

ALMA MATER STUDIORUM · UNIVERSITY OF
BOLOGNA

School of Science

Department of Physics and Astronomy

Master Degree in Physics

**Highly Efficient Monolithic Perovskite/Silicon
Bifacial Tandem Solar Cells**

Supervisor:

Prof. Beatrice Fraboni

Co-Supervisor :

Prof. Stefaan De Wolf

Submitted by:

**Alessandro James
Mirabelli**

Academic Year 2018/2019

Acknowledgements

The only reason why I am here writing these words is because I have had a number of beautiful and wonderful people that have always been around me in my life. Either helping me out, guiding me, or just hanging around and making the time spent more pleasurable, I would probably need to write ten more theses if not more, to pay back all that I have received from them.

I must start by thanking three people in special, because they are the reason why I was able to create and produce all the work that I will go on and bore you with in the following pages. These words of gratitude come easily out of my mind, nothing is forced. This to show just how much they are important. Prof. Beatrice Fraboni, which without her I wouldn't be doing a Master's Degree in the first place and I wouldn't even have had the chance of going to KAUST either. The kindness that she has showered me with during all these years will never be forgotten. Prof. Stefaan De Wolf for giving the chance to this nobody student to visit a fascinating country and also see how high end research is done. Just a small yes from his side meant everything to me and it is hard to convey just how much I appreciated this and am thankful for. Dr. Michele De Bastiani for being the mastermind of all this work. I have no problems in saying that I was mainly the brawn, while he was the brain behind the bifacial project. In these six months the amount of knowledge you have tried to imprint on me is massive. But I must thank you also for the time spent (even if it wasn't much) outside of work, being just a friend and making life at KAUST more enjoyable, and maybe this is what I am most thankful for. To these three people goes everything that I have and can give, and I am pretty sure that I will forever remember this incredible experience.

My gratitude goes then to the other people that have helped me complete my work. I thank Dr. Joel Troughton for taking care of the stability measurements.

Dr. Jiang Liu for helping with the measurement software and the outdoor testing hardware. Dr. Thomas Allen for the bifacial modelling and trying to patiently explain me how it was done. Dr. Michael Salvador for working and measuring at the outdoor testing field in KAUST. Dr. Fabrizio Gota and Prof. Ulrich Paetzold for kindly allowing me to include their energy yield calculations and their outdoor data from Karlsruhe in my work. Without all these people, this thesis simply wouldn't be what it is now, so to all of you: thank you.

I cannot go by without mentioning all the people in KAUST in general, and not just the guys in our group, but also people from other groups and outside of work as well. Thinking back to time spent there just awakens good feelings and makes me smile and laugh. Be it when we went on trips out of the campus, eating together, trying to teach me how to play table tennis, even having the patience of answering my all stupid questions, or just hanging around for a movie or having snacks at the coffee area. Thanks for keeping me company when my hands were not inside the glovebox. You guys have probably already guessed how much this all meant for me when you saw me nearly crack down and cry the last night (by the way, I did end up crying anyways). Thank you.

My thoughts, and also smiles, as I'm writing these words, goes to all my friends in Italy (be it Bologna, Dorno, Pavia or wherever they are) that patiently waited for me to come back from my trip to the desert. Their support, laughter and adventures date way beyond the last six months and stretches to all the different chapters of my life. Just for them I would need to write, not theses anymore, but entire books instead. Encyclopedias probably. They know what they have done for me and probably just have a small, vague idea or seen a glimpse of what they all mean to me. But they will never ever be able to truly understand what their role has been/is in my life and what I owe them. I would need to look at all the synonyms of the english (or italian) language to try and convey in words my feelings for them and still it wouldn't be enough. Guess I would have to move to abstract paintings now to deliver what I feel inside when I think about them.

Thank you.

I must spend some words for my family as well, for having to deal with this troublesome and grumpy child. It is unfortunate how only in the last years I was finally able to grasp the idea of what a family truly means and what it is supposed

to be. I am just sorry that I wasn't able to figure this out earlier. What a complete idiot I have been. Thank you for everything.

My last words are directed to that person who is currently sitting in the living room. She has been alongside me for nearly a decade now, throughout mostly happy moments but also through some terrible ones. And it is especially because she stood by me in those bad periods of my life that she deserves the biggest thank you of them all. Probably without the courage you give me, I wouldn't have gone for such a trip in a far away country, and most certainly without the love that you keep providing me I would not be here writing these words.

Grazie.

Abstract

Perovskite solar cells have been the focus of photovoltaics research in this past decade. Owing to their many favorable properties - like low cost solution processability, tunable bandgap and high efficiency, they have seen much attention in various types of solar cell designs. A promising technology has coupled perovskite cells with another semiconductor material in monolithic tandem solar cells, reaching record efficiencies of 29.15%. However, these kinds of devices require current matching condition to maximize the output of solar cells, making their fabrication challenging. Here, we propose the innovative bifacial tandem configuration to overcome current matching limits between the two sub-cells, by collecting photons from the surrounding environment, i.e. albedo. The extra light shining on our silicon bottom cell boosts the photogenerated current above monolithic tandem values. We show that the current density gain is more pronounced in perovskite solar cells with a narrow bandgap, $1.59eV$, than those with a wider one $1.7eV$. In other words, current matched tandems show little to no increase in efficiency with the extra albedo, while mismatched cells exhibit the most power, reaching up to $\approx 28\%$ in the best scenario. To give more credit to our work, we report outdoor data gathered in various locations around the world, and we show how different albedos have distinct effects on bifacial tandems.

Abstract

Le celle solari con perovskite ibride sono state al centro della ricerca nel settore fotovoltaico nell'ultimo decennio. Grazie a molte delle loro proprietà favorevoli – tra cui i costi ridotti di processo, bandgap variabile e alta efficienza, hanno avuto molta attenzione in diverse configurazioni. Una tecnologia promettente ha incorporato le perovskiti con un altro materiale semiconduttore nelle celle solari tandem monolitiche, raggiungendo efficienze record di 29.15%. Tuttavia, questa tipologia di dispositivi, per massimizzare la potenza prodotta dalle celle solari richiede l'uguaglianza tra le correnti prodotte dalle celle secondarie, facendo sì che la loro fabbricazione diventi ardua. Qui, proponiamo la configurazione tandem bifacciale come modo per aggirare la condizione di uguaglianza di correnti, raccogliendo luce anche dall'ambiente circostante, ovvero l'albedo. La luce extra che incide sul silicio aumenta la corrente fotogenerata, trasformando la parte solitamente limitante della cella, nella parte più performante. Qui, mostriamo come l'aumento di corrente sia maggiore nelle celle tandem con perovskiti con bandgap più piccolo, 1.59eV , piuttosto che in quelle con bandgap grande, 1.7eV . In altre parole, le tandem già bilanciate in corrente traggono poco o nessun profitto dalla albedo extra, mentre dispositivi non equilibrati mostrano l'aumento più grande in efficienza raggiungendo valori attorno al $\approx 28\%$ nei migliori dei casi. Per dar maggior credito al nostro lavoro, riportiamo i dati ottenuti da installazioni all'aperto in varie luoghi attorno al mondo e mostriamo come albedo diversi hanno effetti differenti sulle nostre celle solari tandem bifacciali.

Contents

1	Introduction	1
1.1	Semiconductor Physics	2
1.2	Solar Cell Fundamentals	8
1.3	Characterizing the Solar Cell	11
1.4	Loss Mechanisms	17
1.5	Shockley Queisser Limit	20
1.6	The Silicon Solar Cell Technology	25
1.7	Perovskite	28
1.8	Tandem Solar Cells	35
1.9	Bifacial Solar Cells	40
2	Device Fabrication	43
2.1	The Bottom Cell	43
2.2	The Top Cell	46
2.3	Measurement Setup	51
2.4	Device Encapsulation	53
2.5	Outdoor Testing	54
2.6	Bifacial Stability Characterization	55
3	Results and Discussion	57
3.1	Monofacial 2T Tandem	57
3.2	Bifacial 2T Tandem	63
4	Conclusions	85
4.1	Outlook	87

References

89

Chapter 1

Introduction

Recent years have seen detailed reports stating that global warming is real and poses a major threat to Earth's ecosystem and sustainability. The Intergovernmental Panel of Climate Change (IPCC) declares in their special report on global warming¹ that Earth's average temperature is increasing and it is mandatory to keep the phenomenon in check to avoid huge risks for the entire population. Always the IPCC, in another report², proclaims alarming increased concentration levels of greenhouse gases (GHG) in the last centuries, primarily linked to fossil fuel consumption and CO₂ emission belonging to the beginnings of the industrial revolution. This last year has seen a widespread global rise in awareness regarding Earth's condition. Governments are now demanded to undertake pragmatic actions towards environmental safeguard. A clear message emerged from the many protests seen in 2019, which finds at its core the request to move away from fossil fuel consumption as primary energy source and shift towards renewable ones. We have nowadays a large variety of clean and abundant power sources to choose from, solar, wind, geothermal, hydroelectric, etc. The one we are focusing on in this work, concerns solar energy and photovoltaics.

In the year 2011, global photovoltaic power generation with an installed capacity of $69.68GW$, generated a minuscule amount of $29.66GW$, which accounted for just 0.18% of the total global primary usage³. By the year 2019, the total photovoltaic installed capacity saw a tremendous increase with $593.9GW$ ⁴ installed worldwide; more than 800% growth in just 8 years. As the global market for

photovoltaic depicts, the evolution of global installed capacity is expected to show a sharp rise over the coming years³. However, to achieve a significant share of the total global primary market usage in the next few decades, solar technology requires a rapid expansion in research directions driven by the novel ideas to overcome the present limits. Therefore, in this work, we present the implementation of an already existing idea that has not provided solid evidence so far. Making the following work a primacy in its field. So come with me through this thesis and you'll be, not in a world of pure imagination, but in a new and exciting journey that will show you how to make the best of the reflected sunlight that would otherwise be wasted in a conventional solar cell.

1.1 Semiconductor Physics

Before delving into the physics behind the working principles of a solar cell, we must introduce a few key concepts. Firstly, in order to absorb light, solar cells are composed by semiconductors. Differently from metals, where electrons can be modelled according to an ideal gas system, in semiconductors electrons are confined in a band structure (fig. 1.1). In absence of external stimuli (i.e. temperature or light) electrons populate the states of the “valence band” (VB). In the VB electrons are localized and do not participate in conduction. In presence of external stimuli, electrons can absorb energy and promote in the “conduction band” (CB). Electrons in the conduction band are free to move within the lattice and participate in conduction. The Fermi level (E_F) determines the energetic of the system and usually lies in between the CB and VB. The difference in energy between the CB and the VB is defined as “bandgap” and represents a forbidden region of energies for electrons. Ideally, the VB is fully populated with electrons and the CB is fully underpopulated. When one electron is promoted from the VB to the CB, the lack of negative charge (therefore positive charge) left in its former position in the VB is defined as “hole” (h+).



Figure 1.1: Sketch of the energy levels of a metal (left) and semiconductor (right). In a semiconductor, the VB and CB are separated by a forbidden zone called bandgap.

Secondly, we introduce the concept “doping”, i.e. the mechanism by which it is possible to manipulate the concentration of electrons and holes inside the semiconductor. Technically, this is achieved by inserting atoms of a foreign species into the semiconductor. This alters the crystal lattice structure and electronic bonds in the material (fig. 1.2). In the case of crystalline silicon, common dopants are boron (B) and phosphorous (P). These two elements have differing atomic numbers compared to silicon, meaning that when either P or B are introduced in the crystal’s skeleton, we change the electronic landscape in the vicinity of the dopant. In the case of B, atomic number 5, we have a missing electron or an extra positive one – respect to Si. Such materials are called “acceptors”. On the other hand, phosphorous with atomic number 15, has an excess electron that can be donated to the crystal, and for such reason the resulting material will be called “donor”. We denote a semiconductor as p-type or n-type when holes or electrons, respectively, dominate its electrical conductivity.

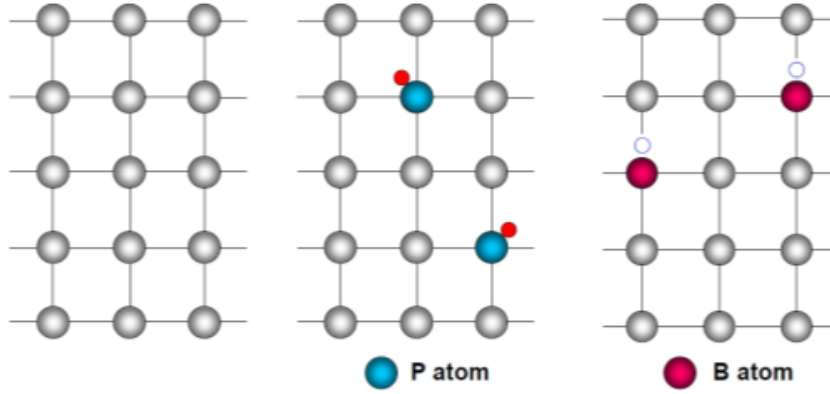


Figure 1.2: Crystal lattices of different semiconductors: undoped (left), n-type (centre), p-type (right).

Inserting donor and acceptor atoms into the lattice of crystalline silicon modifies the energy levels by allowing states to exist in the forbidden bandgap. Where with this last term we identify that section of the band diagram, which is prohibited for a semiconductor, i.e. in between the VB and the CB. In detail, a donor atom will create an energy state E_d just under the CB. While an acceptor atom permits states E_a close to the VB. The action of doping also modifies the Fermi level E_F (fig. 1.3). If we increase the electron concentration, the Fermi energy will move closer to the CB, instead it will shift down towards the VB in the case we insert more holes in the semiconductor. We can measure the position of the Fermi level in an n-type and p-type material from the following equations respectively,

$$E_C - E_F = k_B T \ln \left(\frac{N_C}{N_D} \right) \quad (1.1)$$

$$E_F - E_V = k_B T \ln \left(\frac{N_V}{N_A} \right) \quad (1.2)$$

Where E_C is the minimum attainable conduction band energy, E_V the maximum valence band energy, N_D the donor concentration and N_A the acceptor one, N_C and N_V are the effective densities of the conduction band states and the valence band states, respectively. They are defined as

$$N_C = 2 \left(\frac{2\pi m_n^* k_B T}{h^2} \right)^{\frac{3}{2}} \quad \text{and} \quad N_V = 2 \left(\frac{2\pi m_p^* k_B T}{h^2} \right)^{\frac{3}{2}} \quad (1.3)$$

With m_p^* and m_n^* are the effective masses of hole and electrons.

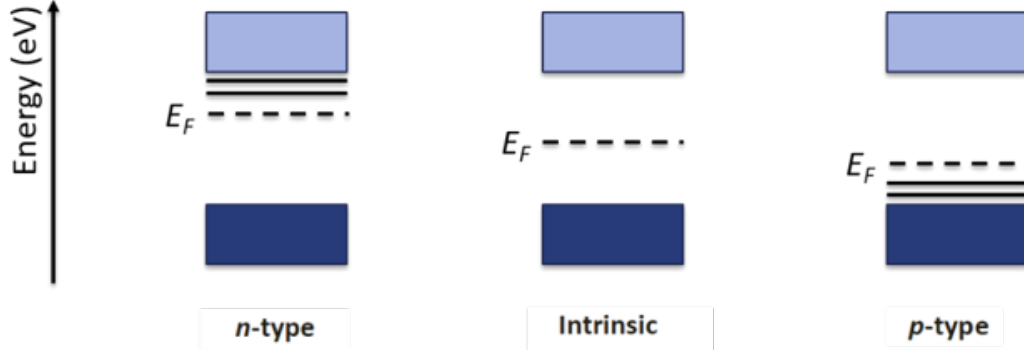


Figure 1.3: Energy levels of doped and undoped semiconductors. Depending on the type of dopant, the Fermi level E_F shifts according to equations 1.1 and 1.2.

The next step towards understanding a solar cell is the definition of the p - n junction (fig. 1.4). When a p -type and an n -type semiconductor are brought together, a very large difference in electron concentration between n - and p -type regions causes a diffusion current of electrons from the n -type material across the interface into the p -type material. Similarly, the difference in hole concentration causes a diffusion current of holes from the p - to the n -type material. Due to this diffusion mechanism the region closest to the interface becomes almost depleted of mobile charge carriers, hence the name “depletion region” or “space charge region”. Inside this area around the interface an internal electric field is formed due to the uncompensated donor and acceptor atoms. This field forces the charge carriers to move in the opposite direction of the concentration gradient. The diffusion currents continue to act until all the forces in play are compensated with one another, i.e. the concentration gradient and the internal electric field. Therefore, the driving force for the charge transport does not exist anymore and no net current flows through the p - n junction. In equilibrium we can define,

$$V_{bi} = \frac{k_b T}{q} \ln \left(\frac{N_A N_D}{n_i^2} \right) \quad (1.4)$$

Which is the electrostatic potential difference across the p - n junction, and it is called built in voltage.

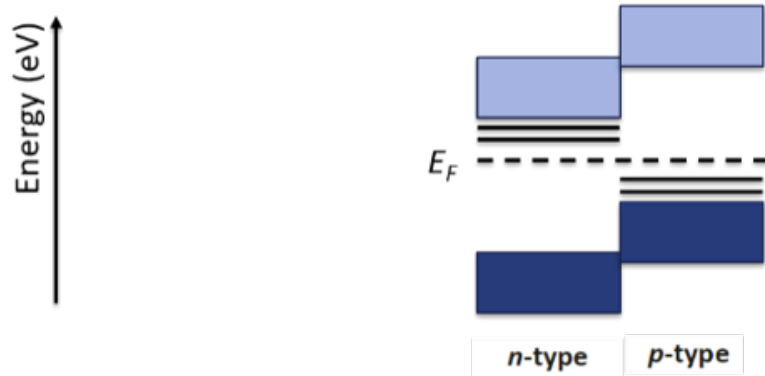


Figure 1.4: Energy sketch of a p - n junction. When different doped semiconductors are juxtaposed, the respective E_{FS} align.

If we now apply an external voltage, V_a , to the system, we modify the potential difference between the two regions ($V_{bi} - V_a$) (fig. 1.5). Depending on the sign of V_a we may be in reverse or forward bias. In the first case, we apply negative V_a in respect to the potential of the p -type region and we end up increasing the potential barrier, thus widening the depletion region. Instead, if we apply now positive V_a in respect to the potential of the p -type, we decrease the barrier and we narrow down the space charge region. In both cases, the system is not in equilibrium anymore and now the concentrations of electrons and holes are described by their quasi Fermi levels E_{Fn} and E_{Fp} respectively.

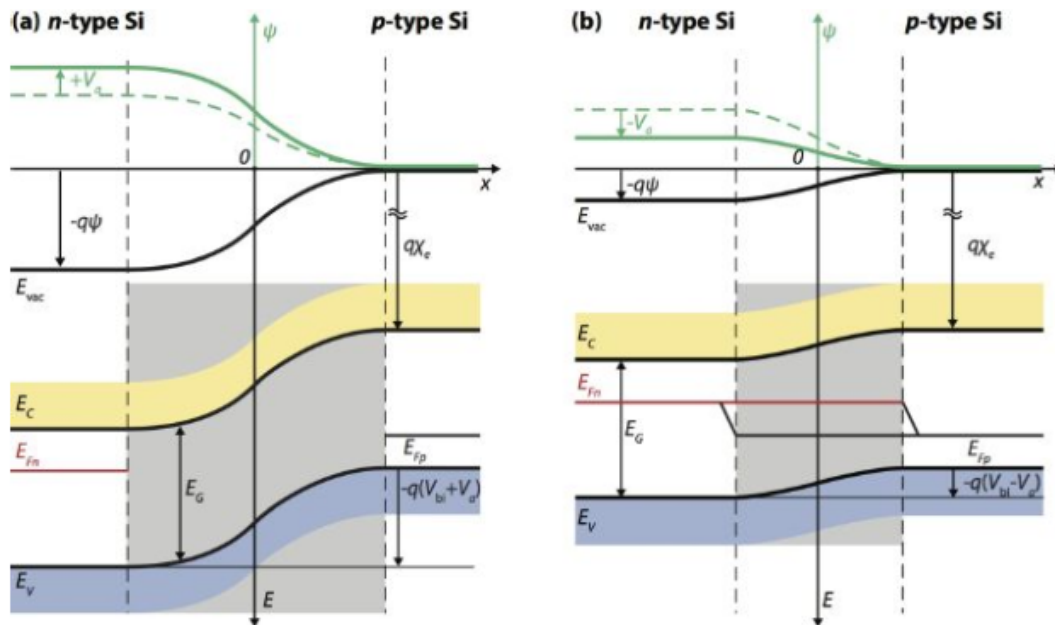


Figure 1.5: Energy band diagram and electrostatic-potential (in green) of a p - n junction under (a) reverse bias and (b) forward bias conditions⁵.

When the p - n junction is illuminated, extra charge carriers are generated in the semiconductor. The concentration of minority carriers strongly increases, leading to a flow of minority carriers across the depletion region into the quasi neutral regions. Electrons flow from the p -type into the n -type and holes from the n -type into the p -type regions. This flow of photo-generated carriers J_{ph} adds to the thermal generation current J_{gen} , which in turn, as the name suggests, is determined by the available thermally generated minority carriers in the doped regions.

1.2 Solar Cell Fundamentals

The working principle of solar cells is based on the photovoltaic effect, i.e. the generation of a potential difference at the junction of two different materials in response to electromagnetic radiation. This effect can be divided into three basic processes (fig. 1.6): 1) generation of charge carriers due to the absorption of photons in the material that forms a junction, 2) separation of the photo-generated charge carriers in the junction, 3) collection of the photo-generated charge carriers at the terminals of the junction.

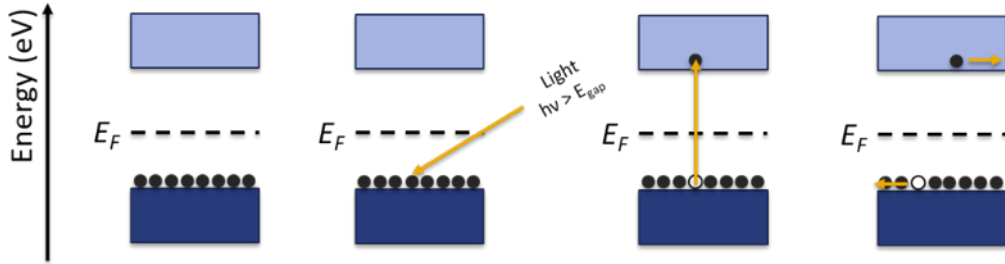


Figure 1.6: Diagram illustrating the photovoltaic effect. A semiconductor absorbs an incoming photon with $h\nu > E_g$. An electron from the VB is promoted to the CB leaving a hole behind. The two charge carriers are collected at the terminals of the junction.

The absorption of a photon in a material means that its energy is used to excite an electron from an initial energy level E_1 to a higher energy level E_2 . Photons can only be absorbed if the energy difference between the two levels E_1 and E_2 is smaller than the energy ($h\nu$) carried by the photon, i.e. $h\nu > E_2 - E_1$. In an ideal semiconductor, electrons can populate energy levels below the valence band edge (E_V) and above the conduction band edge (E_C). As defined previously, the difference between E_C and E_V is known as the energy bandgap (E_g). E_g refers to a particular area of the k-space where no electrons can be present. This means that if a photon with less energy than E_g reaches an ideal semiconductor, it will not be absorbed and instead will traverse the material without interaction.

However, in a real semiconductor, the valence and conduction bands are not flat, but vary depending on the k-vector, a quantity that describes the momentum of an electron in the semiconductor. If the maximum of the valence band and the

minimum of the conduction band occur at the same k-vector, and electron can be excited from the first to the second state, without any change in the momentum. Such a semiconductor is called a direct bandgap material. Instead, if the electron cannot be excited without changing its momentum, the semiconductor is defined as indirect bandgap (fig. 1.7). This momentum variation is done via the help of a phonon, which we can define as the quantum unit of a crystal lattice vibration. As stated previously, when this excitation takes place from E_1 to E_2 , a hole is created. Therefore, for any photovoltaic device, the interaction of photons with the electron-hole arrangement of an absorbing semiconductor results in the transfer/conversion of radiative energy from the first, to chemical energy of the latter. This exchange mechanism allows for the production of useful work on an external system, and the maximum conversion efficiency from radiative to chemical energy is limited by thermodynamics and is set at 67%⁶.

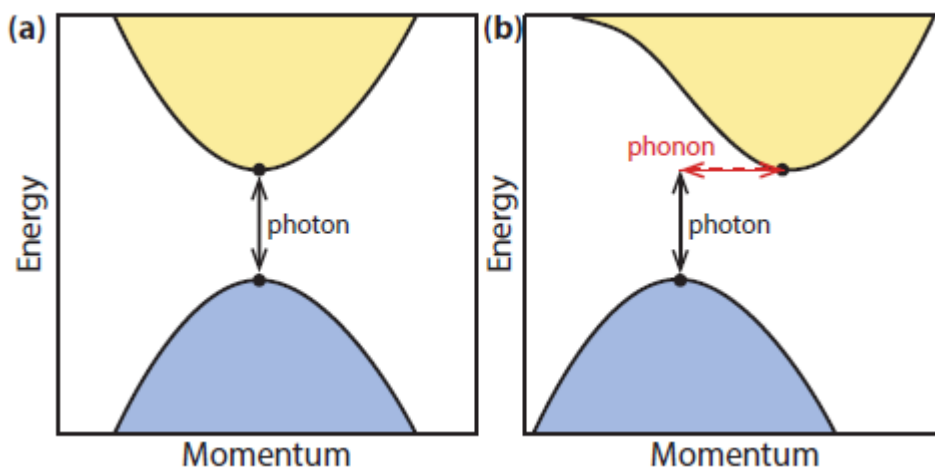


Figure 1.7: Illustrating the difference between a direct semiconductor (a) and an indirect semiconductor (b)⁵.

On the other hand, the electron-hole pair will also indulge in the reverse process, i.e. the electron will fall back to the initial state E_1 , releasing energy. This recombination mechanism can happen with the creation and emission of a new photon (radiative), or with energy transfer to the crystal lattice (non-radiative). Therefore, in order to efficiently use the energy from the incoming radiation and thus performing work, a solar cell has to be designed such that electrons and holes

are split up and directed towards different locations where they have less probability to recombine. In a regular p - n junction, charge separation occurs thanks to the built-in electric field. In such a system, the lifetime of the minority carriers is key to the final performance of a solar cell as it determines the recombination with the majority carriers. A long lifetime assures that electrons/holes can travel to their respective electrodes.

Finally, the charge carriers are extracted from the solar cell with electrical contacts so that they can perform work in an external circuit. Here, the chemical energy of the electron hole pair is converted to electric energy. After the electrons have passed through the circuit, they will recombine with holes at a metal-absorber interface.

1.3 Characterizing the Solar Cell

The main parameters that are used to characterize the performance of a solar cell are the maximum power point P_{max} , the short circuit current density J_{sc} , the open circuit voltage V_{oc} , and the fill factor FF . These parameters are determined from the illuminated J-V curve (fig. 1.8) and the conversion efficiency η can be calculated from them.

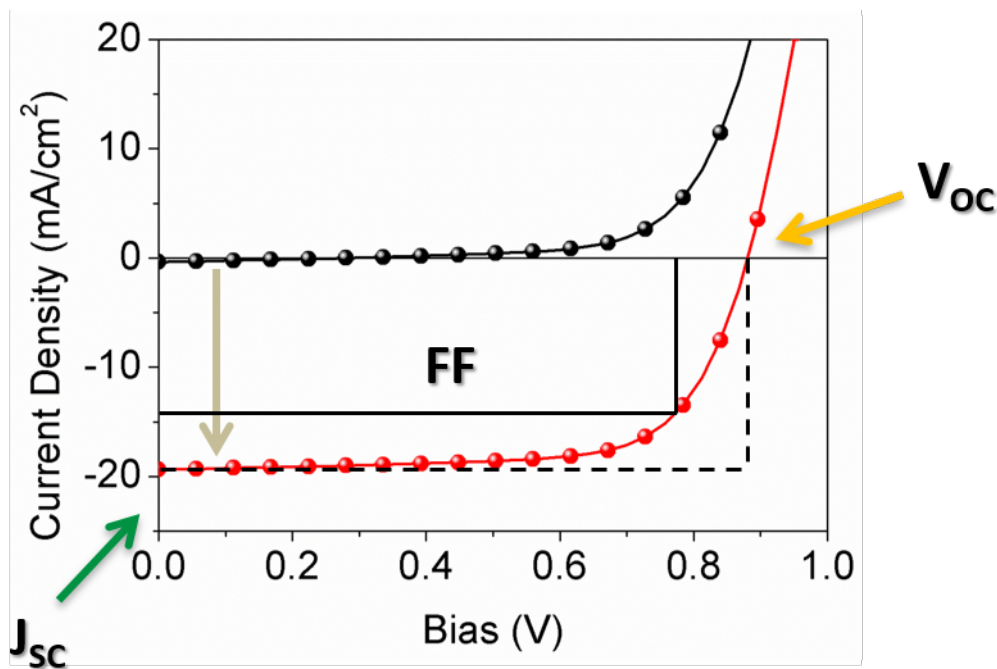


Figure 1.8: Example of a typical current density-voltage curve of a solar cell in dark (black) and under illumination (red).

The short circuit current I_{sc} is the current that flows through the external circuit when the electrodes of the solar cell are short circuited. In order to remove the dependence of the solar cell area, the short circuit current density is used to describe the maximum current that can be delivered by the device. In the ideal case, J_{sc} is equal to J_{ph} , which is the maximum photo generated current achievable by the absorber, and it is written as

$$J_{ph} = qG(L_N + W + L_P) \quad (1.5)$$

Where G is the electron/hole pair generation rate, L_N and L_P are the minority carrier's diffusion length for electrons and holes respectively, and W is the width of the depletion region. From equation 1.5 it is clear that only carriers generated in the depletion region and regions up to the minority carrier diffusion length from the depletion region, can contribute to the photo generated current. For example, crystalline silicon solar cells can theoretically deliver $46mA/cm^2$ under AM1.5 spectrum, whereas commercial solar cells have a J_{sc} that goes just above $40mA/cm^2$.

The open circuit voltage V_{oc} , is the voltage at which no current flows though the external circuit. It indicates the maximum voltage a solar cell can deliver and can be calculated from equation

$$J(V_a) = J_{rec}(V_a) - J_{gen}(V_a) - J_{ph} = J_0 \left[\exp\left(\frac{qV_a}{k_B T}\right) - 1 \right] - J_{ph} \quad (1.6)$$

Assuming that the net current is zero,

$$V_{oc} = \frac{k_B T}{q} \ln\left(\frac{J_{ph}}{J_0} + 1\right) \approx \frac{k_B T}{q} \ln\left(\frac{J_{ph}}{J_0}\right) \quad (1.7)$$

Where the approximation is justified because $J_{ph} \gg J_0$. From equation 1.7 we notice that the V_{oc} depends on the saturation current density J_0 , which in turn depends on the recombination effects inside the solar cell. Therefore, V_{oc} is a measure of the amount of recombination events that occur in the device.

The fill factor is the ratio between the maximum power ($P_{max} = J_{mpp}V_{mpp}$) generated by the solar cell and the product V_{oc} with J_{sc}

$$FF = \frac{J_{mpp}V_{mpp}}{J_{sc}V_{oc}} \quad (1.8)$$

Where the subscript ‘‘mpp’’ denotes the maximum powerpoint (MPP) of the solar cell, i.e. the point on the J-V curve at which the device delivers the maximal power. For commercial applications, it is very important to operate the solar cells (or PV modules) at the MPP.

The conversion efficiency is calculated as the ratio between the maximal generated power and incident power. Solar cells are measured under standard test

conditions (STC), where the incident light is described by the AM1.5 spectrum and has an irradiance of $I_{in} = 1000W/m^2$,

$$\eta = \frac{P_{max}}{I_{in}} = \frac{J_{mpp}V_{mpp}}{I_{in}} = \frac{J_{sc}V_{oc}FF}{I_{in}} \quad (1.9)$$

Since we have stated that the absorption of a photon depends on its energy, it is important to know the spectral distribution of the solar radiation, meaning the number of photons of a certain energy as a function of the wavelength λ . Two quantities are used to describe the solar radiation spectrum, namely the spectral irradiance $I_{e\lambda}$, and the spectral photon flux $\Phi_{ph}(\lambda)$ defined as:

$$I_{e\lambda} = \int_{2\pi} L_e \cos \theta d\Omega = \int_{2\pi} L_e(\zeta, \eta; \theta, \phi) \cos \theta \sin \theta d\theta d\phi \quad (1.10)$$

$$\Phi_{ph} = \frac{\partial^2 \Psi_{ph}}{\partial A} \quad (1.11)$$

With a surface temperature of $\approx 6000K$, the Sun is considered a perfect black body and emits a spectrum described by figure 1.9. Since sunlight traverses the atmosphere to reach terrestrial solar panels, we distinguish between the spectrum outside and inside the atmosphere. Outside the atmosphere we define AM0 the spectrum that gives an irradiance equal to $I_e(AM0) = 1361Wm^{-2}$. When solar radiation crosses the atmosphere, it is attenuated by the absorption of atmospheric agents such as water, carbon dioxide, and ozone. The key parameter to keep in mind is the distance that the sunlight must travel to reach the earth's surface, which is shortest when the Sun is at the zenith. The ratio of the actual path length of the sunlight to this minimum distance is known as the optical air mass. At the zenith this quantity is unity and resulting spectrum is called air mass 1 (AM1). In general, when the Sun is at an angle θ with the zenith, the air mass is given by:

$$AM \equiv \frac{1}{\cos \theta} \quad (1.12)$$

The AM1.5 spectrum is a reference solar spectral distribution, being defined in the International Standard IEC 60904-3⁷. This spectrum is based on the solar irradiance received on a Sun-facing plane surface tilted at $^\circ 37$ to the horizontal.

Both direct, diffuse, and the albedo are considered. With albedo we define the part of the solar radiation that is reflected by the earth's surface, depending on the reflectivity of the environment.

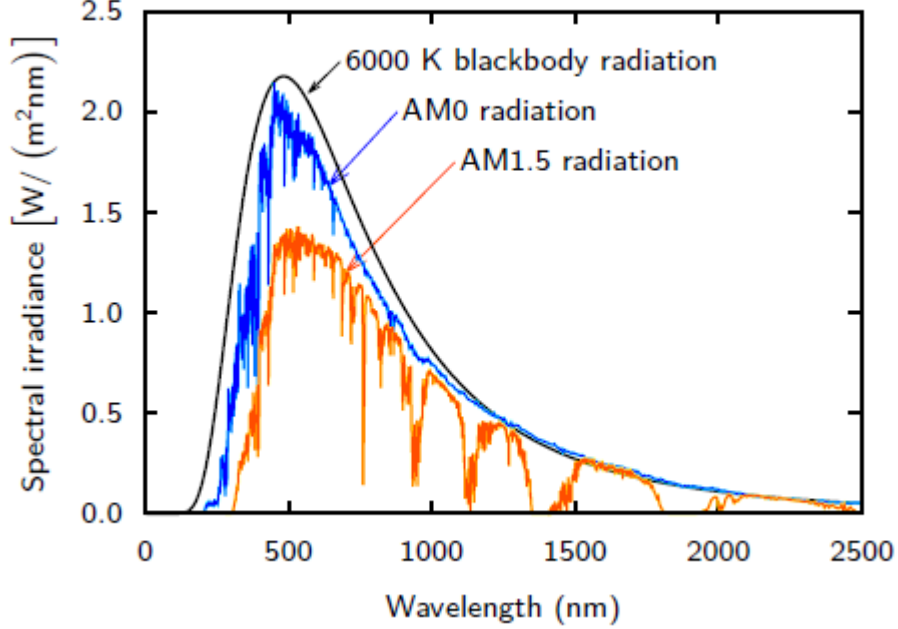


Figure 1.9: Different solar spectra: the blackbody spectra at $6000K$, the extraterrestrial AM 0 and the AM 1.5 spectrum⁵.

Another important quantity that describes a solar cell is the external quantum efficiency ($EQE(\lambda)$). It is the fraction of photons incident on the solar cell that create electron-hole pairs in the absorber, which are then successfully collected. Wavelength dependent, it is usually measured by illuminating the solar cell with monochromatic light at different (λ) and measuring the corresponding photocurrent I_{ph} through the solar cell. The EQE is then determined as:

$$EQE(\lambda) = \frac{I_{ph}(\lambda)}{q\Psi_{ph,\lambda}} \quad (1.13)$$

Where q is the elementary charge and $\Psi_{ph,\lambda}$ is the spectral photon flow incident on the solar cell. I_{ph} depends on the bias voltage, which is fixed during measurement, and the photon flow is usually determined by taking the EQE of a calibrated

photodiode under the same light source,

$$\Psi_{ph,\lambda} = \frac{I_{ph}^{ref}(\lambda)}{qEQE^{ref}(\lambda)} \quad (1.14)$$

By combining the two (eq. 1.13 and eq. 1.14) we obtain,

$$EQE(\lambda) = EQE^{ref}(\lambda) \frac{I_{ph}(\lambda)}{I_{ph}^{ref}(\lambda)} \quad (1.15)$$

The shape of the EQE curve is deeply connected to the optical and electrical properties of the material, meaning it considers all possible losses associated to the device. Analysing this data can provide information regarding parasitic absorption and recombination losses. For example, in solar cells that have short minority carrier diffusion lengths or surface recombination, the EQE curve will be affected and will drop to lower values, reflecting such losses. Instead, when EQE values reach close to 1, it means that almost all absorbed photons are converted into electron-hole pairs that can leave the solar cell. The EQE of a high quality crystalline silicon based solar cell is reported in figure 1.10.

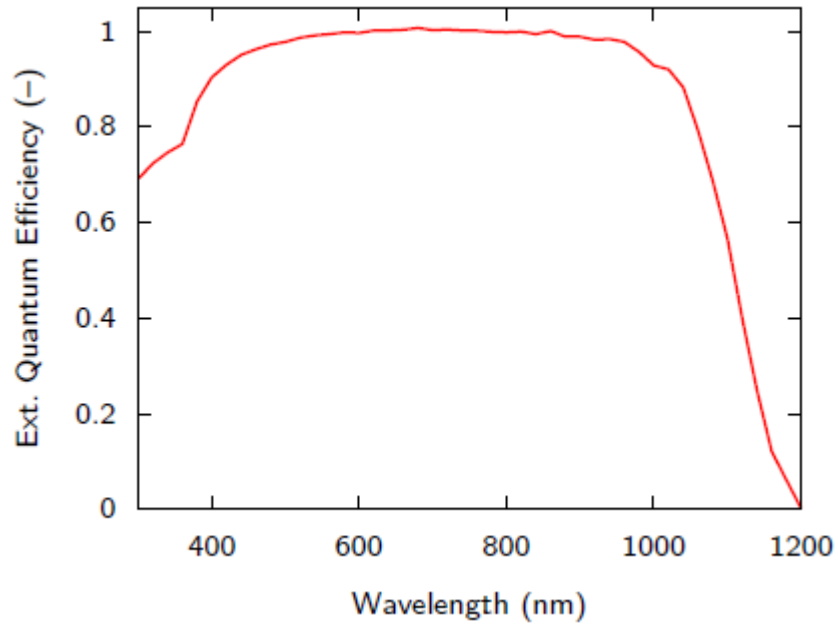


Figure 1.10: EQE of a high quality crystalline silicon-based solar cell⁵.

At 0V bias, the measured J_{ph} is equal to J_{sc} . Determining J_{sc} via the EQE has the advantage of being independent of the area and spectral shape of the light source used, thus giving a more accurate value than a J-V measurement. To determine the J_{sc} we combine the photon flow at a certain wavelength with the associated EQE, leading to the flow of electrons leaving the solar cell for that λ . J_{sc} is then obtained by integrating across all relevant wavelengths,

$$J_{sc} = -q \int_{\lambda_1}^{\lambda_2} EQE(\lambda) \Phi_{ph,\lambda}^{AM1.5} d\lambda \quad (1.16)$$

1.4 Loss Mechanisms

Having discussed the fundamentals behind a functioning solar cell, we are now obliged to briefly describe the processes that hinder the efficiency of a device. As we have already mentioned, only the extracted charge carriers contribute to the J_{sc} . If we don't collect them, it means the electron hole pair has recombined. It is clear then, that the recombination rate strongly influences the final performance of solar cells. We distinguish between radiative and non-radiative recombination depending on whether a photon is re-emitted or not in the process. Deeply connected to this topic is the concept of minority carrier lifetime. Already introduced before, here it can be seen as the time constant at which an excess carrier concentration decays exponentially, if external generation is no longer taking place, i.e. no light is shining on the solar cell. N-type, τ_{nd} , and p-type, τ_{pd} lifetimes are defined as,

$$\tau_{pd} = \frac{1}{\beta n_0} \quad (1.17)$$

$$\tau_{nd} = \frac{1}{\beta p_0} \quad (1.18)$$

Where β is a temperature dependent constant and p_0 and n_0 are the equilibrium concentrations of holes and electrons, respectively.

Another important detrimental effect to solar cells is the Shockley-Hall recombination process. Here, the recombination of electrons and holes does not occur from bandgap to bandgap. It is facilitated by an impurity atom or lattice defects, also defined as "trap". These trap states introduce allowed energy levels E_t within the forbidden gap. An electron can then be trapped in such a defect and consequently recombine. It is usually non radiative, and the excess energy is dissipated into the lattice in the form of heat. Even in this case we can define the lifetimes of holes, $\tau_{p,SRH}$, and electrons, $\tau_{n,SRH}$, as

$$\tau_{p,SRH} = \frac{1}{c_p N_T} \quad \text{and} \quad \tau_{n,SRH} = \frac{1}{c_n N_T} \quad (1.19)$$

Where c_p and c_n are the respective hole and electron capture coefficient, and

N_T the trap density.

Lastly, we mention the Auger recombination which is dominant in indirect bandgap semiconductors. Here we involve three particles instead of two. When an electron recombines with a hole, they pass this energy and momentum either to another electron or another hole. If the third particle is an electron, it is excited higher up into the conduction band to then thermalize at a second stage exchanging vibrational energy with the lattice. A hole instead, moves towards deeper levels in the valence band and again then gives its energy to the lattice, allowing it to rise again towards the valence band edge. Auger recombination strongly depends on the charge carrier densities of electrons and holes, as seen from the square dependence in the definition of their lifetimes,

$$\tau_{eeh} = \frac{1}{C_n N_D^2} \quad (1.20)$$

$$\tau_{ehh} = \frac{1}{C_p N_A^2} \quad (1.21)$$

Where C_n and C_p are proportionality constants that are dependent on the temperature⁸. A summary of the major losses that can hinder solar cell performance are depicted in figure 1.11.

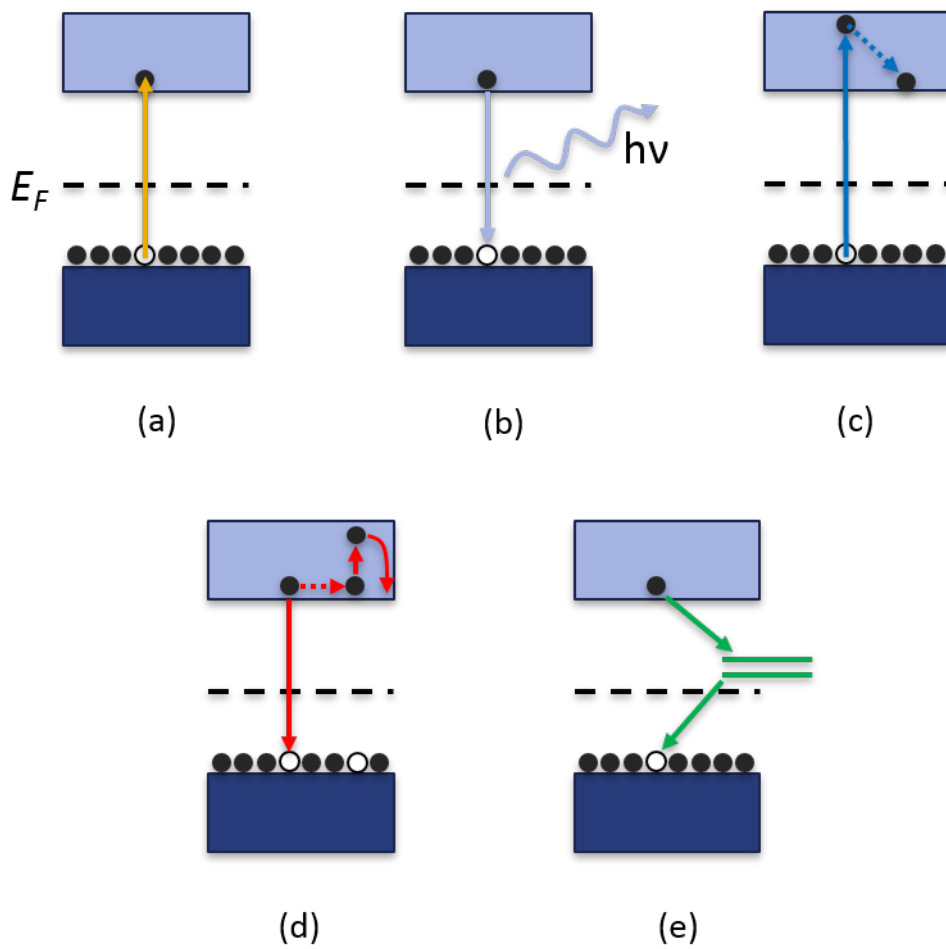


Figure 1.11: Summary of the various loss mechanisms that occur in a solar cell when a photon is (a) absorbed: (b) radiative recombination, (c) thermalization loss, (d) Auger recombination, (e) Shockley-Hall trap assisted recombination.

1.5 Shockley Queisser Limit

In 1961 the Journal of Applied Physics published an article by William Shockley and Hans J. Queisser titled: “*Detailed Balance Limit of Efficiency of p-n Junction Solar Cells*”. Here, the authors proposed a new theoretical upper limit for the efficiency of solar cells employing *p-n* junctions in semiconductors. They stated that this limit “is a consequence of the nature of atomic processes required by the basic laws of physics, particularly the principle of detailed balance”⁹. Such a limit, called the detailed balance limit, is calculated and compared with the previous existing limit called the “*semiempirical limit*”^{10,11}. A comparison of the two limits is shown in figure 1.12.

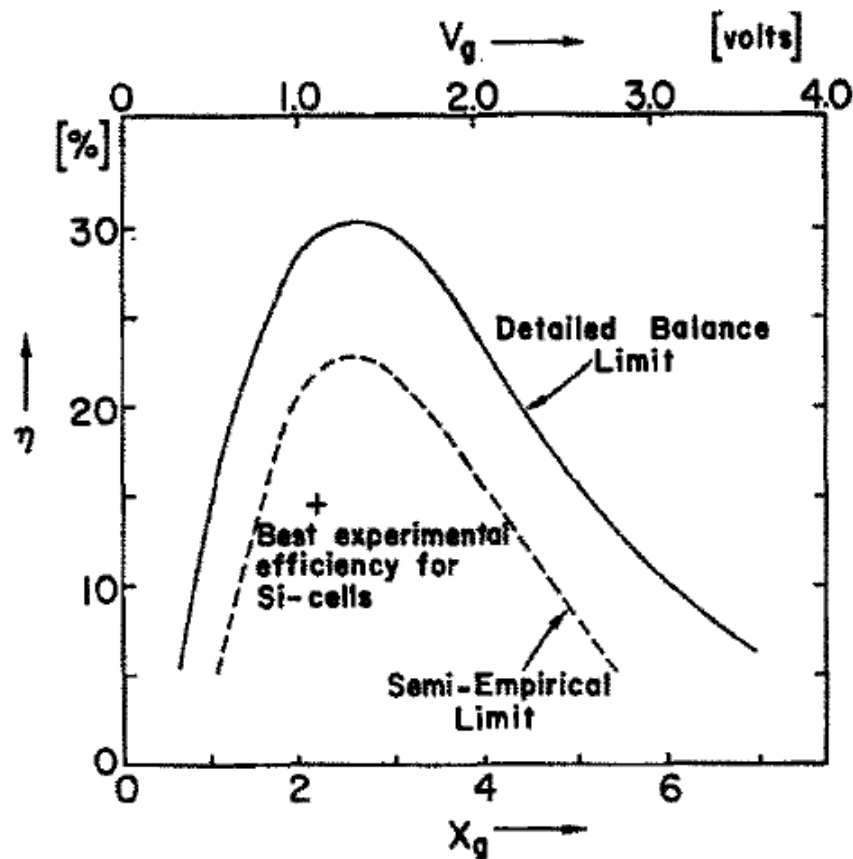


Figure 1.12: Comparison of the “*semiempirical limit*” of efficiency of solar cells with the “*detailed balance limit*”⁹.

Shockley and Queisser (SQ) stated that a solar cell's efficiency is limited by two factors: i) the energy gap of the active absorber; ii) the number of recombination events between electrons and holes that results in the emission of a photon (radiative recombination). In turn, radiative recombination limits the lifetime of minority carriers and determines the efficiency of light conversion. Indeed, if radiative recombination is only a fraction of all recombination effects, then the efficiency is substantially reduced below the detailed balance limit.

Consequently, SQ posed three hypotheses to determine the maximum efficiency. First, each photon with energy greater than $h\nu_g$ produces one electronic charge q at a voltage $V_g = h\nu_g/q$. Second, radiative recombination is the only recombination mechanism present. Third, all the photoexcited electrons are extracted from the conduction band, those that have extra energy (hot carriers) relax at the conduction band edge.

Thus, the efficiency can be defined as the electrical power out of the cells into a matched load divided by the incident solar energy irradiating the solar cell:

$$\eta = \frac{I [V (max)] V (max)}{P_{inc}} \quad (1.22)$$

According to eq. 1.22, a single active absorber solar cell, otherwise known as single junction solar cell, has a theoretical upper limit set at around 30%, which is still remarkably higher than those efficiencies reported for the best solar technologies¹². As an example, the best silicon solar cell reached an efficiency at 26.6% (Kaneka) while the best perovskite reported so far 25.2%¹².

From this, a natural question arises. What is preventing a solar cell from reaching the theoretical SQ limit? To begin with, we would like to note that SQ's limit for a solar cell derives only from its bandgap and temperature. The absorption cross-section, determined by the absorption coefficient, calculates absorption and emission as step function with zero absorption below and full absorption above E_g . This implies that the optical properties of the device and any concepts for light trapping are not considered in the original SQ theory. Instead, a real device must deal with a series of issues that cause either electrical or optical losses and result in an efficiency that is much lower from the modelled one. These losses can be summarized as the following¹³:

- Absorption loss: in a single junction solar cell, the bandgap energy limits the generated current. The maximum accessible short-circuit current density J_{sc}^{max} is given for perfect light absorption above the energy E_g and no absorption below energy E_g . However, in a real device we must consider that absorption is a probability. This means that we refer to an average number of absorbed photons and consequently, to an average energy loss due to non absorption.
- Carnot loss: a solar cell can be imagined as a heat engine that generates work while heat flows from the hot reservoir of the sun ($T_s = 5800K$) to the cold reservoir of the solar cell device with its surrounding atmosphere ($T_c = 300K$). We can estimate the loss by considering first the open circuit voltage (V_{oc}) of a monochromatic solar cell. Such a device interacts with the sun only at a single wavelength E_{mo} . In the radiative limit and under full concentration, there is no thermalization. The resulting V_{oc} is therefore¹⁴

$$qV_{oc}^{mo} = E_{mo} (1 - T_c/T_s) \quad (1.23)$$

And it represents the limiting efficiency of the conversion of a single photon into electrical energy. If we expand this reasoning to an infinite number of monochromatic solar cells with $E_{mo} > E_g$, we obtain:

$$V_{oc}^{Carnot} = \frac{\bar{E}_{sun}(E_g)}{q} \left(1 - \frac{T_c}{T_s} \right) \quad (1.24)$$

This value corresponds to the maximum V_{oc} that can be obtained by a reversible process that makes use of all solar photons with energy larger than E_g .

- Thermalization loss: in a single junction solar cell, the charge carriers which are excited beyond the bandgap thermalize to energy levels close to E_g . This causes an irreversible loss process that decrease the V_{oc} below the Carnot limit. The resulting value is

$$V_{oc}^{max} \approx \frac{E_g}{q} \left(1 - \frac{T_c}{T_s}\right) + \frac{k_b T_c}{q} \ln \left(\frac{T_s}{T_c}\right) \quad (1.25)$$

The second term represents the increase in energy of charger carriers at the band edge due to their thermal energy.

- Etendue expansion loss: this additional thermodynamic loss is associated with the increase in solid angle between the photons emitted from the solar cell and the incident photons from the sun. If the etendue of the emitted photons (ε_{out}) from the solar cell is larger than the small etendue of the incident photons of the sun (ε_{in}), entropy will be produced since the directional order of the photons is decreased. The loss can be expressed by

$$V_{oc}^{etendue} = V_{oc}^{max} + \frac{k_b T_c}{q} \ln \left(\frac{\varepsilon_{in}}{\varepsilon_{out}}\right) \quad (1.26)$$

- Nonradiative loss: nonradiative recombination losses or parasitic optical losses in the solar cell induce thermalization of charger carriers in the device, which produces thermal losses and is written as

$$V_{oc}^{nonrad} = V_{oc}^{etendue} + \frac{k_b T_c}{q} \ln \{Q_e^{LED}\} \quad (1.27)$$

Where Q_e^{LED} is the external LED quantum efficiency of the device define via

$$Q_e^{LED} = \frac{J_0^{rad}}{J_0^{rad} + J_0^{nrad}} \quad (1.28)$$

Here, we distinguish between the saturation current J_0^{rad} that leads to emission of one photon per injected electron from the saturation current J_0^{nrad} that does not lead to photon emission.

The losses pointed out here make it clear why the theoretical limit is still far away. Even though some factors can and have been reduced/minimized, like unwanted reflection, parasitic absorption and non radiative recombination¹⁵, the efficiencies achieved so far are still behind the practical limit. In light of this,

many researchers have looked for alternatives to overcome these limits: hot carrier conversion¹⁶, quantum confinement¹⁷, multiple exciton generation¹⁸, up and down conversion¹⁹. However, there is another technology that has been the hope of researchers for the past few decades¹²: tandem solar cells.

1.6 The Silicon Solar Cell Technology

Since its beginning, silicon solar cells dominated the photovoltaic (PV) technology. Over the last twenty years, the silicon solar cells have been constantly improved, aiming to more efficient devices, up to the point where solar energy is considered the most promising among all the renewable energies. Part of this success can be ascribed to a constant reduction in the costs of monocrystalline silicon (c-Si), today below 0.25\$/watt, which is gradually drifting away the PV market from the multicrystalline (multi-Si) technology (cheaper, but less efficient). In parallel to the cost's reduction, the development of contact passivation further advanced the progress of c-Si solar cells over multi-Si. The vast majority of commercially manufactured c-Si solar cells, commonly called Al-BSF (aluminum back surface field) solar cells, are processed with only five main fabrication steps (texturing; front phosphorus diffusion; silicon nitride, SiN_x , deposition; screen printing and co-firing of the metal electrodes). This simplicity is a result of the fact that many of the processes and materials combine to enact multiple functions in the device. This simplicity in manufacturing has enabled low cost, high throughput production at the expense of device performance. An evolution of the Al-BSF technology is represented by the PERC (passivated emitter and rear cell) configuration. PERC devices are manufactured in a similar way to the Al-BSF cell but with rear-surface passivation (often aluminium oxide, AlO_x) and localized aluminium BSF contacts (typically defined by laser ablation of the AlO_x layer). The addition of the passivation layer at the rear suppresses surface recombination, thereby increasing the device voltage relative to the full-area Al-BSF cell. For this reason, PERC cells have a higher efficiency potential. Figure 1.13 summarizes the fabrication process of Al-BSF and PERC solar cells.

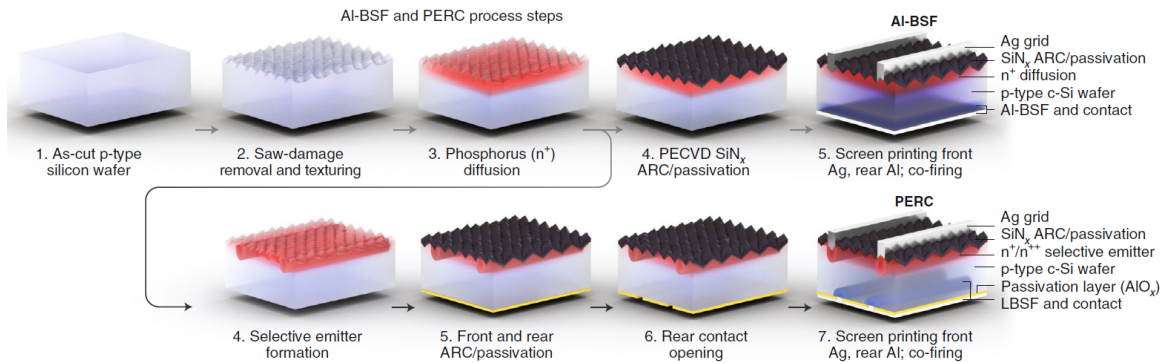


Figure 1.13: Fabrication process of Al-BSF and PERC solar cells²⁰.

A relatively simple passivating contact device design is that of the silicon heterojunction cell (SHJ), which takes the doping outside of the c-Si absorber and places it within the contact structure in the form of n- and p-doped a-Si:H layers. The SHJ device architecture, like the Al-BSF cell, benefits from a conceptually facile fabrication procedure: a thin film of intrinsic a-Si:H is sandwiched between the silicon wafer and the doped a-Si:H layers in order to passivate surface defects, resulting in high operating voltages. A transparent conductive oxide (TCO; typically sputtered indium tin oxide, ITO) provides lateral charge transport to the screen-printed metal fingers and acts as the anti reflective coating (ARC). Figure 1.14 shows the fabrication process of SHJ. The most critical performance limitation of this design is parasitic absorption in the front TCO and a-Si:H layers, spurring research into alternative materials and device designs. One solution to this problem is to place all of the contacts on the rear side of the wafer in an interdigitated back contacted (IBC) architecture. Alongside the increase in fabrication complexity, the transfer of the front contacts to the rear side of the cell places stricter requirements on both the electron and hole contact resistivities owing to their relative reduction in surface area. In addition, since the vast majority of excess carriers are photo-generated at the front of the wafer, high bulk lifetimes and state-of-the-art surface passivation is necessary to achieve the long diffusion lengths needed to maintain a high quantum efficiency.

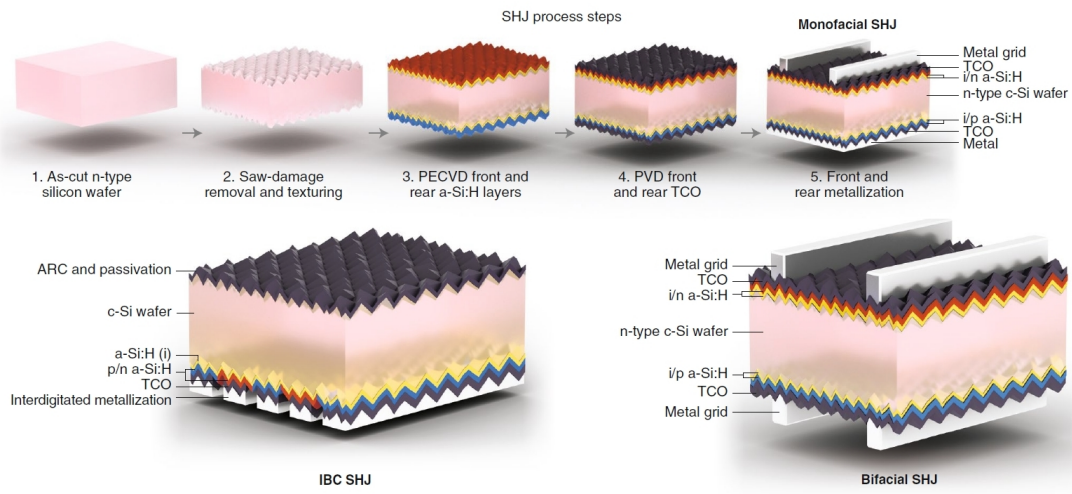


Figure 1.14: Fabrication steps of a SHJ²⁰.

1.7 Perovskite

The evolution of organic-inorganic lead halide perovskite solar cells (PSCs) began its notable journey in 2005 in the Peccell Technologies Inc. laboratory at Toin University in Yokohama, Japan. There, graduate student Akihiro Kojima joined the research group lead by Tsutomu Miyasaka to examine the possibility of using halide perovskites as a sensitizer on mesoporous TiO_2 electrodes for liquid electrolyte-based dye-sensitized solar cells (DSSC)²¹. At that time “perovskite” generally meant metal oxides having perovskite structures, i.e. a crystal with chemical formula ABX_3 , in which A and B are cations and X is an anion. In an ideal cubic structure, the B cation has a 6-fold coordination, surrounded by an octahedron of anions, and the A cation has a 12-fold cubooctahedral coordination. The cubic unit cell of such compounds is composed of A cations at cube corner positions, B sitting at the body-centre position, and X occupying the face-centred positions (fig. 1.15).

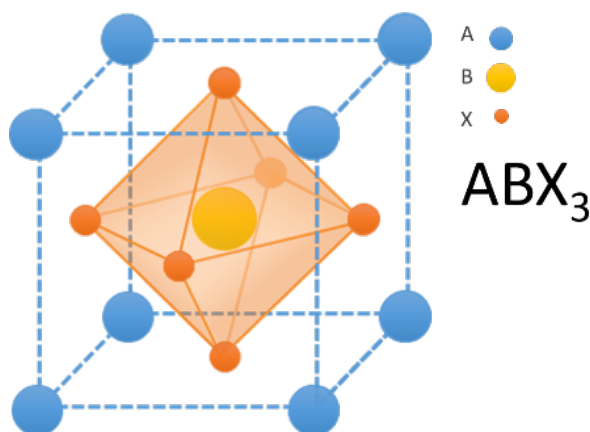


Figure 1.15: General perovskite unit cell. A and B are cations, while X is an anion.

The perovskite mineral was first discovered by Prussian mineralogist Gustav Rose in 1839²² in a piece of chlorite rich skarn. It was composed of CaTiO_3 and named after the renowned Russian mineralogist Count Lev A. Perovskiy (1792-1856). Many inorganic metal oxides were found to have the perovskite structure, BaTiO_3 , PbTiO_3 , SrTiO_3 , etc., but these compounds did not show good semiconducting properties that would make them good candidates for photovoltaic (PV)

applications. However, a class of halide perovskites containing a halide anion in place of the oxide anion, exhibits semiconducting properties that are desired for PV applications. In 1893, Wells et al. studied the synthesis of lead halide compounds from solutions including lead halide and cesium, CsPbX_3 ($X = \text{I}, \text{Br}, \text{Cl}$)²³, ammonium (NH_4)²⁴, or rubidium, RbPbX_3 ²⁵. Later, in 1957 Møller found that CsPbCl_3 and CsPbBr_3 have the perovskite structure^{26,27}.

It was Weber^{24,25}, that discovered that the organic cation methylammonium ($\text{CH}_3\text{NH}_3\text{NH}_3^+$) replaces Cs^+ to form $\text{CH}_3\text{NH}_3\text{MX}_3$ ($M = \text{Pb}, \text{Sn}, X = \text{I}, \text{Br}$) and reported the first crystallographic study on organic lead halide perovskite (fig. 1.16). From then on, it was Miyasaka's encounter with Kojima's supervisor, Dr. Kenjiro Teshima, which triggered the start of perovskite photovoltaics. The first perovskite-based solar cell utilized $\text{CH}_3\text{NH}_3\text{PbX}_3$ ($X = \text{Br}, \text{I}$) as sensitizer on a TiO_2 mesoporous electrode used in conjunction with a lithium halide-containing electrolyte solution²¹. Hypothesizing that the perovskite would perform the duty of a quantum dot sensitizer, perovskite was deposited via spin coating, with a solution molarity such to obtain the thinnest layer of nanocrystalline material, similar to a DSSCs. In 2009 the group managed to report a fabricated PSC with an efficiency of 3.8%²⁸. This was the beginning of an incredible story that has now reached a certified efficiency of 25.2%¹².

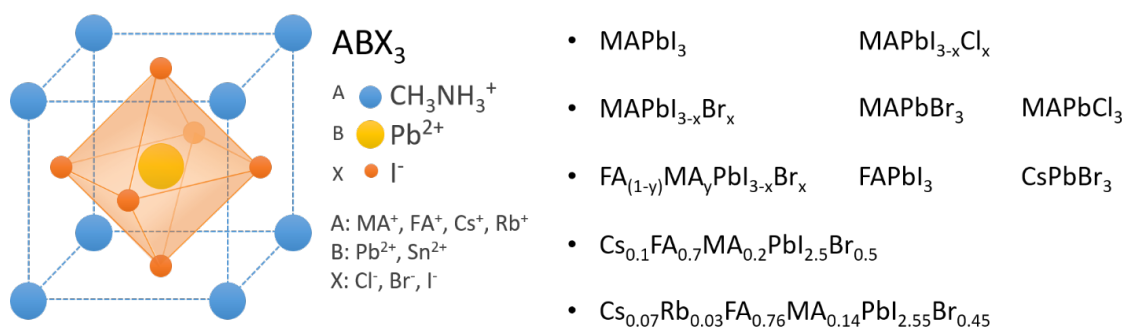


Figure 1.16: Different cation and anion combinations.

Some major milestones that radically changed the structure include the work of Michael Lee in 2012, at the time Ph.D. student in Henry Snaith's group at Oxford, where the first version of highly efficient, long term durable perovskite solid state solar cell with 10.9% efficiency was presented²⁹. The aim of the work

was to solidify the perovskite sensitized solar cell with a spin coated layer of an organic hole transporter (HTM), Spiro-OMeTAD (2, 2', 7, 7'-tetrakis(N, N-dimethoxyphenylamine)-9, 9'-spiro-bifluorene). Snaith et al. demonstrated that perovskite absorber of hundreds of nanometers on the surface of an insulating mesoporous Al_2O_3 scaffold can transport charges through its surface, substituting the previously employed TiO_2 (fig. 1.18). The electronically inert Al_2O_3 served as a base for the formation of perovskite absorber increasing its surface area and thus aiding in increased absorption. Indeed, a cell using this material exhibited higher voltage and PCE, a sign of the long diffusion length of carriers in the perovskite. This new concept of solar cell substantially differed from the idea of DSSC and was defined as meso-superstructured solar cell (MSSC) (fig. 1.17).

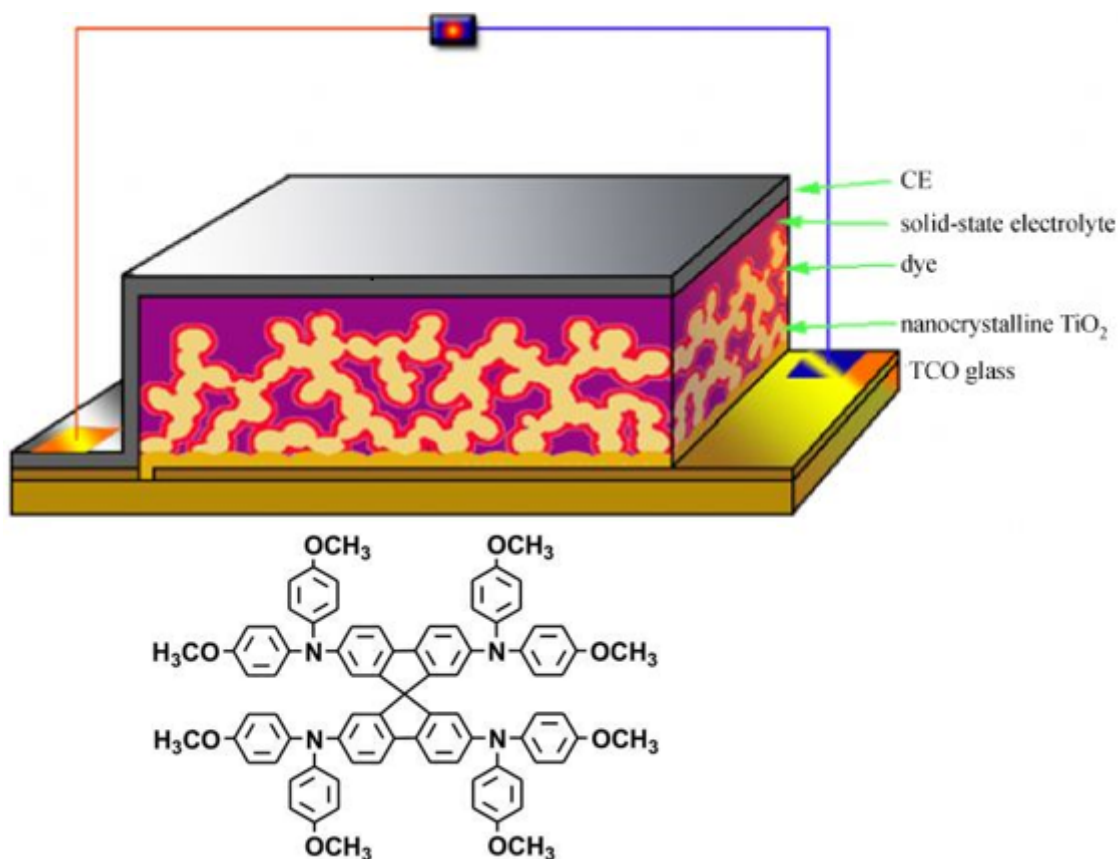


Figure 1.17: The meso-superstructured cell presented by Lee et al.²⁹ (top), the chemical structure of Spiro-OMeTAD (bottom).

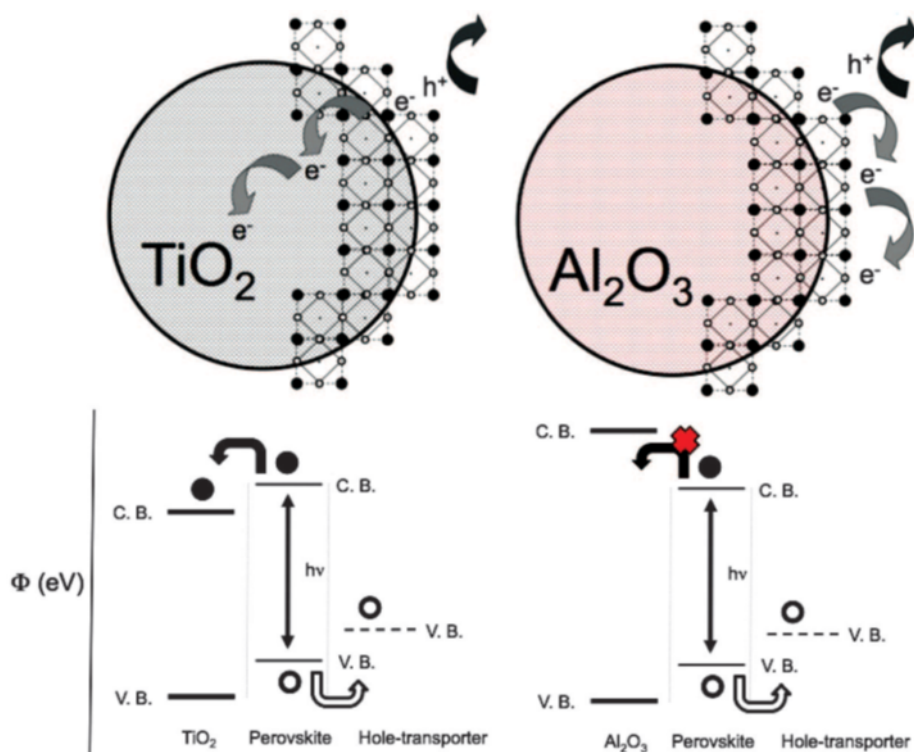


Figure 1.18: The different charge transport mechanisms between the perovskite-sensitized TiO₂ solar cell (left) and a non injecting Al₂O₃ based cell (right). A representation of the energy landscape is shown below, with electrons shown as solid circles and holes as open circles²⁹.

The next step was to move away from the requirement of a mesoscopic oxide layer. The perovskite material was found to have ambipolar transport characteristics, i.e they are able to transport electrons and holes to their respective selective contacts. Hence, the mesopores could now be filled with perovskites directly and only a capping layer was required. These devices produced efficiencies closer to 15%³⁰. Hereafter, the perovskite absorber layer made the mesoporous oxide completely obsolete and a planar architecture with the absorber sandwiched between ETL and HTL was realized³⁰. After that, Liu et al. proved that vacuum deposition was an alternative to deposit perovskite from solution, by co-evaporating methylammonium iodide and PbCl₂ on a compact TiO₂ to form a 300nm thick perovskite with 15.4% efficiency solar cell³¹. These two works defined the perovskite as per today, a thin film technology.

From there on, following studies have managed to bring the efficiency of PSC above the 25% threshold and the main reason is due to their extremely favourable physical and chemical properties. Due to the ionic nature of perovskite crystals, the absorption edge wavelength (band gap) can be freely modified by mixing I and Br or Br and Cl, forming mixed halide solid solutions ranging from $\approx 1.2 - 2.8eV$ ^{32,33}. When iodide is added to the perovskite structure, the absorption exhibits a constant red shift from the edge wavelength of $\approx 550nm$ for pure bromide, to $\approx 830nm$ for pure iodide³⁴ (fig 1.19).

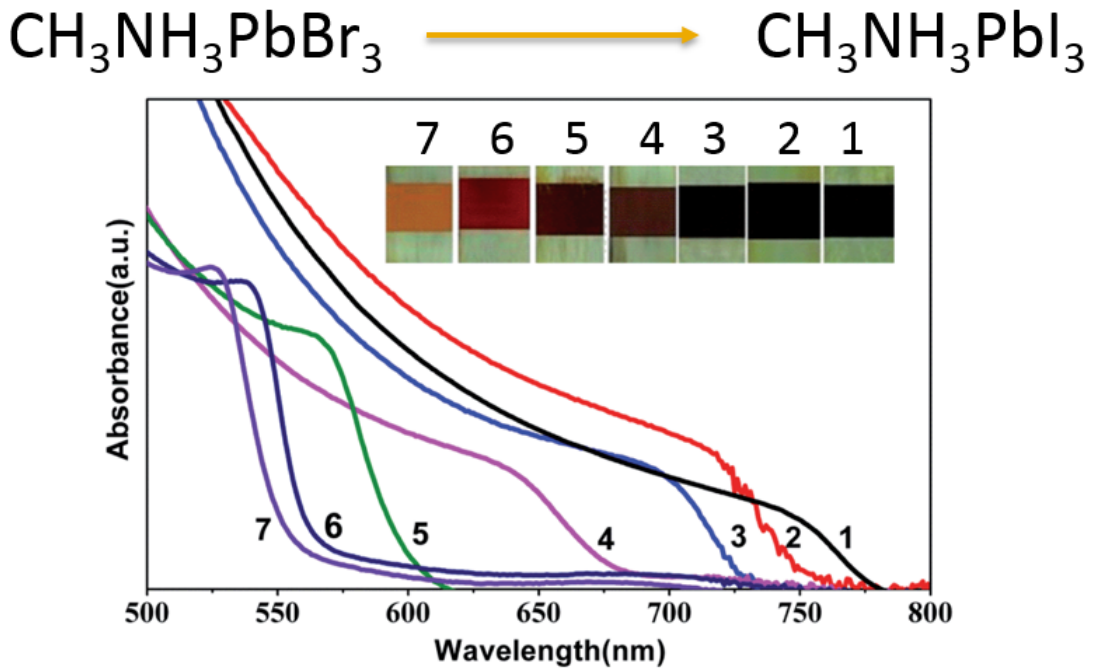


Figure 1.19: Depiction of the shifting absorption edge according to different I/Br content in the perovskite solution. Pure iodide perovskite (number 1) is dark colored and has a lower bandgap, $1.55eV$. Pure bromide (number 7), on the other hand is light colored as its absorption stops at $550nm$ ³⁵.

The strong edge wavelength and the broad flat absorption behaviour at shorter wavelength reflect the excellent optical properties useful for visible light optoelectronics³⁶. Density functional theory (DFT) of the standard perovskite absorber, $CH_3NH_3PbI_3$ (MAPbI₃) with $1.55eV$, shows a highly symmetric and therefore direct bandgap, where the strong contribution of the halide p-p electronic transitions from valence band (VB) to conduction band (CB) contribute to the exceptionally

high optical absorption coefficient of the material (10^5cm^{-1}) (fig 1.20)^{37,38,39,40,41}. Moreover, the unique defect properties of perovskite generate trap states that exist either within the bands (VB and CB) or exist as shallow traps near the CB and VB⁴². Carriers trapped in shallow defects can be detrapped easily and can contribute to current generation. This defect tolerance is reflected by the large carrier diffusion lengths, measured over the photoluminescence (PL) lifetime, which range from $1 \mu\text{m}$ (polycrystalline film fig. 1.21)⁴³ to over $100 \mu\text{m}$ (single crystal)⁴⁴.

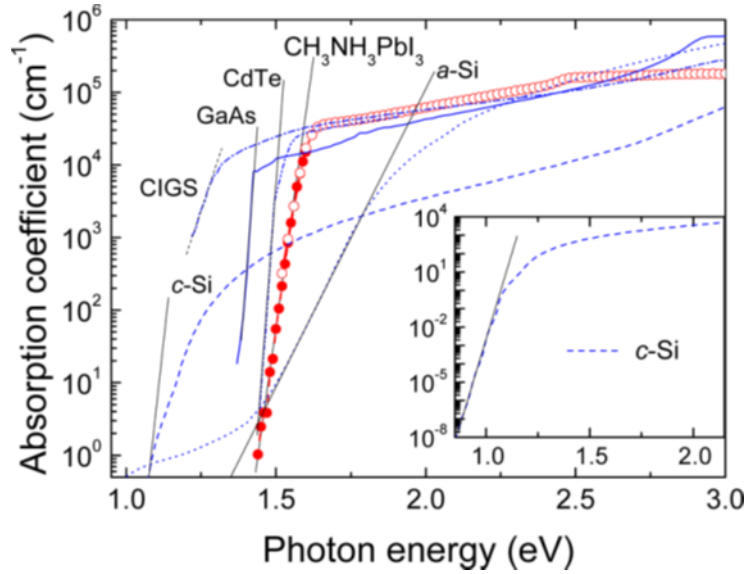


Figure 1.20: Absorption coefficients of different semiconductor materials. MAPbI_3 is highlighted in red⁴¹.

To summarize, the key factors that justify superior performance and high efficiency of PSCs are the following: 1) high optical absorption coefficient that enables the use of thin film, 2) long carrier diffusion length and suppressed recombination due to defect tolerance, 3) well balanced charge transfer. In PV applications, quality number 2, leads to generation of high voltage ($1.1 - 1.2\text{V}$)⁴⁵. The open circuit voltage (V_{oc}) of all types of solar cells suffers from a large thermal loss because of its band gap energy (E_g). However, PSC can harvest light more efficiently due to their high E_g and the high V_{oc} is maintained even under weak light intensity. Indeed, it is the ability to collect light efficiently in the blue part of the solar spectrum that allowed PSC to be implemented in tandem solar cells successfully.

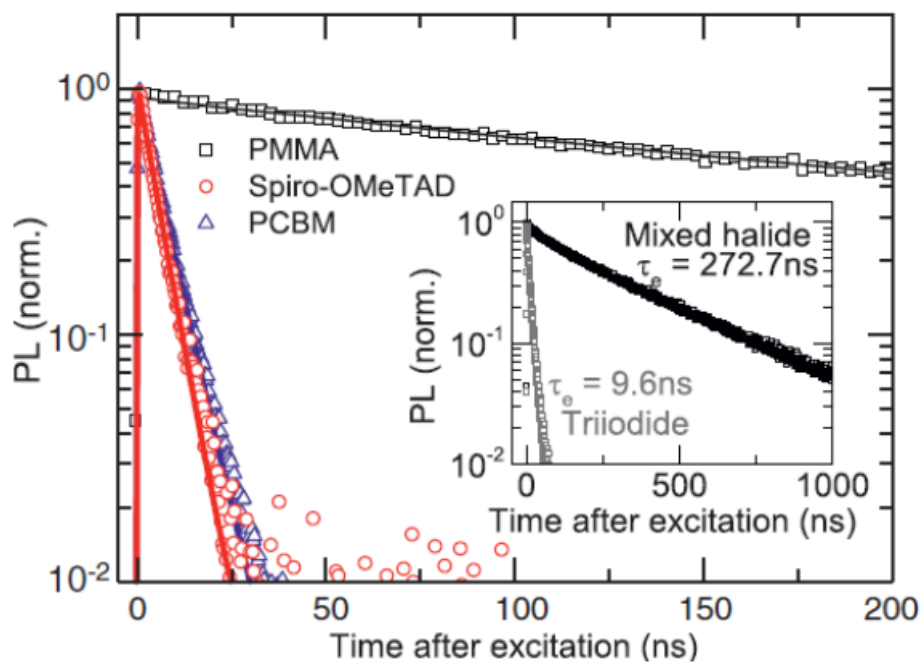


Figure 1.21: Photoluminescence measurement of a polycrystalline perovskite film according to Stranks et al.⁴³.

1.8 Tandem Solar Cells

The idea behind a tandem solar cell is to employ two active absorber materials to make better use of the solar spectrum. Since absorption is a threshold mechanism and one material can only absorb photons with energy above their E_g , having multiple active layers that can absorb different parts of the solar spectrum is convenient. For this reason, the tandem solar cell is composed by two or more sub-cells, and each sub-cell must be complementary in the absorption of light, avoiding competitive absorption. The ideal tandem architecture is obtained when there is minimum to no absorption overlap between the materials of the solar cell, meaning that each sub-cell can efficiently harvest different wavelengths of the incoming light. There are different ways to fabricate a tandem solar cell: mechanically stacked four-terminal (4T) where top and bottom cell are operated separately, and 2-terminal monolithic tandem (2T) (fig. 1.22). In this work, we present solar cells built following the latter configuration⁴⁶.

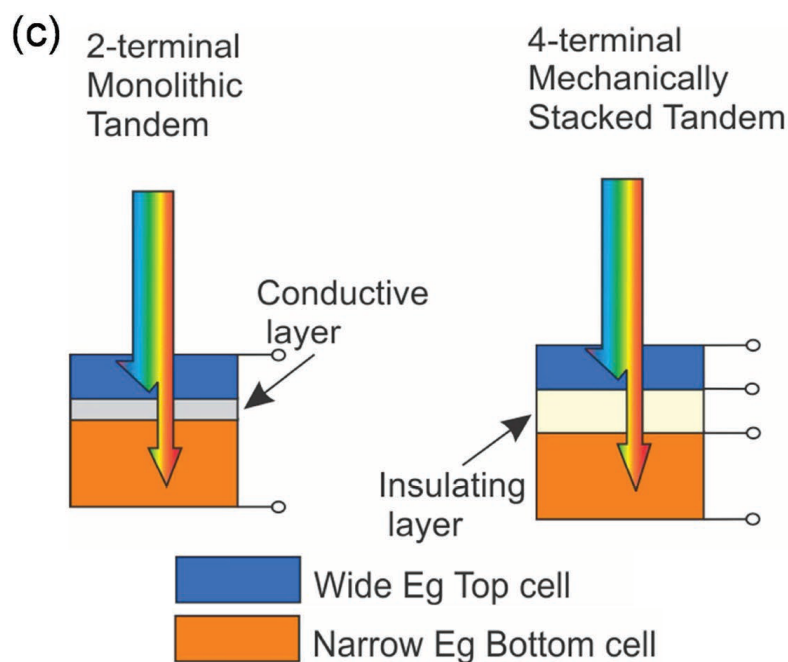


Figure 1.22: Diagram of the 2T and 4T tandem solar cells⁴⁷.

From an electrical point of view, a 2T tandem solar cell can be described

as two single junction solar cells that are connected in series. This implies that the resulting V_{oc} is the sum of the respective top and bottom V_{oc} 's, whereas the final J_{sc} will be limited by the solar cell that produces the lowest current. This last point highlights immediately a major problem of tandem solar cells: current matching. If either the top or the bottom cell produce less current than the other cell, that current is lost, leading to power loss and lower efficiency than the device's potential. 2T tandems require also compatibility between every processing step with all preceding layers and interfaces, making this configuration more challenging to develop.

Indeed, parasitic absorption between the different materials must be considered. For example, two main reflection losses occur at the front transparent electrode and the smooth surfaces. To address these problems it is possible to deposit quarter length anti reflecting coatings like LiF or MgF_2 ^{48,49} at the top of the tandem solar cell, and use textured surfaces to enhance light trapping⁵⁰. Parasitic absorption originates from photons that are absorbed in any other layer apart from the active material: the difference between EQE curve and absorbance spectrum can be used to experimentally characterize this type of losses⁵¹. The primary parasitic absorption occurs at the transparent electrode (TCO) and it is induced by free carrier absorption. This implies that a lower carrier concentration in the transparent electrode will mitigate parasitic losses, but this increases the sheet resistance and corresponding electrical loss. Solutions to this problem usually involve thinning down the TCO⁵² or moving to an electrode with lower carrier concentration but large carrier mobility: going from the common Indium Tin Oxide (ITO) to Indium Zinc Oxide (IZO). Despite the complex realization, the tandem architecture has the best potential to reach high practical efficiencies and lower levelized costs of electricity. This, thanks to fewer substrates and transparent contacts, compared to the 4T counterparts^{53,54}, which require more layers and are also more costly to produce.

The most intuitive structure of a tandem solar cell envisions a top cell composed of a material with a wide bandgap in order to harvest light in the blue end of the solar spectrum, in combination with a bottom cell made of a low bandgap absorber to collect the red end (fig. 1.23). In this way the highly energetic photons at short wavelengths are efficiently absorbed, generating high voltage and reducing

thermalization losses, leaving the bottom cell to absorb the transmitted low energy photons of the near infrared (NIR).

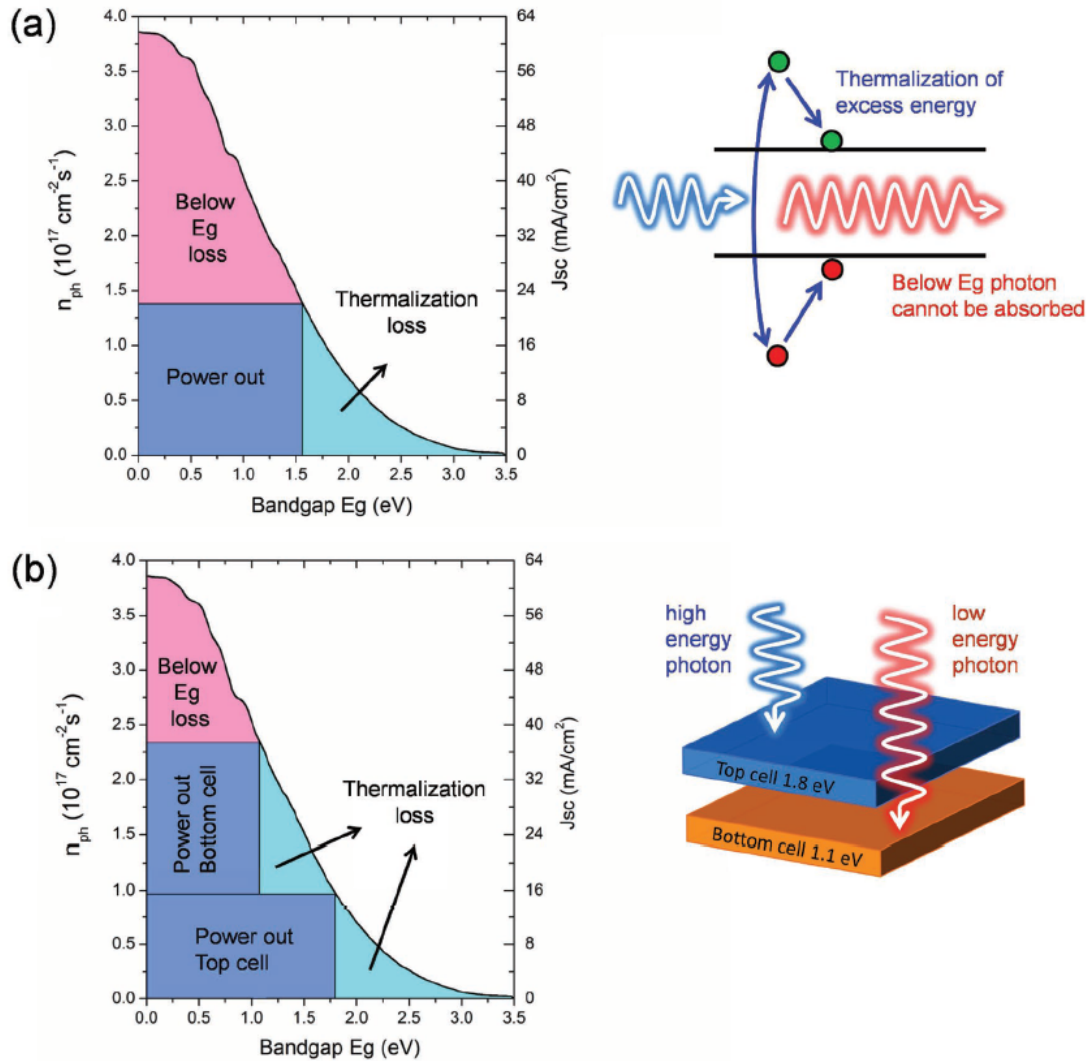


Figure 1.23: Thermalization loss and below- E_g loss of a) a single junction solar cell with E_g of 1.55 eV and d) dual junction tandem solar cell with 1.8 eV E_g top cell and 1.1 eV E_g bottom cell⁴⁷.

Candidates for the bottom cell are Silicon (Si), Copper Indium Gallium Selenide (CIGS), Cadmium Telluride (CdTe), etc. solar cells. The ideal bottom cell in a tandem configuration requires good response in the NIR light (for good current matching) and good passivated surface to compensate the small band gap

and V_{oc} . Currently, the best candidates lie in the III-V semiconductors category. However, these materials are too expensive for terrestrial application. Therefore, silicon heterojunction (SHJ) solar cells represent the most promising candidates for efficient 2T tandems^{51,49}. However, the SHJ is unstable at temperatures above $200^{\circ}C$, limiting the upper tandem technology to low temperature processes. To this end, perovskite solar cells (PSC) are perfectly suitable as top cells. Owing to their high efficiency, cheap processing, and tunable bandgap, this material has shown promising results as top cell in a 2T tandem configuration reaching record efficiencies of 29.15%¹² with various deposition techniques. Additionally, PSCs can now be deposited on textured surfaces with solution based processes, such as spin coating (fig. 1.24), while still achieving respectable certified efficiencies of 25.7% and lowering their fabrication cost even more⁵⁰.

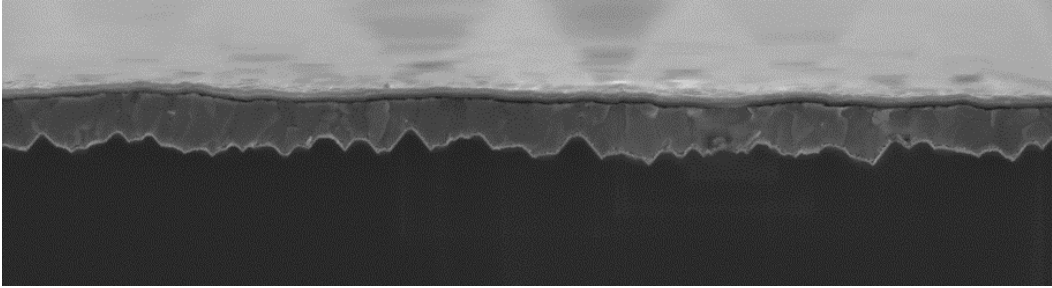


Figure 1.24: SEM cross sectional image of a solution processed perovskite layer deposited on top of textured silicon.

The SQ theory applied to the tandem cell tells us that an efficiency as high as 46% is achievable⁵⁵, which is not too far away from today's certified devices¹². For perovskite/silicon tandems, efforts are being put into reaching and overcoming the 30% mark, be it carefully tuning the thickness and choice of interlayers or through compositional engineering of the top cell. PCSs used in the current generation of tandems have been put under the spotlight for their sub optimal performance when compared to the state-of-the-art single junction solar cells. V_{oc} values are $\approx 200mV$ lower in tandem devices than the best performing single junction cells⁵⁶, and the Fill Factor (FF) too is lower in the latter configuration compared to the first one. If tandem cells could reach the same technological advancement as other mature manufactured photovoltaic technologies, which have achieved cell efficien-

cies that are around 85% of their respective SQ limits (such as Si and GaAs)¹², they would achieve efficiencies above 36%. This can be feasibly achieved by pairing wide bandgap (1.65 – 1.8eV) PSC with Si. Unfortunately, experimental results show that for an absorber with a bandgap of 1.75eV, with a theoretical maximum current density of $\approx 22\text{mA}/\text{cm}^2$, the highest recorded value is $\approx 19.7\text{mA}/\text{cm}^2$ ^{257,58,59}. Coupled with a V_{oc} of 1.41eV^{60,61} and a FF of 0.83 operating at 92% of its detailed balance efficiency limit^{62,63} we would obtain a PSC top cell of 23,2% efficiency. Which would then lead to a possible tandem efficiency of 35.2%¹⁵.

To push the efficiency of PSCs, the key is obtaining a stable wide bandgap perovskite, though researchers have been obstructed by the aforementioned problems: intrinsic instability, degradation, phase segregation. However, there is also another route to increase the power output of photovoltaic devices while relying on the more performing lower bandgap perovskites: bifacial tandem solar cells.

1.9 Bifacial Solar Cells

In the bifacial tandem, the rear electrode is transparent, enabling diffused and reflected light to enter the device. This is opposite to conventional (monofacial) tandems, where the rear electrode consists in an opaque layer of metal. All the light components other than direct light, such as the diffused or reflected light, are conventionally defined with the term albedo. Similar to the direct light, even the albedo can be exploited for power generation, paving the way for new technology to push the device efficiency higher^{64,65}. The concept of a bifacial solar cell that exploits the direct and albedo light is well established in silicon photovoltaics^{66,67,68} and crystalline silicon (c-Si) bifacial solar cells are now entering the photovoltaic market.

In a perovskite silicon tandem, the bifacial concept offers the possibility to further increase the power output by boosting the current generation⁶⁹. Indeed, on a performance level, the major difference between the monofacial tandem and the bifacial is the current matching. In the monofacial case, as discussed before, current matching between perovskite and silicon is required to maximize the power output of the total cell. Any mismatch would create power losses. In the bifacial case, instead, we can purposely design a mismatch condition, where the top cell (perovskite) has a smaller bandgap to generate more current. This would limit the bottom cell (silicon) due to the competitive absorption. However, thanks to the bifacial concept, the bottom cell can compensate the lack of photons from the front with the albedo from the back. In turn, this results in a strong enhancement of the current output and consequentially the absolute power. Figure 1.25 summarizes the differences between the monofacial and bifacial concepts, with the predicted current generation.

Thanks to the bandgap tuning proper of perovskites, we can go from a bifacial device heavily limited by silicon, with light coming only from the top, to a bifacial device now limited by the perovskite when there is light also entering from the bottom. In contrast, an already perfectly matched solar cell will not show any J_{sc} increase even in the presence of albedo. In light of this, what determines the amount of J_{sc} gain, and consequently the new power output, is the bandgap of the perovskite solar cell (PSC): a narrow bandgap equates to a higher generated

current, whereas a large bandgap results in less current. This means that in our bifacial case, in contrast with the research direction of the tandem community¹⁵, it is actually beneficial to work towards a stable and efficient narrow bandgap perovskite in order to push back the current matching point and make the best out of the albedo radiation. More in detail, we can see from simulations⁷⁰ that with increasing albedo, the optimal bifacial device performance is met at significantly lower bandgaps. In this work, we go over the results obtained from fabricating perovskite/silicon bifacial tandem solar cells via solution processing. We then measure such devices with solar simulators in the laboratory and also show data obtained from outdoor test fields.

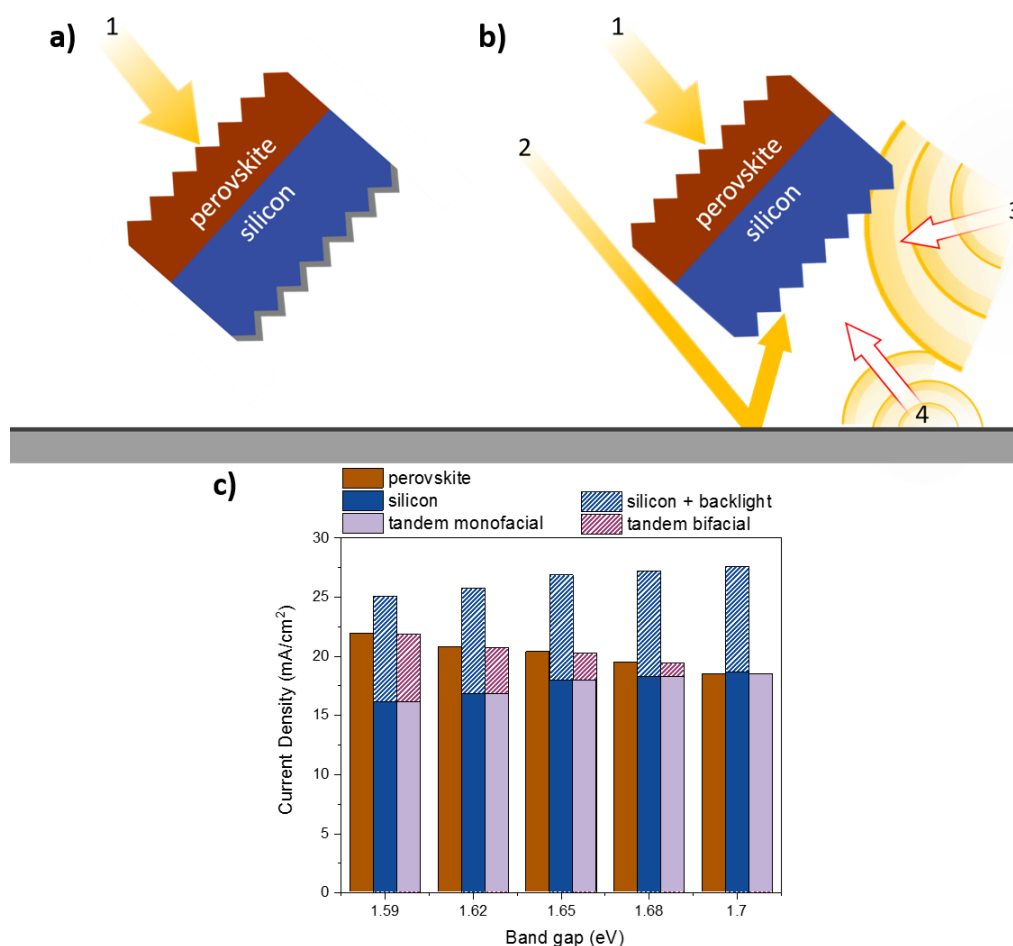


Figure 1.25: Difference between a) a monofacial tandem, which collects light only from the front; b) a bifacial tandem that is able to gather light even from the rear electrode; c) histogram illustrating the predicted currents.

Chapter 2

Device Fabrication

We now delve into the device fabrication part, reporting all the steps required to complete our bifacial solar cell. The device is similar to a 2T tandem solar cell, since it functions with two photoactive absorber layers connected in series. As mentioned in the previous chapter, the tandem aims to harvest more efficiently the solar spectrum than a single junction solar cell, though with an extra twist, i.e. it can also collect sunlight from the surroundings, albedo, because it has a transparent electrode on the rear side. Following the fabrication protocol, we first report the fabrication processes for the bottom SHJ, then the top perovskite cell.

2.1 The Bottom Cell

Silicon SHJ bottom cells are fabricated on float-zone double side-textured four inches wafers (TOPSIL, n-doped, resistivity $1 - 5\Omega/cm$, thickness $250 - 280\mu m$). Originally, the silicon wafers are bought double sided mirror-polished. To reduce the reflection losses induced by the polished surface, the wafers are textured with random pyramids, a standard procedure in silicon solar cell fabrication²⁰. The texturing process is done in alkaline solution. By controlling the alkaline concentration, temperature and processing time, we optimized the pyramid size to accommodate the perovskite top cell and to reduce the reflection losses⁵⁰. After the texturing process, the wafers are cleaned in RCA1 and RCA2 solutions. RCA1 is used to remove organic contaminants, by oxidation of the wafer surface

in a $\text{NH}_4:\text{H}_2\text{O}_2:\text{H}_2\text{O}$ solution at 75°C . The RCA1 oxide layer is then stripped in a hydrofluoric acid HF solution. After RCA1, RCA2 is used to remove metal contaminants, again by oxidation of the wafer surface in a $\text{HCl}:\text{H}_2\text{O}_2:\text{H}_2\text{O}$ solution at 75°C . Finally, a second HF solution is used to remove the RCA2 oxide layer.

The clean and textured wafers can now be moved in the PECVD/PVD cluster, the Octopus2 from Indeotec. Firstly, we passivated the silicon surfaces by depositing 8nm thick layer of amorphous intrinsic *i* silicon on both sides of the wafers, using SiH_4 as gas precursor. Subsequently, we deposited 6nm of *n* and 13nm of *p* doped amorphous layers on the top and bottom, using a mixture of $\text{SiH}_4:\text{PH}_3$ and $\text{SiH}_4:\text{TMB}$ gases, respectively. Secondly, we deposited via RF magnetron sputtering, the recombination junction (RJ) on the top and the bottom contact on the rear. For the RJ, we sputtered 15nm of ITO (Vital Thin Film materials – 97% In_2O_3 3% SnO_2), while for the bottom contact 150nm of ITO. For these depositions, the base pressure is $1 \times 10^{-5}\text{Torr}$, 13.56MHz RF source, $0.9\text{W}/\text{cm}^2$ power density, in an Ar/O_2 atmosphere (0.8% O_2 content) and the process pressure is $1 \times 10^{-3}\text{Torr}$. The ITO sputtering is done with the use of masks to define the recombination junction ($\approx 1\text{cm}^2$) between the bottom and top cell. For each wafer, we fabricated seven bottom cells.

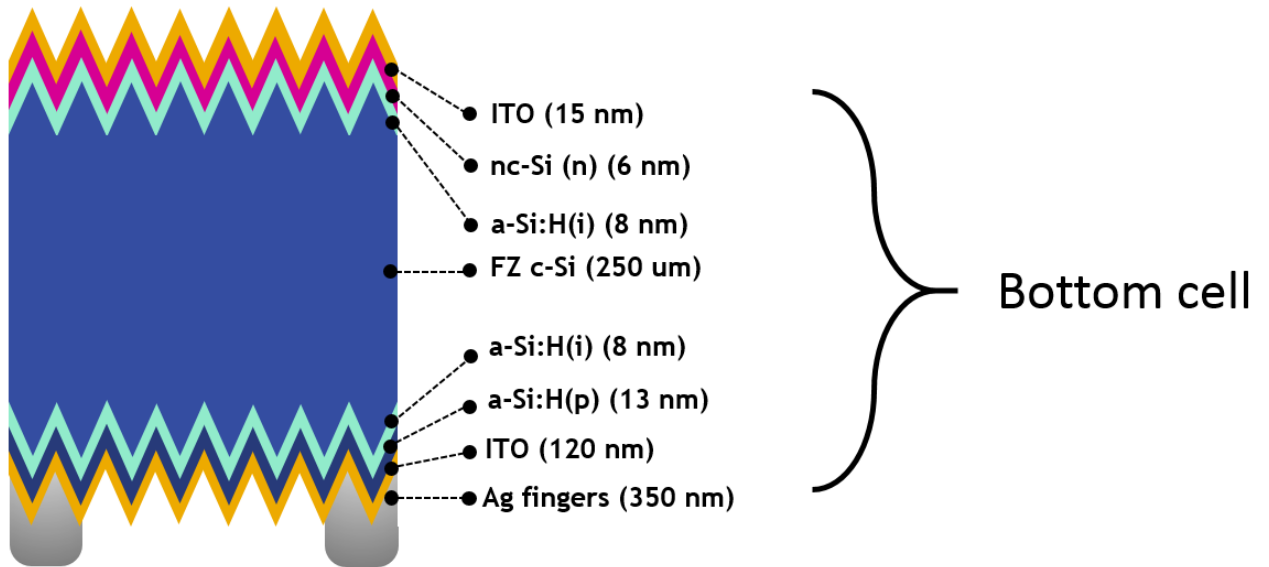


Figure 2.1: Complete structure of the SHJ bottom cell of our bifacial tandems.

The bottom SHJ cell of our bifacial tandem is now complete (fig. 2.1) and as a final step we annealed the wafers at 200°C for 5 min to recover the sputtering damage of the PVD on the amorphous layers.

2.2 The Top Cell

The top cell fabrication consists in the deposition of the perovskite and the intermediate layers that are necessary to make the bifacial functional. The perovskite top cell is in *p-i-n* configuration. Therefore, the first layer deposited on the RJ is 17nm of nanocrystalline NiO_x as the hole transport layer (HTL) via RF sputtering (Angstrom EvoVac sputtering tool). The process is done at base pressure of $< 1 \times 10^{-6}\text{Torr}$ in pure Ar atmosphere with no intentional heating or cooling of the substrate. The target, 99.9% NiO Plasmaterials, was sputtered at power density $1.97\text{W}/\text{cm}^2$ and 13.56MHz RF source.

After the deposition, the NiO_x is passivated with a carboxylic acid to reduce the surface defects⁷¹. Next, the perovskite precursor solution was prepared for spin coating deposition. The perovskites utilized in our bifacial cells contain three cations: cesium (Cs), fomamidinium (FA) and methylammonium (MA). For anion we have iodide (I) and bromide (Br). We prepared perovskite compositions with different band gaps, that means we utilized different ratios of I and Br for each precursor solution, while keeping the cationic part the same. To prepare 1.68 M solutions we mixed 36.4mg of caesium iodide (CsI, Alfa Aesar), $44,8\text{mg}$ of methylammonium bromide (MABr, Greatcell), 389mg of fomamidinium iodide (FAI, Greatcell), lead bromide (PbBr_2 , Sigma Aldrich) and lead iodide (PbI_2 , Alfa Aesar) in $1,646\text{ml}$ solution made of dimethylformamide (DMF) and dimethylsulfoxide (DMSO) (4:1 v/v). The solution was stirred until complete dissolution of the precursors. Depending on the desired bandgap we mixed PbI_2 and PbBr_2 accordingly, see table 2.1.

Bandgap (eV)	PbI ₂ (mg)	PbBr ₂ (mg)
1.59	1198	73.4
1.62	1107	154
1.65	1000	236
1.68	922	293
1.70	829	367

Table 2.1: PbI₂/PbBr₂ quantities used to obtain the perovskite solution with desired bandgap.

For the perovskite film formation, $75\mu\text{l}$ of perovskite precursors is spin coated on the bottom cell substrate. An initial 600rpm step is maintained for 6s , succeeded by another at 2000rpm for 54s , followed by a last step at 7000rpm for 8s . Between these last two, there is a 3s ramp that gradually brings the speed from 2000rpm to 7000rpm . During the acceleration phase, we steadily drop $300\mu\text{l}$ of anisole as solvent quencher. This process is used to extract the low boiling point solvents DMF/DMSO from the perovskite solvates, allowing the crystallization on the textured bottom cell. Finally, the forming film is allocated onto a hot plate at 100°C for 10 minutes. With this spincoating technique we are able to achieve micrometer-thick perovskite that covers entirely the silicon pyramids (fig 2.2). The whole process is done in the nitrogen filled glovebox.

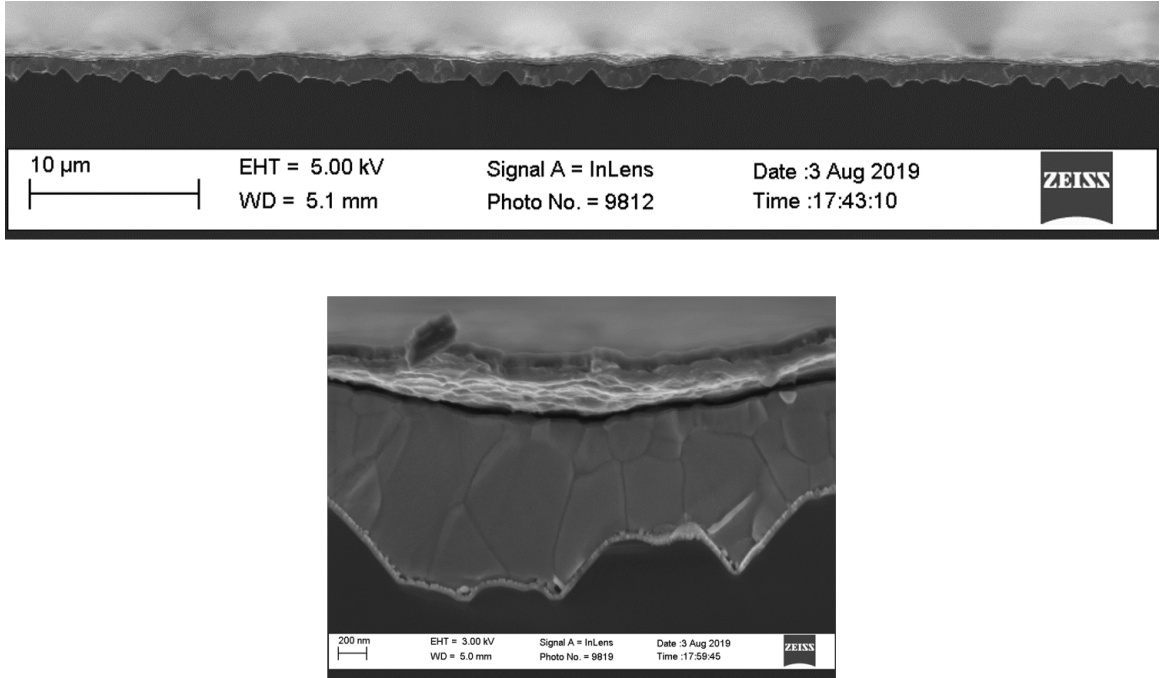


Figure 2.2: SEM cross sections of a perovskite layer deposited via spincoating on top of textured silicon.

After the perovskite layer is formed, we transferred quickly the bifacials to another glovebox where we deposit the electron transport layer (ETL) stack composed of lithium fluoride (LiF) (1nm , 99.85%, Alfa Aesar) and C_{60} (20nm , > 99.95% NanoC). The two are thermally evaporated in an Angstrom EvoVac evaporation system without breaking vacuum in between (base pressure $< 1 \times 10^{-6} \text{Torr}$, evaporation rate of $0.1 \text{\AA}/\text{s}$ for LiF and of $0.2 \text{\AA}/\text{s}$ for C_{60} as measured by quartz crystal monitors, quartz crucibles, no intentional heating or cooling the substrate holder). From there we transfer the cells to the Picosun cluster for thermal atomic layer deposition (ALD) of 20nm of SnO_x buffer layer. The buffer layer is required to protect the perovskite from the sputtering damage of the top electrode (see below). The ALD- SnO_x buffer layer is deposited with a thickness between $18 - 20\text{nm}$ (134 cycles). We used Tetrakis(dimethylamino)tin and H_2O as precursors, with N_2 as the gas carrier.

After the buffer layer deposition, the bifacials are again exposed to air when they are then prepared and masked to define the active for the top electrode deposition. We carefully aligned manually the front transparent conductive oxide

(TCO) with the recombination junction defined by the ITO previously deposited with the PVD. As top electrode we sputtered 110nm indium zinc oxide on top of the buffer layer in an Angstrom EvoVac sputtering system (base pressure $< 1 \times 10^{-6}\text{Torr}$) with RF power of 42W (90% In_2O_3 /10% ZnO , 99.9% Plasmaterials, source to substrate distance is 10cm). To functionally contact the top and bottom transparent electrodes, we evaporated silver contacts, on the front and afterwards on the rear of our bifacials. To provide light absorption from the rear side, we do not to cover completely the rear TCO. For this reason we use the same shadow mask for the front and the backside of the cells (fig. 2.3). We employ 350nm of Ag to create the bus-bars and fingers to gather the generated charge carriers. The two depositions are both done with an Angstrom EvoVac thermal evaporator (base pressure $1 \times 10^{-6}\text{Torr}$) with a rate of $2.5\text{\AA}/\text{s}$ as measured by quartz crystal monitors. Lastly, we deposit 95nm of MgF_2 as antireflection film evaporated with the same previous system (Plasmaterials, $> 99.9\%$, $1\text{\AA}/\text{s}$ as measured by quartz crystal monitors, base pressure $< 1 \times 10^{-6}\text{Torr}$). Our bifacial tandem top cells are now complete (fig. 2.4) and can now be measured with an in house solar simulator. Figure 2.5 summarizes all the device fabrication process.

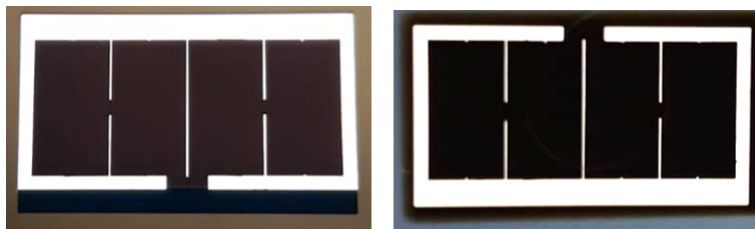


Figure 2.3: Picture of the front (left) and the back (right) electrodes of our bifacial tandems.

The scanning electron microscopy (SEM) images of the bifacials, and here reported throughout this work, were collected at 5kV accelerating voltage with 30mum beam aperture, using a Zeiss Auriga microscope equipped with an in-lens detector.

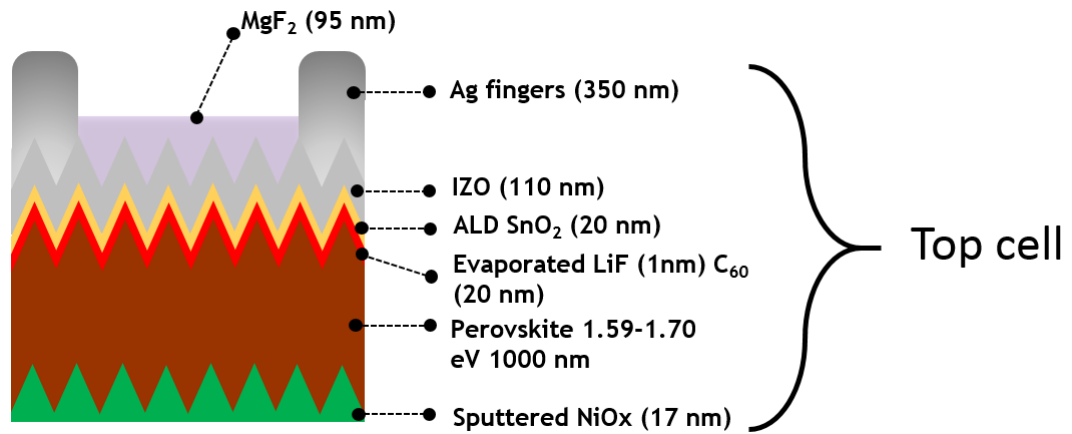


Figure 2.4: Complete structure of the perovskite top cell of our bifacial tandem solar cells.

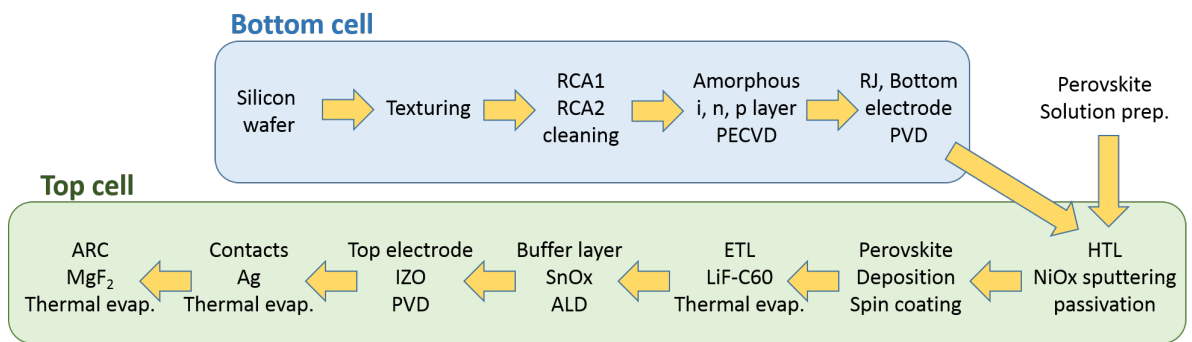


Figure 2.5: Diagram summarizing the entire device fabrication process.

2.3 Measurement Setup

Once the bifacial tandems are completed, we evaluated the performances in “monofacial mode”, i.e. using only front (top cell side) illumination. This is done as an initial evaluation of the efficiency of the solar cells, in order to discriminate successful devices from failures. To do this, we used a Wavelabs Sinus 220 LED based solar simulator with AM1.5G irradiance spectrum as our light source and we coupled it with a Kiethley 2400 series SourceMeter to take the J-V measurements. The data is recorded via a homemade MATLAB based software. The solar cells are measured from $-0.1V$ to $+1.9V$ at $200mV/s$ in both forward and reverse scan directions and the illuminated area, defined by a laser cut shadow mask, is $1.03cm^2$. For stabilized power measurements we use a homemade LabView based software to track the cell efficiency while it is held at maximum power-point voltage for $10min$. To calibrate the Wavelabs we used a Fraunhofer reference solar cell before each measurement session.

EQE measurements are performed using PV-Tools LOANA equipment. When measuring bifacial tandem devices, we must light bias the system in order to separately collect EQE from the top or bottom sub cells. To get a signal out of the perovskite top cell, we use IR LEDS ($930nm$) to saturate the silicon’s response; vice versa to obtain the bottom cell data, the tandems are biased with blue LEDS to saturate the perovskite. To measure in near short circuit conditions for each case, MPP voltages are applied on the devices. In this way we can integrate the EQE curve to obtain another take on the photo generated current produced by the two sub cells and compare the result with the J_{sc} recorded via the Wavelabs and Keithley. All device characterizations have been performed at ambient air with $RH \approx 50\%$ and without any encapsulation.

After recording the device efficiency our tandems in monofacial mode and collecting EQE data and SEM images (where required), we measure them in “bifacial mode”: with light shining on both sides of the solar cell. To achieve this, we have utilized two different solar simulators: Abet Technologies Sun 3000 Class AAA and Newport Oriel Sol3A Class AAA, both xenon (Xe) arc lamp based. The two are arranged vertically and pointing towards each other as seen in figure 2.6. In the middle we use a black coated board as sample holder with an aperture ($4cm^2$)

in the centre to allow the solar cell to see both simulators: the perovskite facing down towards the Abet, the silicon facing up towards the Oriel. During all our measurements, the Abet is kept fixed at 1 sun ($100\text{mW}/\text{cm}^2$), while the Oriel's intensity is varied via the use of its dedicated power supply. Calibration of both solar simulators is done with the Fraunhofer reference SHJ cell, and it is done before each measurement session. To record the data, we again couple the system with a Keithley 2400 SourceMeter and use the same two software to obtain J-V curves and stabilized power tracking with the same procedure as mentioned before. In addition, we take J-V measurements at different back light intensities, i.e. the Oriel, to study the effect of additional rear side illumination on the overall performance of the solar cell.

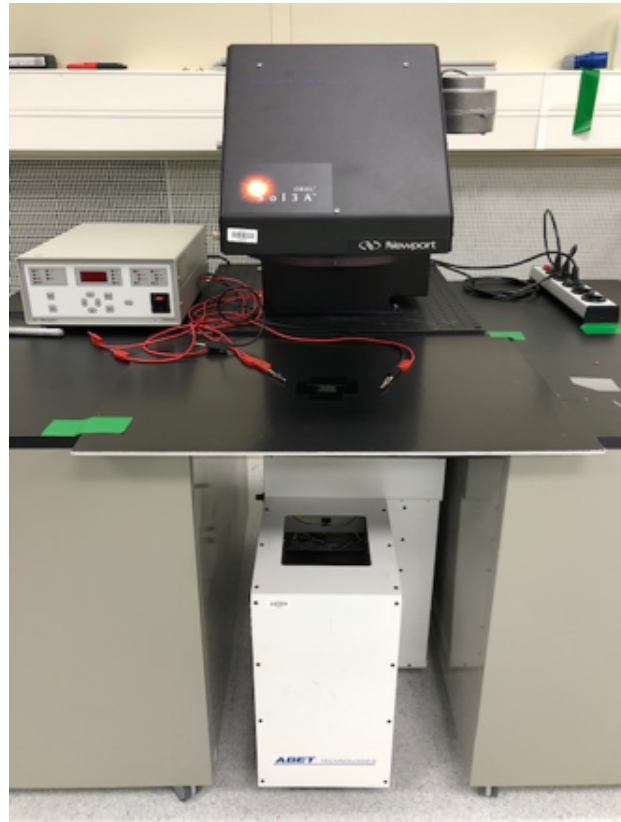


Figure 2.6: Photo of our Abet (at the bottom in white) and Oriel (on top in black) setup to measure the bifacial tandems. The solar cells are places on the black board in the middle of the two simulators.

2.4 Device Encapsulation

For bifacial measurements involving the Abet/Oriel setup and later for outdoor testing and operational stability, we first encapsulate the tandems using an industrial vacuum laminator Ecolam 5 Ecoprogetti. During this study we have tested different encapsulation methods and materials to eventually settle with glass/butyl rubber, as it guaranteed the highest success rate. To prepare the bifacials for encapsulation we first utilized a millimetre wide tabbing wire to extend two contacts out of the glasses. Screen printing Ag-paste was employed to assure conductivity between the wire and the bus-bars of the devices. After a 5 minute annealing to degas the paste, the contacted solar cells are placed on a $7 \times 7\text{cm}$, 3mm thick, glass previously prepared with butyl rubber strips along the edges. We use an identical glass/butyl rubber combination to close the bifacial on top. The bundle is then placed inside the vacuum laminator, which then seals the device at 100°C under vacuum for 10 minutes. Once the procedure is finished, the bifacials are now encapsulated, with two contacts coming out as shown in figure 2.7, and is ready to be measured.

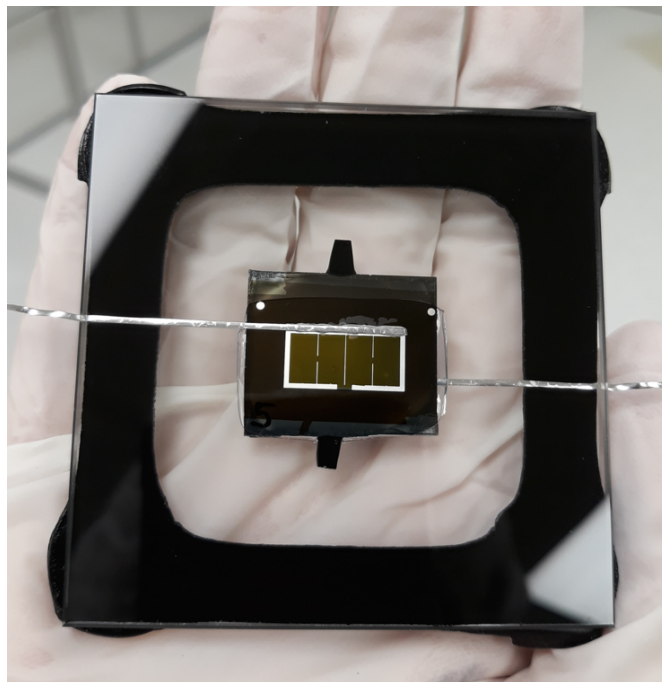


Figure 2.7: Photo of a bifacial solar cell encapsulated with glass/butyl rubber.

2.5 Outdoor Testing

Once the bifacials have been measured in the laboratory with the Abet/Oriel setup, we took the devices to the in-house test field to evaluate the efficiency under real conditions. To acquire photovoltaic data, we use an I-V tracer from EKO (model MP-160). The I-V characteristics of multiple samples are probed successively using the multiplexers MI-520 again from EKO. Current-voltage curves are acquired with a scan rate of $200mV/s$, and we measure all physical parameters with a time interval of 10 min. The electronic equipment is kept inside a cooled house at $23^{\circ}C$ and data acquisition is performed with a computer running EKO's MP160 software. The global horizontal irradiance on the plane of the devices is measured using the pyranometer MS-802 (EKO), which is mounted on the same structure as the devices. The solar cells are mounted on a structure with a tilt angle of $^{\circ}25$ and South orientation and it's located in KAUST's outdoor testing field on the KAUST campus, near the village of Thuwal (Saudi Arabia; 22.302494, 39.110737). Furthermore, solar spectra is acquired using the spectrometers QE65PRO (visible spectral region) and NIRQuest512 (NIR spectral region) from Ocean Optics. The spectrometers are built into a temperature-controlled housing and possess a wavelength resolution of $< 2nm$ across the entire VIS/NIR.

2.6 Bifacial Stability Characterization

For operational stability measurements, we take the previously encapsulated bifacial solar cells and keep them in the dark inside a Shel Lab 1445 oven at 85°C , with a relative humidity of $\approx 40 - 50\%$ and measure them at room temperature over time under AM 1.5G 1-sun condition. This test last 1000 hours. We also tested the device's response under illumination at MPP condition. To do that, we keep the devices continuously irradiated under a metal halide discharge lamp (Osram Powerstar HQI, 900W) in air. The lamp intensity is calibrated so the bifacial's J_{sc} is equal to the one measured under spectrally matched AM 1.5 G light. J-V curves in both scan direction are taken every 10 min at 100mV/s from -0.1V to 1.9V and vice versa. Between the measurements, we keep the bifacial solar cell at the maximum power point voltage, which is determined by the most recent J-V scan. This test last 500 hours. The light spectrum is reported in figure 2.8.

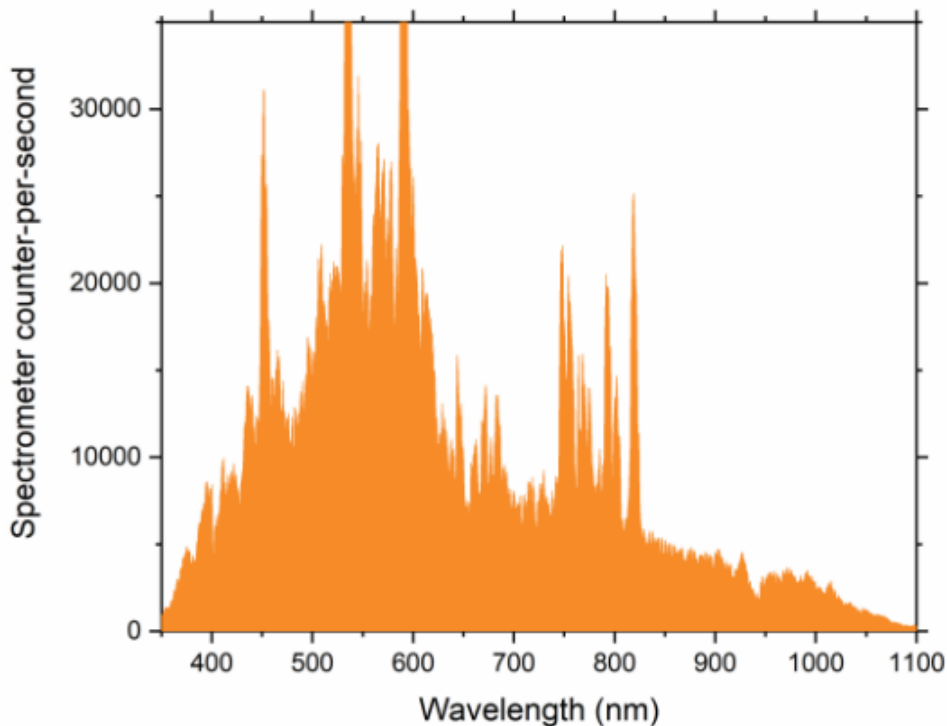


Figure 2.8: Spectral output of operational stability setup.

Chapter 3

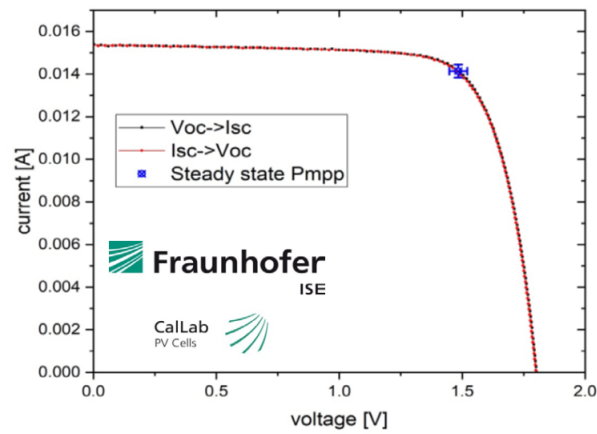
Results and Discussion

Before reporting the data collected regarding our bifacial tandem solar cells, we first show the performance of our best monofacial 2T perovskite/silicon devices. By doing this, we can highlight more clearly the difference between the two architectures and use it to display the efficiency gain of the new bifaciality concept compared to conventional tandem solar cell.

3.1 Monofacial 2T Tandem

This innovative solution deposition technique⁵⁰ allows us to fabricate 2T perovskite/silicon cells with a certified efficiency of 25.2% (fig. 3.1). In this case we used a 1.65eV bandgap perovskite since current matching is a major concern in monolithic tandems. By using a wider bandgap absorber, we blue shifted the absorption curve of the perovskite to avoid detrimental overlapping with the silicon absorption. As a consequence, it is no surprise that our champion device, with a 1.68eV bandgap, achieved 25.8% efficiency (fig. 3.2). This value is confirmed by the MPP tracking at 26.4% (fig. 3.3) and by an additional J-V measurement taken afterwards, which shows 25.95% efficiency. The slight difference between PCEs in the current density-voltage measurements is likely due to halide rearrangement inside the perovskite during MPP light exposure. Indeed, it is widely reported that exposure to light activates photo-induced cation or halide redistribution^{72,73} in the perovskite, which is very likely to happen during the power stabilization

tracking where the monofacial cell is shone with AM 1.5G 1-sun for 5min.



		Vorwärtsrichtung / forwards scan direction			Rückwärtsrichtung / reverse scan direction
V_{oc}	=	(1800.5 ± 12.1) mV	V_{oc}	=	(1802.6 ± 12.1) mV
I_{SC} (Ed.2 - 2008)	=	(15.35 ± 0.29) mA	I_{SC} (Ed.2 - 2008)	=	(15.36 ± 0.29) mA
I_{MPP}	=	14.16 mA	I_{MPP}	=	14.15 mA
V_{MPP}	=	1475.1 mV	V_{MPP}	=	1485.3 mV
P_{MPP}	=	20.89 mW	P_{MPP}	=	21.01 mW
FF	=	75.58 %	FF	=	75.91 %
η	=		η	=	
steady state MPP					
V_{oc}	=			=	
I_{SC} (Ed.2 - 2008)	=			=	
I_{MPP}	=	(14.14 ± 0.30) mA		=	
V_{MPP}	=	(1483.3 ± 36.2) mV		=	
P_{MPP}	=	(20.98 ± 0.57) mW		=	
FF	=			=	
η	=	(25.21 ± 0.75) %		=	

Figure 3.1: Certification performed by Fraunhofer ISE on our monofacial tandem that achieved $PCE = 25.2\%$.

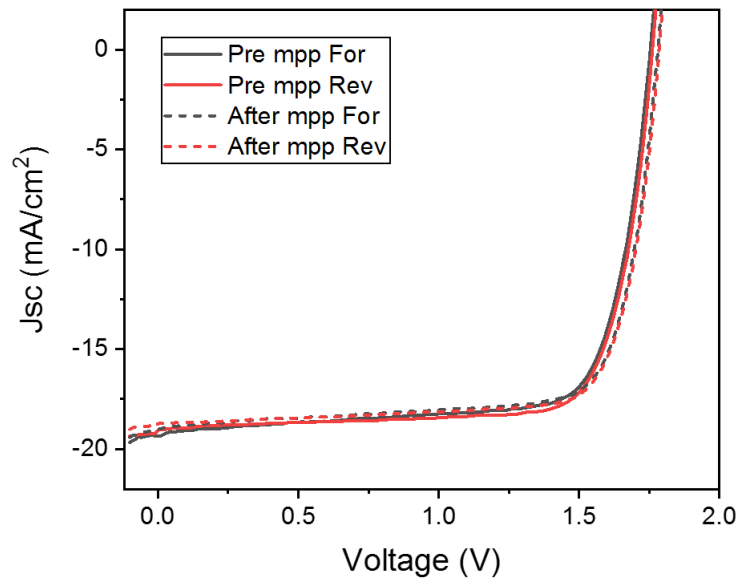


Figure 3.2: J-V curves of our champion monofacial tandem.

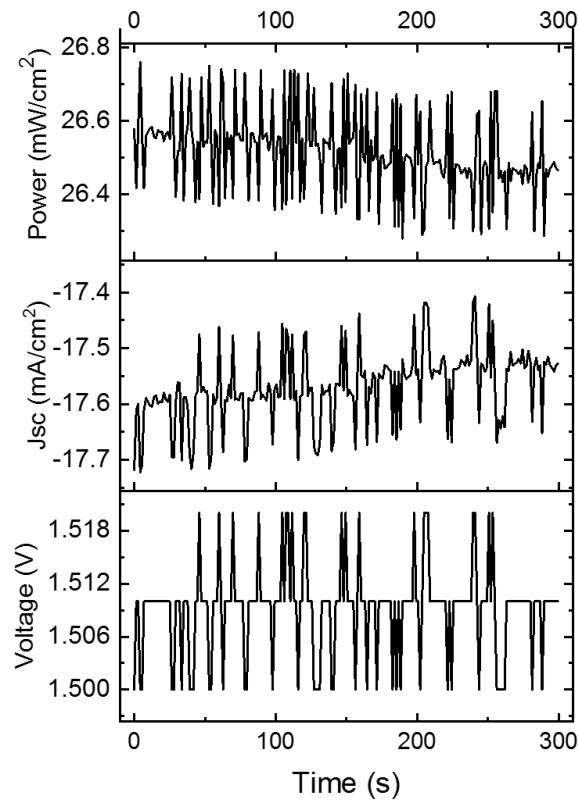


Figure 3.3: Stabilized power tracking of our champion monofacial tandem.

Our spincoating process allows us to reliably reproduce multiple devices with similar efficiencies, as seen from a statistics of 88 devices (fig. 3.4 and 3.5). To this we can add two stability tests performed on encapsulated cells. In the first experiment, we tracked the four figures of merit for 400 hours while keeping the tandems at 85°C in the dark with $\approx 40\%$ humidity, and found that devices retained their original performance (fig. 3.6). In the second test, we tracked the effect of 400 hours of continuous illumination under MPP condition, with a J-V curve every 10 min to determine the performances. Again, we found that the tandems lose negligible amount of efficiency (fig. 3.7). Complementary, these two experiments testify, over a remarkable extent, the stability of our tandems.

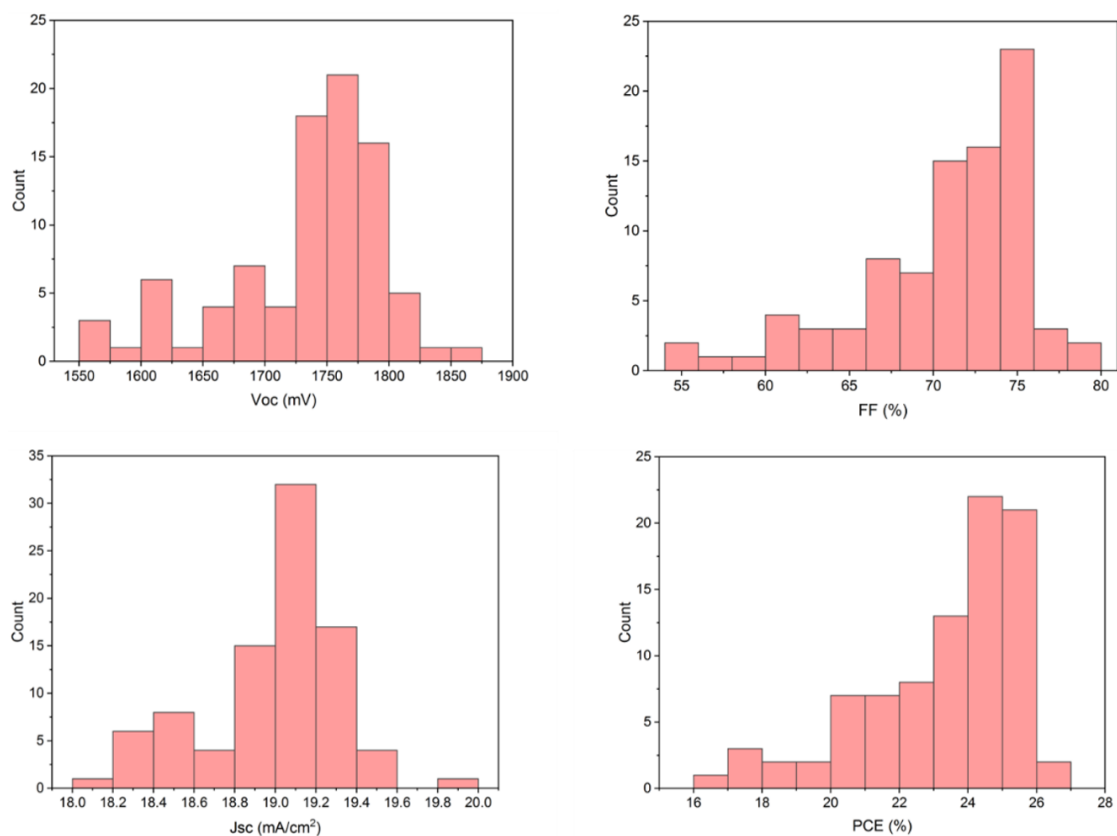


Figure 3.4: Histogram plots of the four figures of merit of 88 monofacial tandems.

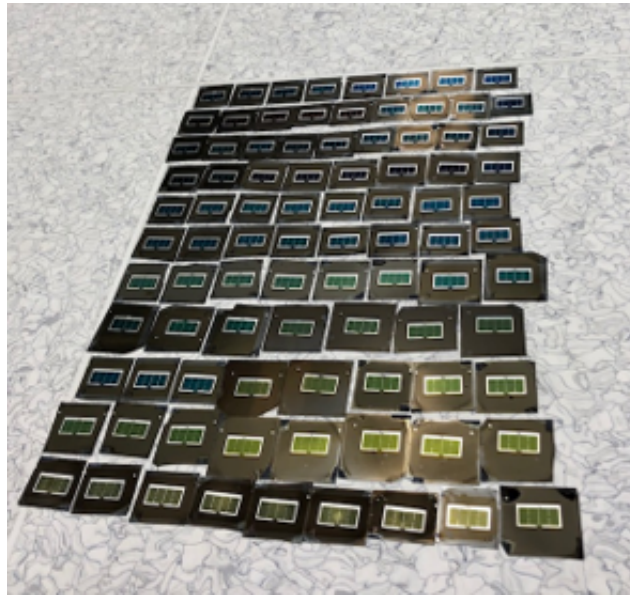


Figure 3.5: Photo of the 88 monofacial tandem used for statistics.

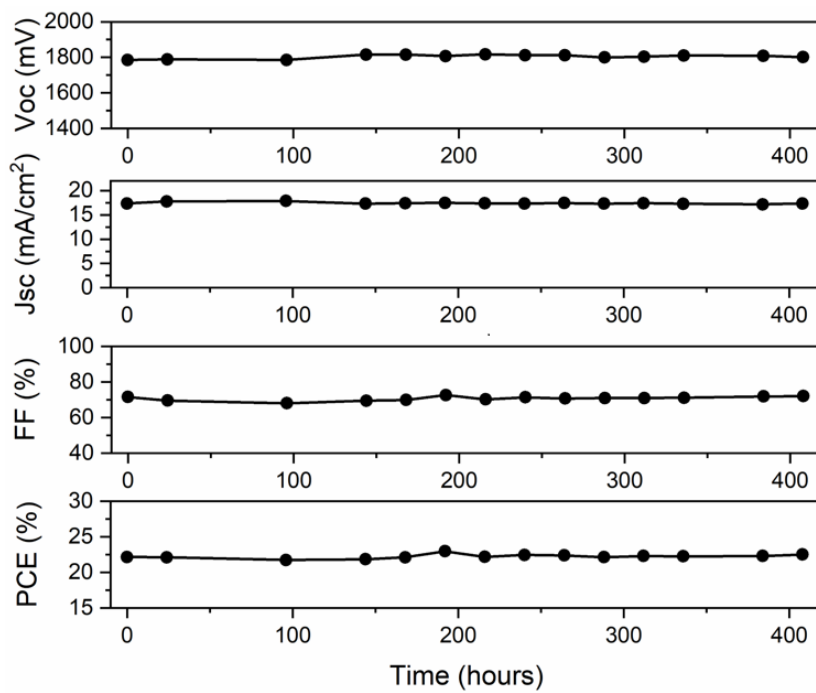


Figure 3.6: Performance of the monofacial tandem during the 85°C stability test.

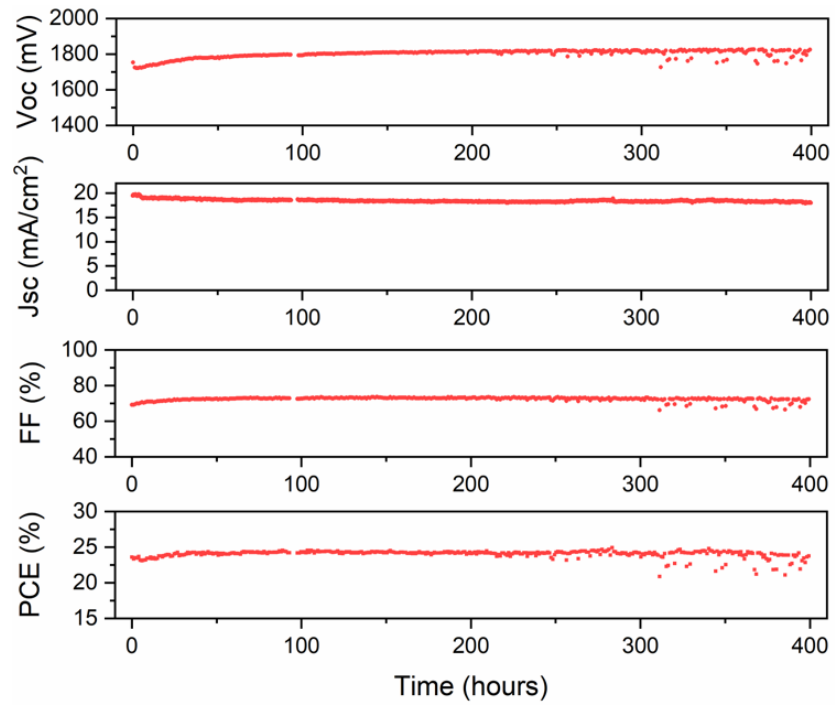


Figure 3.7: Performance of the monofacial tandem under constant illumination.

3.2 Bifacial 2T Tandem

As we have previously explained, a bifacial tandem includes a semitransparent rear contact that allows light absorption from the silicon bottom cell. This extra gathered light is known as albedo and is the sum of three components: 1) direct sunlight reflected from the grounds, 2) scattered sunlight, 3) scattered sunlight reflected from the ground (fig. 1.25). To study the effect of albedo on device efficiency, we fabricated 2T bifacial perovskite/silicon tandem solar cells with different perovskite bandgaps. Similar to the monofacial case, our bifacial tandem employs micrometer thick perovskite on top of fully textured silicon heterojunction cells, in *p-i-n* configuration. Figure 3.8 recaps said structure. Differently from the monofacial tandems, which have the back side fully covered by sputtered Ag, our bifacial's backside resembles the front electrode (fig. 2.3).

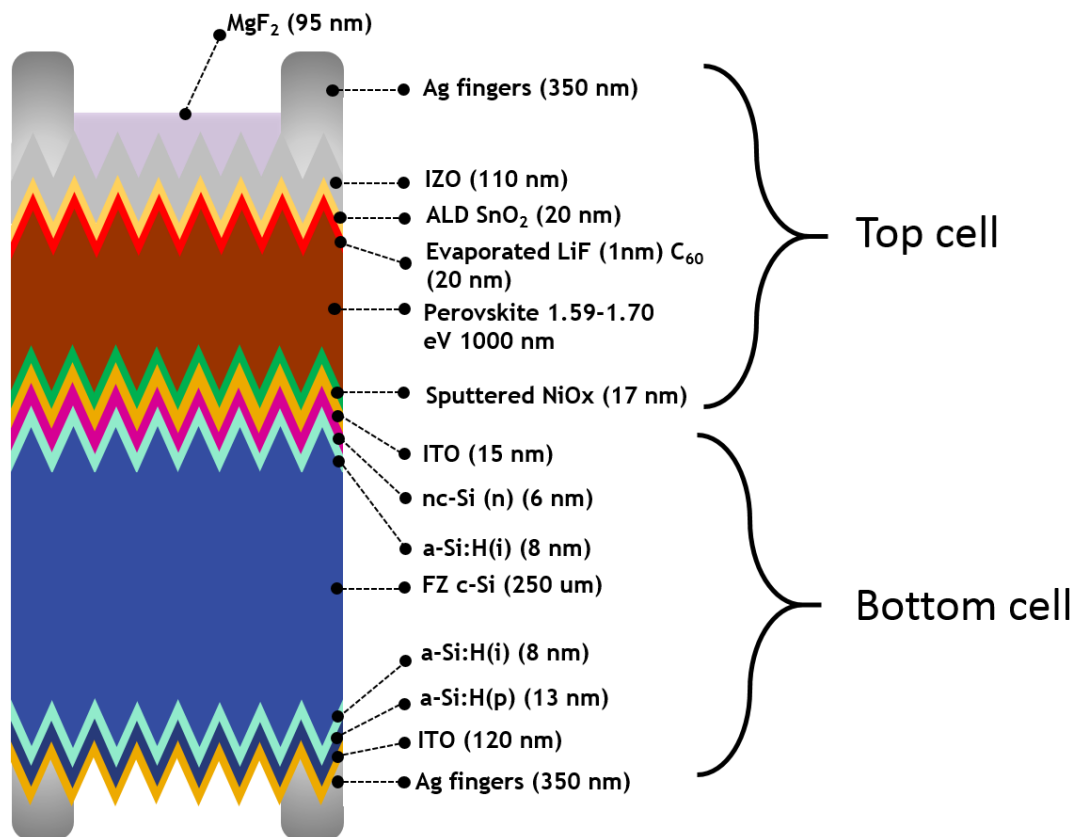


Figure 3.8: Overview of the complete bifacial tandem structure.

In the monolithic tandem, the top and bottom cell are connected in series by the recombination junction, and as per textbook, the total current of the device is limited by the lower of the two sub-cells. Therefore, the ability to generate equivalent current (current matching condition) in both sub-cells under specific irradiation, determines the maximum current generated by the tandem. Optimum current-matching can be achieved via tuning the perovskite bandgap, i.e. by changing the iodide-bromide ratio. In comparison to monofacial mode, we predict higher absolute values of saturation current for tandems operating in bifacial mode, since the albedo can provide extra photons to the silicon bottom cell. The saturation condition indicates that current matching is reached for that specific perovskite bandgap. This is in agreement with previous gathered data for conventional tandems, where we see that it is always the silicon that limits the J_{sc} of the overall device. Figure 3.9 shows J_{sc} of the bifacial tandem, perovskite sub-cell, and silicon sub-cell as a function of the rear illumination (defined as “effective albedo”) for five different perovskite bandgaps. For the theoretically optimized current matching condition of perovskite/silicon monofacial tandems illuminated with AM 1.5G spectrum light, at $1.7eV$ bandgap, we see that the effective-albedo does not improve the J_{sc} of the device. On the other hand, reducing the top-cell perovskite bandgap allows the presence of effective-albedo to improve the J_{sc} of the tandem stack progressively: the lower the bandgap, the higher J_{sc} saturation values we can achieve. In a similar fashion, the overall predicted power output of the bifacial tandem also benefits from the same effect. For bandgaps smaller than $1.7eV$, we show a maximum power output of $49mW/cm^2$ for a $1.59eV$ perovskite with only $15mW/cm^2$ of effective albedo (fig. 3.10).

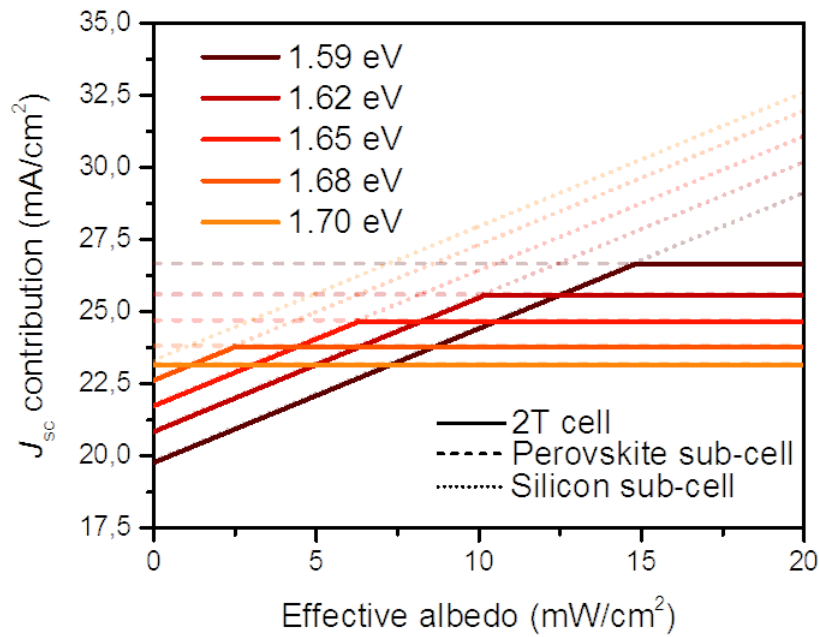


Figure 3.9: Theoretical J_{sc} values for bifacial solar cells with 5 different perovskite bandgaps.

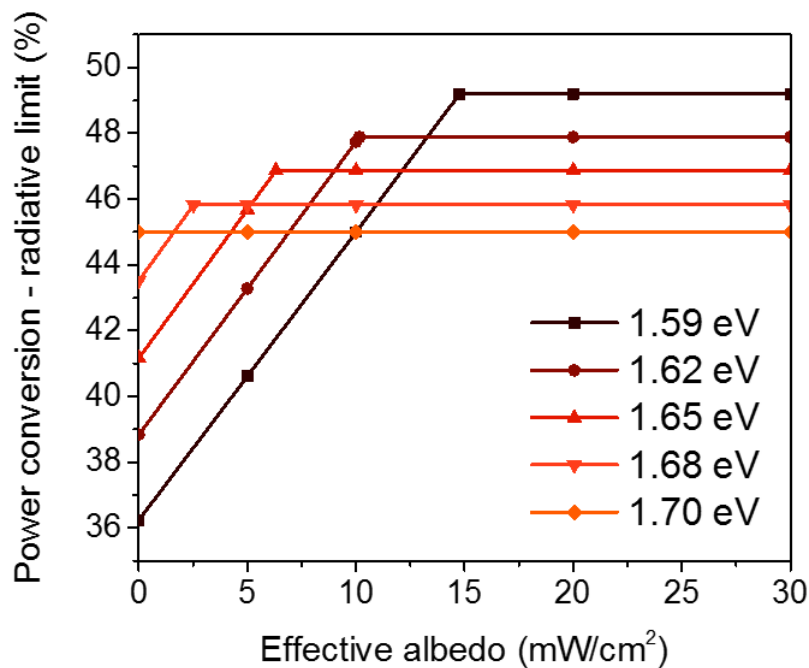


Figure 3.10: Overall predicted power output for bifacial tandems with 5 different perovskite bandgaps.

To confirm the theoretical models, we fabricated bifacial solar cells with five different perovskite bandgaps (1.59, 1.62, 1.65, 1.68, 1.7eV) by altering the iodide to bromide ratio. Photoluminescence measurements were used to empirically determine the bandgap of the solutions prepared (fig. 3.11).

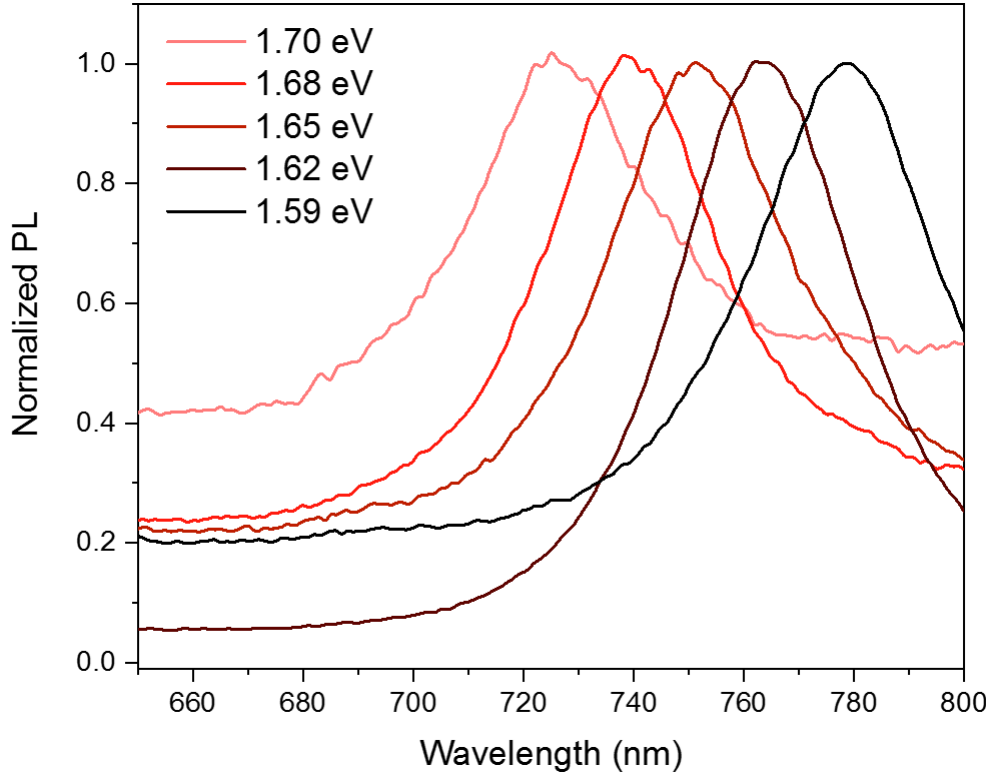


Figure 3.11: Photoluminescence measurements taken in order to check the bandgap of our perovskite solutions.

In the following graphs, we show the statistical distribution of the figures of merit for bifacial tandems with different perovskite compositions, measured under 1 sun AM 1.5G in monofacial mode. This initial measurement is done to check the outcome of the device after the whole fabrication process. Nevertheless, even from these first measurement, we can already identify some interesting trends. For starters, we see that the V_{oc} (fig. 3.12) increases as the bandgap is widened, reaching 1.8V for the largest case. The J_{sc} (fig. 3.13) shows a bell trend, with a maximum at 1.68eV, in which we identify the optimal current matching condition. For smaller bandgaps, the perovskite's absorption is larger than the silicon's, thus

producing more current. However, since we are connected in series, the overall J_{sc} is limited by the smaller of the two sub-cell generated currents, i.e. we are in silicon-limited condition. For bandgaps above 1.68eV , the perovskite sub-cell is now producing less current than its silicon counterpart and we are now in the opposite condition: the perovskite is now limiting the tandem's J_{sc} (perovskite limited condition). Interestingly, the FF (fig. 3.14) is slightly higher in silicon-limited condition compared to perovskite-limited condition. Finally, we see that the power conversion efficiency (PCE) (fig. 3.15) is close to 25% for those bifacials with perovskite bandgaps of 1.65 , 1.68 and 1.7eV ., confirming the results obtained with the monofacial tandems.

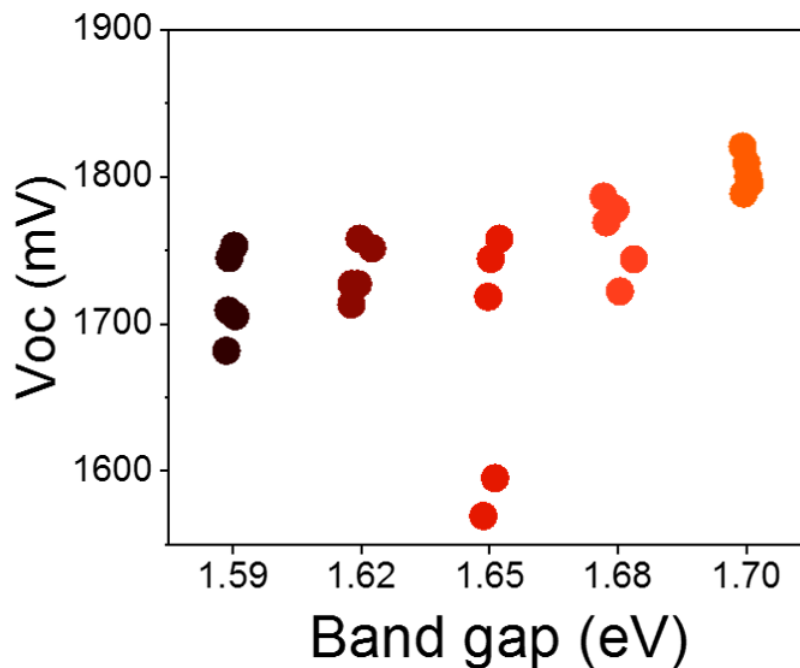


Figure 3.12: V_{oc} values of our bifacials measured in monofacial mode. By opening the bandgap, the open circuit voltage increases.

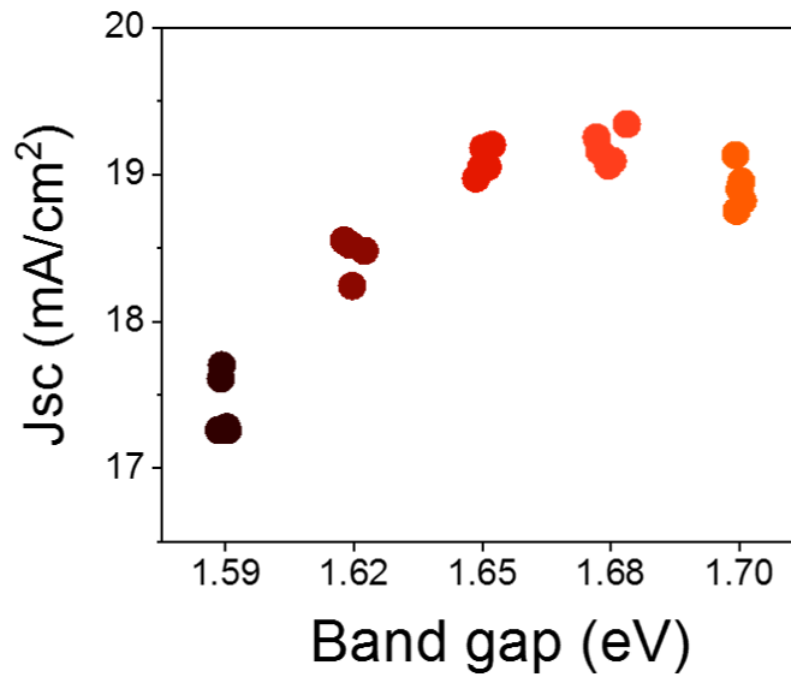


Figure 3.13: Short circuit density current of our bifacial solar cells measured in monofacial mode. J_{sc} values reach the maximum at 1.68eV, which highlights the current matching condition between top and bottom cell.

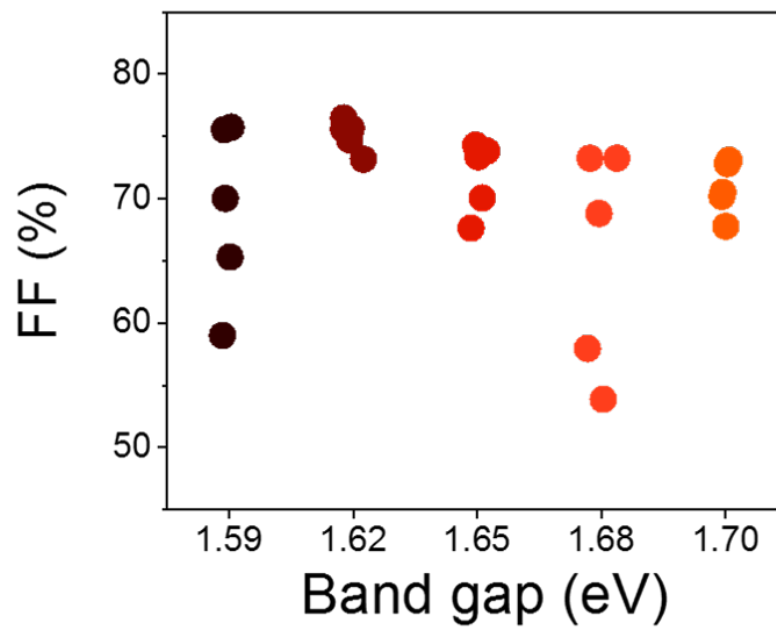


Figure 3.14: Fill Factor data of the bifacial devices, measured in monofacial mode.

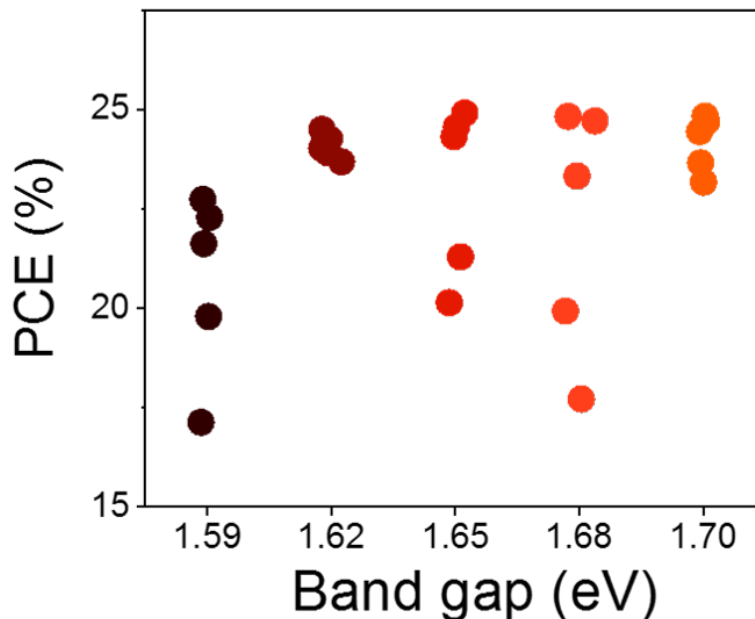


Figure 3.15: PCE of our bifacial solar cells measured only with light shining on the front side. The highest efficiencies are obtained with the wider bandgap perovskites.

After confirming the positive outcome of the bifacial fabrication, we now move to investigating the role of effective-albedo on our solar cells. The bifacials are here measured in a custom setup involving two solar simulators facing each other. The Abet simulator is fixed at 1 sun ($100\text{mW}/\text{cm}^2$) intensity and we use it to shine the perovskite top cell. The silicon bottom cell is irradiated by the Oriel simulator, with intensity ranging from 0 to $90\text{mW}/\text{cm}^2$ (or 0.9 sun equivalent). We use this second light source to recreate the variable albedo. The bifacial solar cell is placed on a board located in the middle between the Abet/Oriel system as seen in figure 2.6. As mentioned in chapter 2, before measuring with the bifacial setup, we encapsulate the solar cells in order to facilitate contact layout and limit device degradation in open-air. In figure 3.16 we compare J-V curves of bifacial tandem, before (yellow) and after encapsulation (brown) for a 1.62eV bandgap perovskite. This process comes at the cost of a significant reduction in current density, attributed to the front glass reflection and mismatch in refractive index at the glass-vacuum-top electrode interfaces. Figure 3.16 also shows that the 1.62eV bifacial, when measured in monofacial mode, has a lower current compared to

the 1.68eV with standard metal rear electrode (blue), which is to be expected if we look back the different J_{sc} shown in figure 3.13. However, in the presence of $20\text{mW}/\text{cm}^2$ effective-albedo (orange), the current density is enhanced above the monofacial limit. Indeed, the effective-albedo provides extra photons to overcome the silicon-limited condition of the bottom cell and match the current generation of the 1.62eV perovskite, improving the overall efficiency of the solar cell. This power boost demonstrates the promising potential of bifacial tandem devices, as the current-matching condition with excess effective-albedo surpasses the optimized current density of a monofacial tandem.

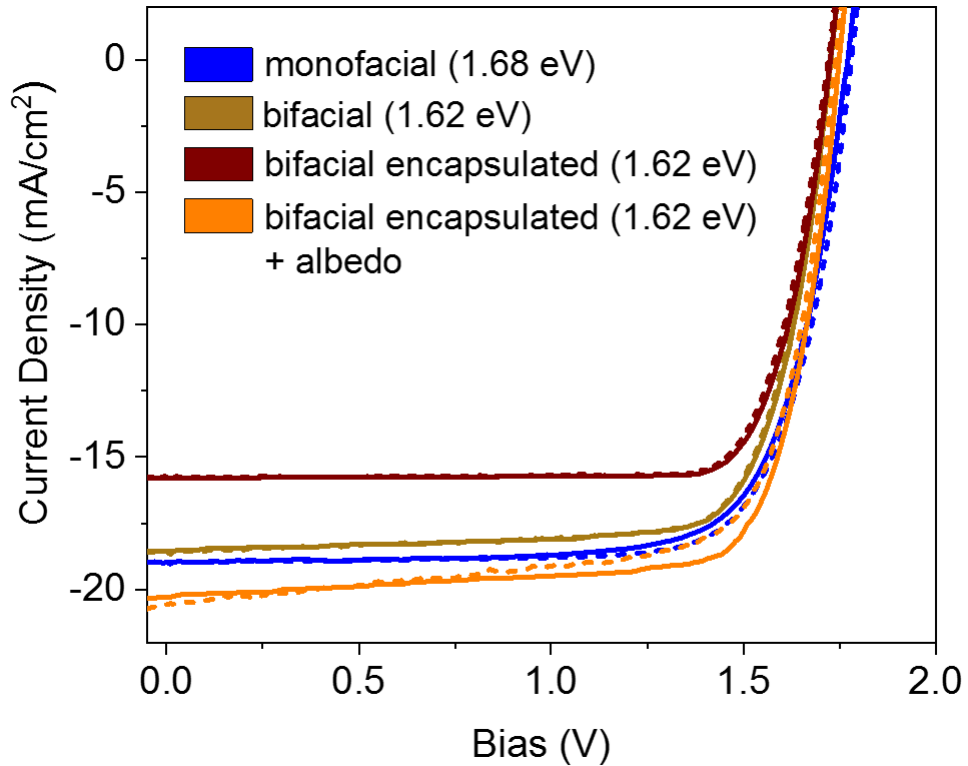


Figure 3.16: J-V comparison between devices pre-encapsulated and encapsulated. The thick glass and vacuum in front of the perovskite, lower the J_{sc} of the bifacial. However, with the extra albedo from the back, the device can overtake J_{sc} values of a wide bandgap monofacial tandem.

In the following figures, we report the device performance as a function of effective albedo, ranging from 0 to $\approx 95\text{mW}/\text{cm}^2$, of the same bifacial tandems with different perovskite bandgaps, now encapsulated. We can see that the V_{oc} (fig.

3.17) slightly increases with effective-albedo, in agreement with a higher concentration of photo-generated electrons. However, it's the J_{sc} (fig. 3.18) parameter which benefits the most from the presence of additional light. In absence of any back light, the current density mimics the same trend seen in figure 3.13, where the only variation is due to the perovskite bandgap. As we increase the power of the Oriel solar simulator, the J_{sc} rises rapidly, saturating at $\approx 20\text{mA}/\text{cm}^2$ for most bandgaps tested. This enhancement is most pronounced in narrower bandgap perovskites (1.59 and 1.62eV), as the current matched J_{sc} level is increased due to the red-shifted perovskite absorption and the increased silicon absorption through effective-albedo. Whereas the wide bandgap 1.7eV shows little to no J_{sc} gain. Both experimental and calculated values show that with decreasing bandgaps, the effective-albedo required to reach current-matching, is pushed to higher albedo intensities. However, the FF (fig. 3.19) drops dramatically in the $0 - 20\text{mW}/\text{cm}^2$ rear light range, only to partially recover at irradiation higher than $\approx 20\text{mW}/\text{cm}^2$. This effect is again more pronounced for lower bandgap perovskites.

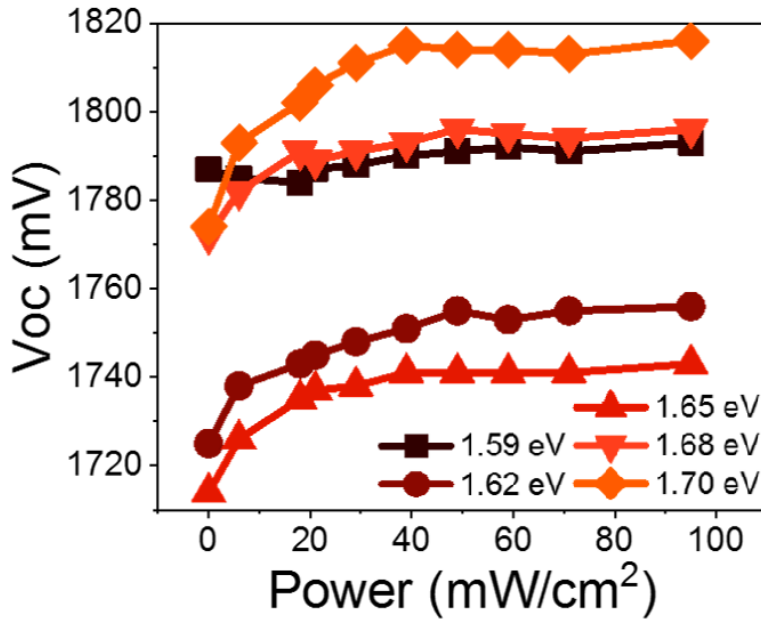


Figure 3.17: V_{oc} of our bifacial devices as function of increasing rear albedo.

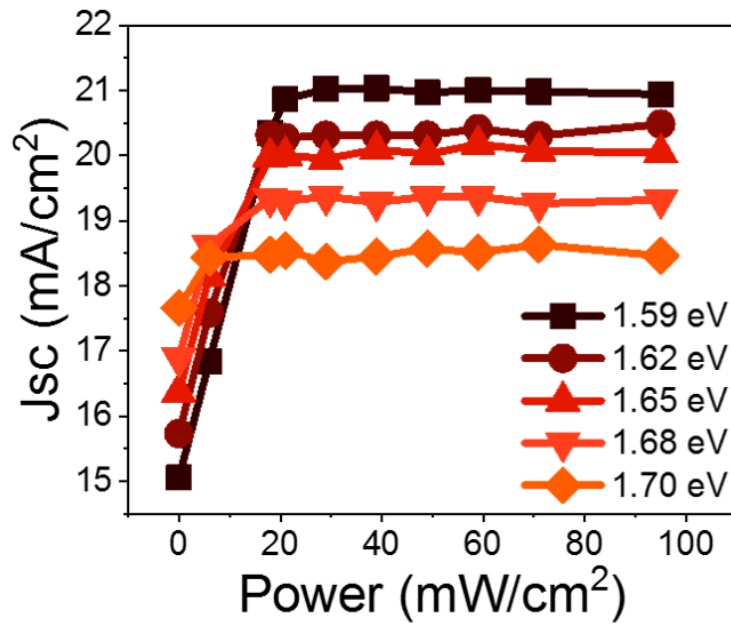


Figure 3.18: Short circuit density current of bifacials as function of increasing back light. J_{sc} values reach a saturation level, which is higher for lower bandgap perovskites.

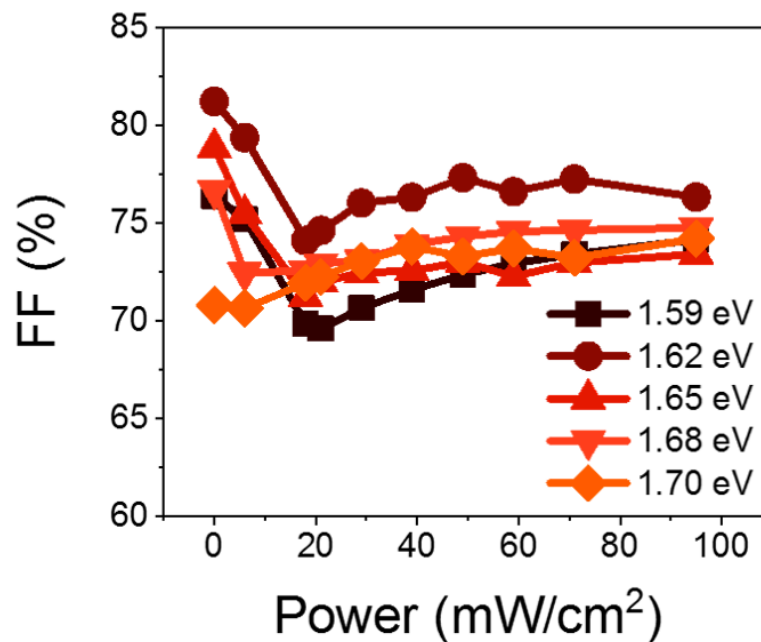


Figure 3.19: Fill Factor as function of increasing rear illumination. The FF drop around $20\text{mW}/\text{cm}^2$ is due to current mismatch between top and bottom cell.

The power conversion efficiency calculations of our bifacial tandems significantly differ from the monofacial counterparts, as the additional light source is used to recreate the effective-albedo. Therefore, we report the absolute power generation of the device as a function of the effective-albedo. Similar to the J_{sc} trend, the device's power generation (fig. 3.20) strongly benefits from the extra photons on the bottom cell, achieving values as high as $\approx 28mW/cm^2$ for 1.59 and 1.62eV perovskites.

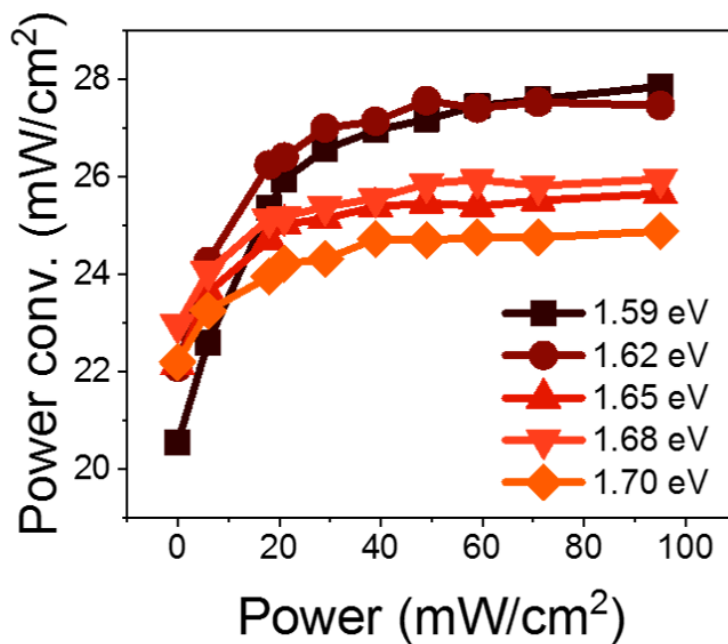


Figure 3.20: Overall power output of our bifacials. The lower the bandgap, the higher efficiencies obtained. The maximum reached is $\approx 28mW/cm^2$ with a 1.59eV perovskite bandgap.

More importantly, our calculations show that an effective-albedo of just $30\text{mW}/\text{cm}^2$ can improve the absolute power generation of the bifacial tandem with low bandgap by more than 25%, compared to the monofacial configuration (fig. 3.21). Such albedo intensity is a realistic condition in solar fields where sand or concrete cover the ground surface. To validate our findings and to again confirm the reproducibility of our solution processed device fabrication, we report the statistics for 29 bifacials with 1.62eV perovskite bandgap (fig. 3.22). Here we analyse the power generation enhancement when we have $30\text{mW}/\text{cm}^2$ effective-albedo on the rear side, and find out that the device power distribution is centred on $25.5\text{mW}/\text{cm}^2$. Instead, without albedo, the same distribution is shifted to lower values around $21.5\text{mW}/\text{cm}^2$. The graph herein shows that operating the tandem device in bifacial mode offers an average absolute increment of 19% in power generation.

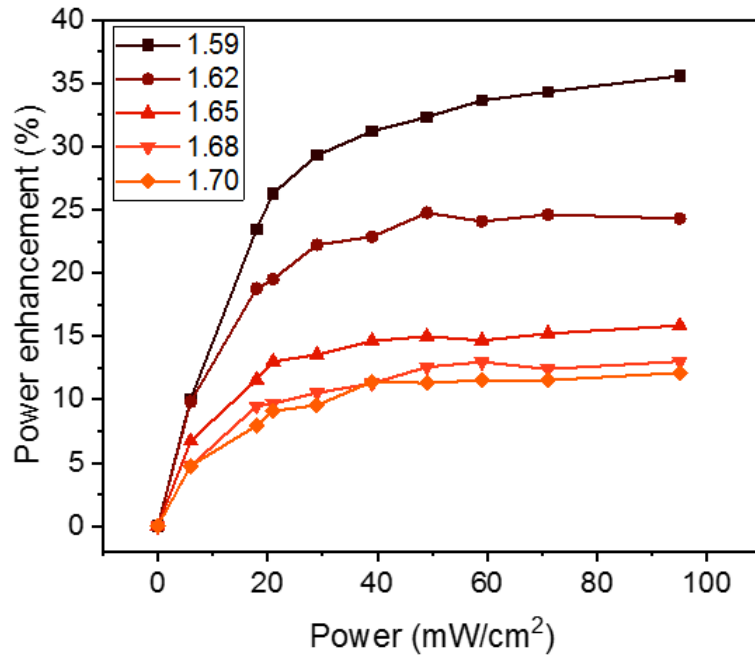


Figure 3.21: Overall power output gain for bifacial tandems with albedo effect, compared to monofacial mode.

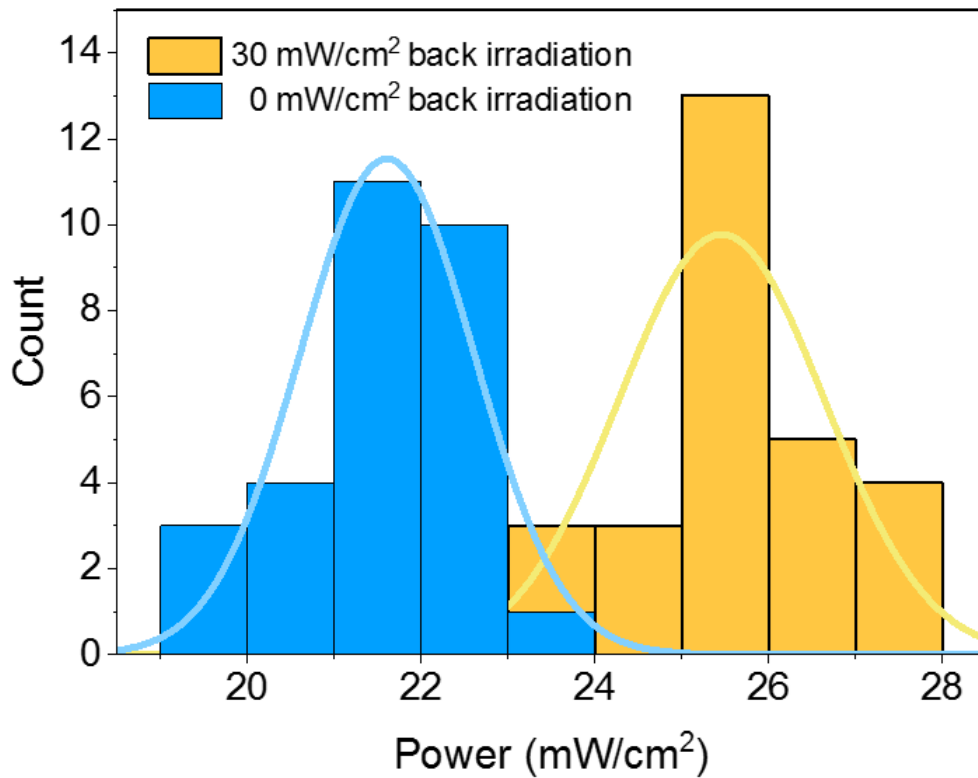


Figure 3.22: Distribution of the power output of 29 bifacial solar cells at $1.62eV$ taken at 0 albedo and at $30mW/cm^2$ of back light intensity.

As a by-product of the additional effective-albedo shining onto our devices, the operating temperature of the bifacial tandem increases. In figure 3.23 we monitor the temperature variation under different rear side irradiation conditions alongside their respective cooling times. As expected, shining the devices with more light, rapidly increases the temperature to over $60^{\circ}C$. Based on the cooling time results, we established a minimum time interval between the sequential measurements carried out for figures 3.17, 3.18, 3.19, and 3.20 in order to ensure standard test conditions. However, the operational temperature of a solar cell in an outdoor environment (especially in a sunny and hot climate like the one in KAUST) can easily reach the $50 - 60^{\circ}C$ range, even for perovskite/silicon tandems where thermalization losses are significantly reduced compared to the single junction counterparts.

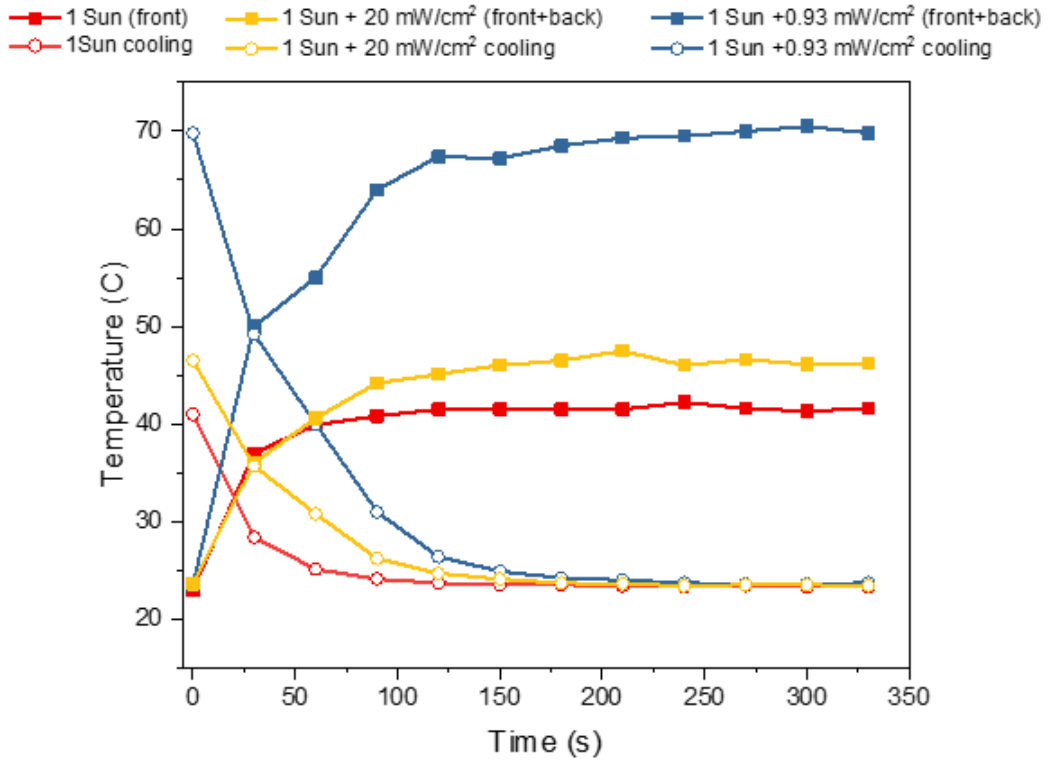


Figure 3.23: Plot of temperature variation. The solar cell heats up more rapidly when more rear side albedo is present, and also takes more time to cool down.

Related to this problem, it is important to probe the operational stability of the device performance for our glass/glass encapsulated bifacial tandems. We stored a solar cell in the dark at 85°C for 1000 hours and recorded the J-V curves, in monofacial mode, on a daily basis (fig. 3.24). Interestingly, we observed an increase in V_{oc} over time and a small reduction in the FF. We speculate that the degradation of the contacts is the cause for such variations. Nonetheless, since the current remained constant over the whole investigation, the overall PCE remained stable. Figure 3.25 illustrates photovoltaic parameters measured for 500 hours under constant irradiation to assess operational stability under constant irradiation. Maximum power point tracking is employed between J-V sweeps. Similar to the stress study, a gain in V_{oc} is observed within the first hundred hours. The primary degradation factor is a gradual decrease of the FF, attributed to ion migration and accumulation⁷⁴ within the perovskite absorber layer, progressively impeding

charge transport over the duration of the stability experiment. Fortunately, this effect is reversible in the dark, leading to an FF jump from 62% to 75% after 24 hours with no irradiation as reported elsewhere^{75,76,77,78}. Taking in consideration this dark-recovery, a PCE drop of 12% is observed after 500 hours of constant irradiation. J-V curves (fig. 3.26) were taken as explained in depth in chapter 2, section 6.

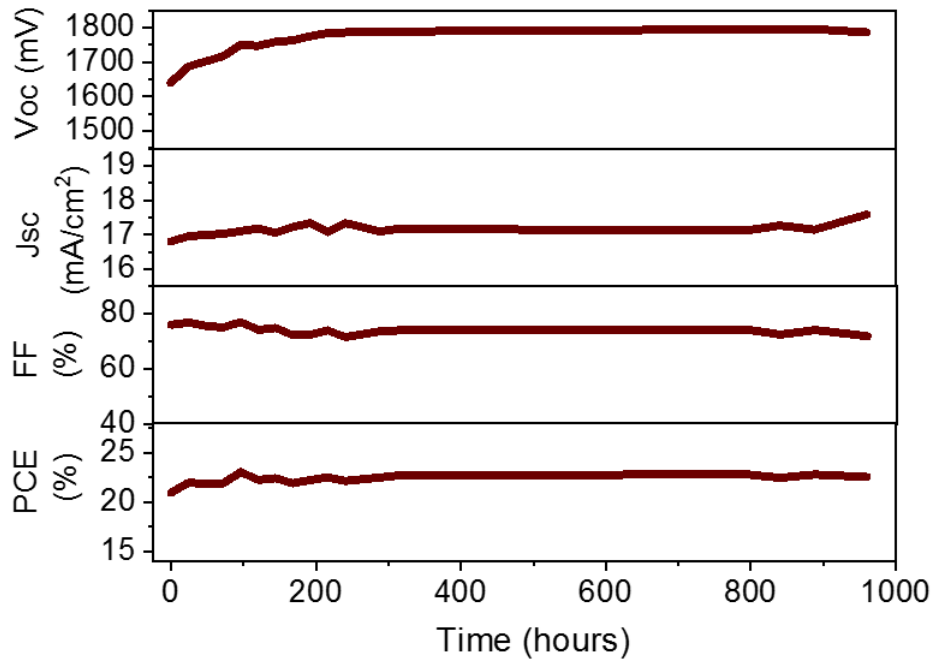


Figure 3.24: Progress over 1000 hours, of the four figures of merit, of our bifacial tandem at 85°C in dark.

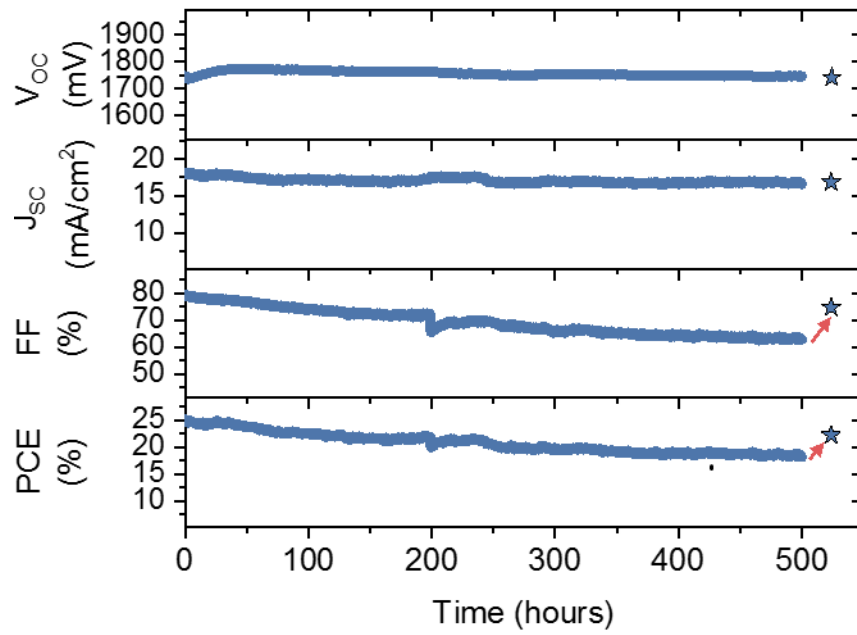


Figure 3.25: Constant irradiation tracking of our bifacial tandem. The star represents the measurement taken after 24 hours of dark, highlighting the device's recovery.

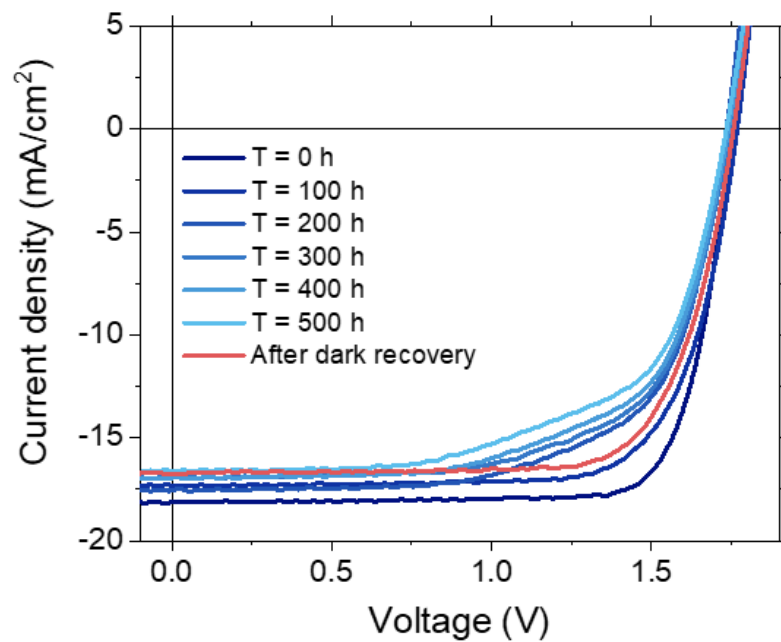


Figure 3.26: Evolution of the J-V curve during operational stability test under constant irradiation.

To better understand the current matching between the perovskite and silicon sub-cells, we collected the EQEs of non-encapsulated bifacial tandems with 1.59, 1.62, 1.65, 1.68, 1.7 eV perovskite bandgaps (fig. 3.27) measured in monofacial mode. As expected, the widening of the perovskite bandgap reduces the current contribution from the top cell, because the band edge is more blue shifted. This way, the perovskite filters out less incoming radiation, and more light reaches the silicon bottom cell. Vice versa, a 1.59 eV top cell bandgap, has a red shifted band edge and overlaps more with the silicon's response, therefore limiting the amount of light that reaches the bottom of the tandem. From the integrated EQE, we identify the current matching condition (for the monofacial tandem case) to happen at 1.68 eV as evidenced by the trend in J_{sc} of figure 3.13. The overall reflection of the bifacial tandem does not vary from bandgap to bandgap (fig. 3.28).

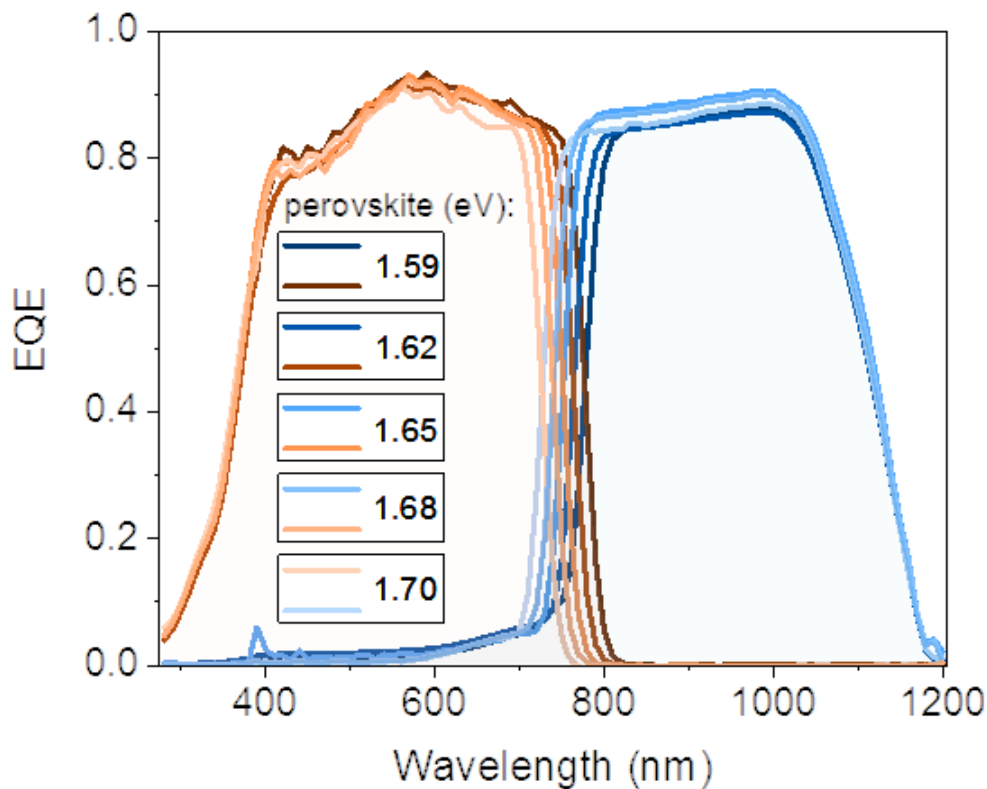


Figure 3.27: EQE curves of the 5 different perovskite bandgaps. When the perovskite response decreases, the silicon's curve increases, and vice versa.

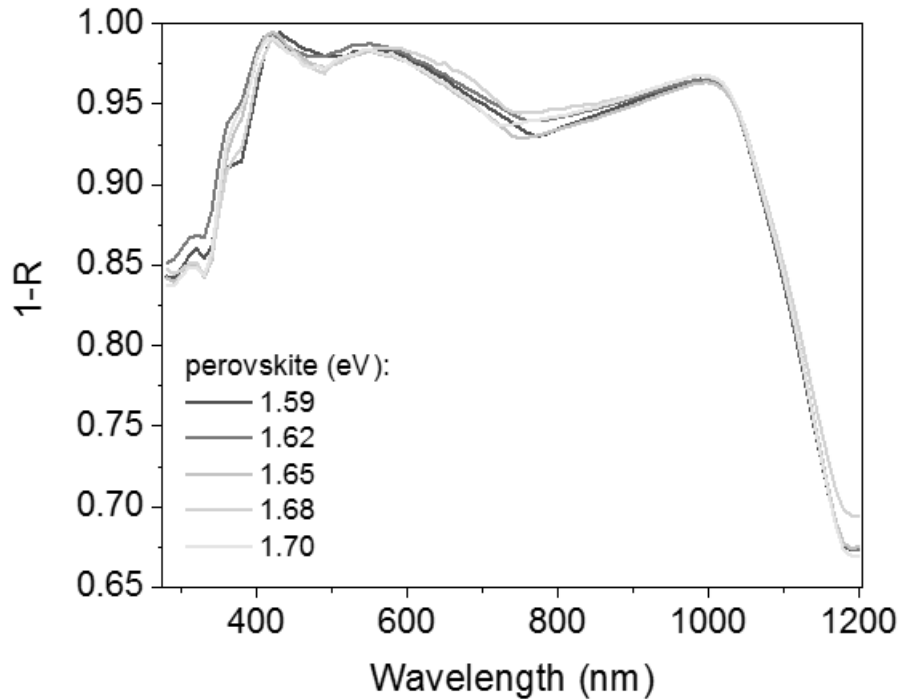


Figure 3.28: 1-Reflection measurement taken for each perovskite bandgap.

To better visualize the influence of the perovskite bandgap on the bifacial current, figure 3.29 plots the EQE's integrated currents (full circles) of both perovskites (red) and silicon (blue), for the different bandgaps. We compare these values with the J_{sc} s obtained from the figure 3.18 (hollow circles) in the saturation regime (red) and without effective-albedo (blue). The integrated EQE data suggest that current matching is achieved for a perovskite bandgap slightly smaller than $1.7eV$. While this represents the optimum condition for monofacial tandems, as we tested, in the bifacial configuration, a $1.7eV$ top cell bandgap offers no gain in current, since the device becomes perovskite-limited under effective-albedo. On the other side of the graph, the integrated EQE shows a remarkable mismatch in current for the $1.59eV$ perovskite, since the silicon component is heavily limiting the final device current. Obviously, this would be a poor choice for a monofacially configured device. However, the narrow bandgap enables the highest current gain in the bifacial configuration, provided sufficient rear side illumination is present. As a result, the perovskite bandgap plays a fundamental role in capitalizing on realistic albedo and achieving significant current gains for bifacial tandem setups.

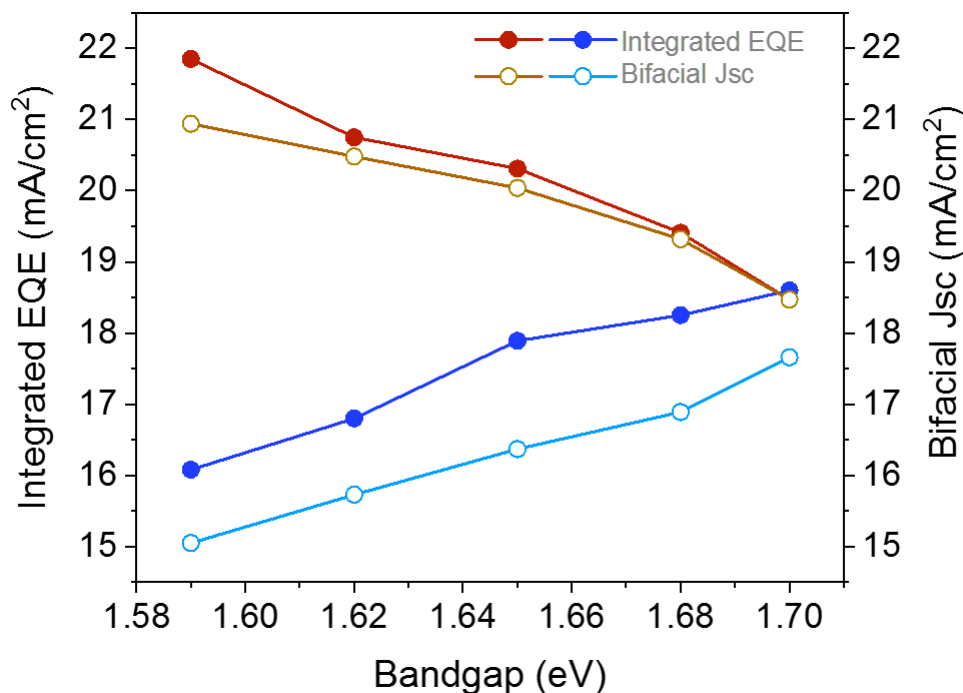


Figure 3.29: Graph highlighting current match and mismatch of the different bandgaps. Full circles are points taken from the integrated EQE curves, while hollow circles are data taken from the J-V measurements done with the Abet/Oriel setup. J_{sc} difference between full and hollow circles is attributed to encapsulation.

To validate the potential of our technology, we compared the operational properties of monofacial and bifacial tandems under three different albedo conditions: concrete, synthetic grass, and artificial snow. For this experiment, we installed the monofacial and bifacial tandems on our portable test field kit, changing the ground material to generate the different coloured albedos. For each condition, we recorded a J-V curve every 10 min, for 1 hour. To be consistent, we carried out the experiment at the Zenith, with the support of a pyranometer and a calibrated silicon solar cell to monitor the light intensity. Figure 3.30 shows the power conversions and the J_{sc} of the bifacial (black) and monofacial (red) tandems. We clearly can see that the bifacial tandem outperforms the monofacial tandem for each albedo condition, with remarkable gains for the concrete case. We speculate that this result is due to the larger ground coverage of actual concrete behind the test field set up. We correlate the increment in the power conversion to the higher

generated current in bifacial configuration. Overall, the average increment is 20% for concrete, 6% for artificial snow, and 4.3% for synthetic.

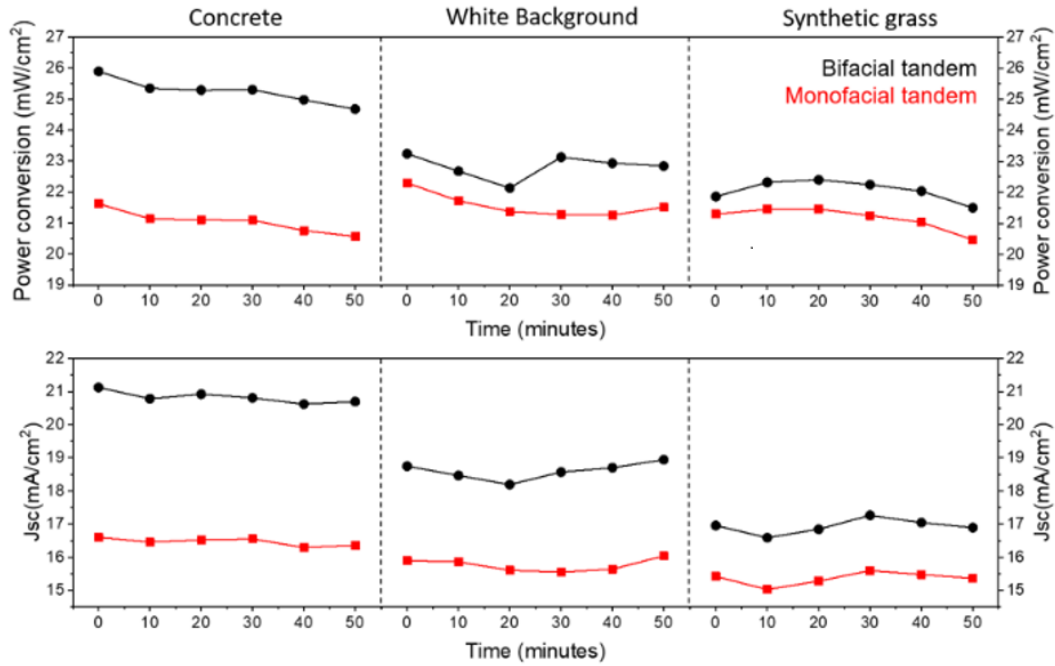


Figure 3.30: Effect of different albedo types on our bifacial tandems and comparison with monofacial solar cells.

Furthermore, we extended the comparison between monofacial and bifacial tandems to three test-field locations: Jeddah – Saudi Arabia, for hot and sunny environment; Toronto – Canada, for cold environment; Karlsruhe – Germany, for continental environment. Figures 3.31, 3.32, and 3.33 show the power conversion of the devices from dawn to (06.00 am) to dusk (06.00 pm), measured every 10 min, over a 5 day investigation. To compare the results, we normalized the power conversion to sun equivalents, via the pyranometer and a calibrated silicon reference cell. For the experiment, the tandems were placed in a test field structure, with similar orientation (South) and distance from the ground, which is composed by sand and concrete (Jeddah), concrete (Karlsruhe), and snow (Toronto). To better represent the symbolic environmental conditions, the tandems were installed in specific times of the year: September for Jeddah, January for Toronto, and February for Karlsruhe. In Jeddah, the bifacial tandem performed better than the

monofacial. In particular, during midday when the light intensity is close to being 1-sun and the albedo influence is higher.

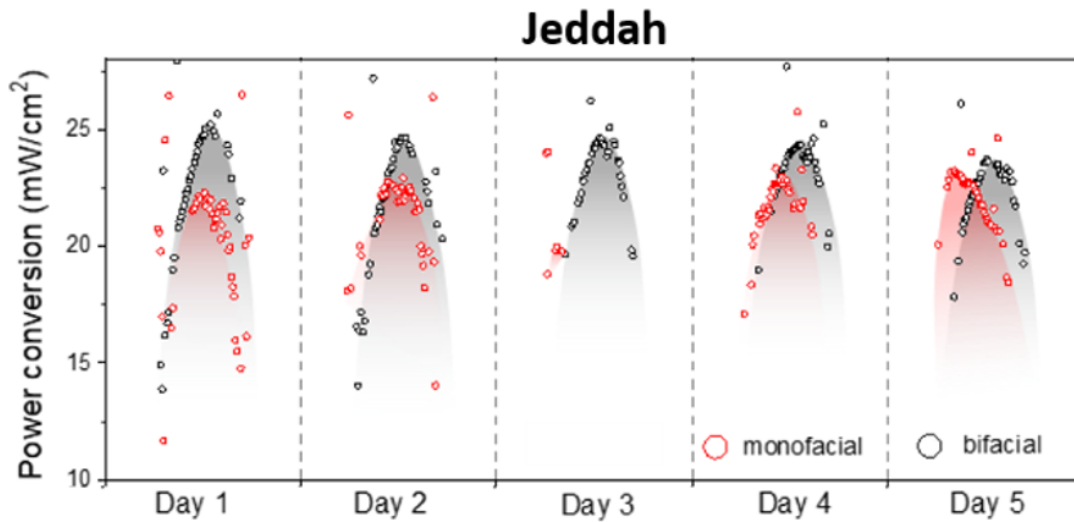


Figure 3.31: Outdoor field data for the location of Jeddah, Saudi Arabia.

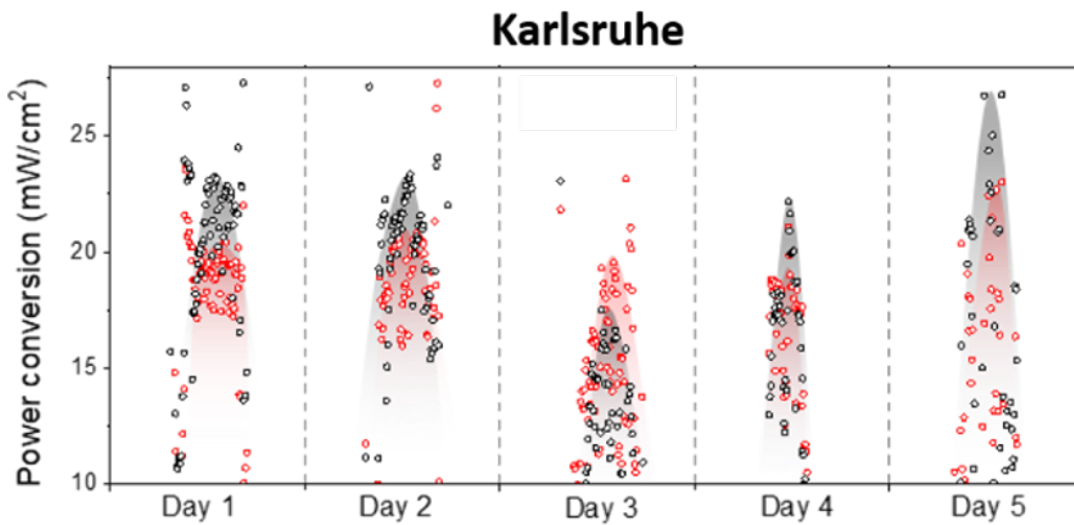


Figure 3.32: Outdoor field data for the location of Karlsruhe, Germany. Monofacial data is displayed in red, while bifacial data is portrayed in black. Power output enhancement for bifacial tandems is more pronounced when the weather is sunny (days 1, 2 and 5), compared to cloudy and rainy days (days 3 and 4).

In Toronto unfortunately, the adverse weather conditions strongly impeded the

success of the experiment. Interestingly enough though, in the only day that we were able to measure, the weather was cloudy and the sun's irradiance was mostly diffused, with constant power between $10 - 20 \text{ mW/cm}^2$, during the light hours. In these conditions, we expected lower current and lower performances for the bifacial tandem, due to the diffused nature of light. However, the bifacial and monofacial solar cell, showed similar power outputs, testifying the fundamental role of the albedo generated from the snow-covered ground.

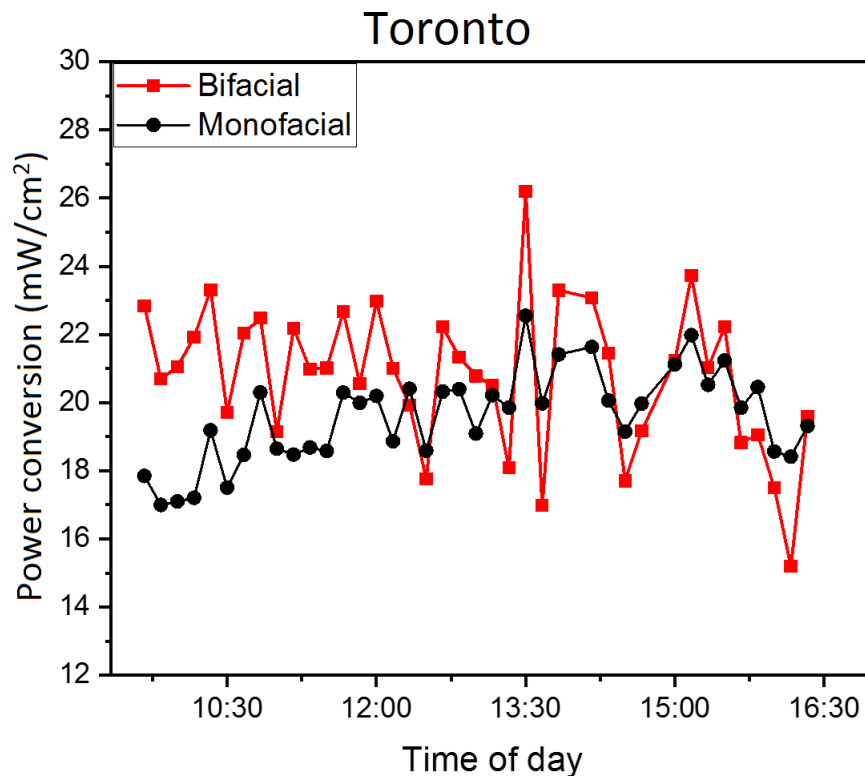


Figure 3.33: Outdoor field data for the location of Toronto, Canada, in the only day we were able to measure the solar cells.

Chapter 4

Conclusions

In this work, we have undisclosed the potential of bifacial perovskite/silicon monolithic tandems to overcome the limits of conventional light-to-electricity conversion: above the Shockley-Queisser limit, and above the limits imposed by current matching condition - typical of monolithic perovskite/silicon monofacial tandems. The key-enabler of this technology is the semitransparent back electrode, thus distinguishing bifacials from a conventional monofacial tandem (which has a full covered rear side). This extra window allows the backside of the device to collect reflected and scattered photons from the surrounding area. Because of this extra light, the current matching limit is bypassed and the overall efficiency of the device is increased. In this way, we proved that a bifacial tandem outperforms a monofacial tandem in terms of power conversion efficiency.

In details, we presented the fabrication of solution processed perovskite/silicon bifacial tandem solar cells on textured silicon. The solar cell is fabricated monolithically, meaning that the device works with only two electrodes and it consists of interconnected layers stacked on top of each other. This configuration allows for efficient light harvesting since the silicon absorbs in the red end of the spectrum, while the perovskite responds to the blue end. In chapter 2, we thoroughly described the steps to fabricate our bifacial solar cells. Starting from the double-sided polished silicon wafer, through the cleaning and texturing necessary to create random pyramids on the surface, following the plasma enhanced chemical vapor deposition to create the amorphous silicon layers that envelop the monocrystalline

core. The last layer of ITO then gave us the completed bottom cell. With a novel processing technique, we then deposited a micrometer thick perovskite (Cs-MAFAPb(IBr)), which acted as our top cell. Finally, we terminated the solar cell with the transparent conductive oxide and the semitransparent electrodes on the front and back of our solar cell.

In chapter 3, we presented the results of our bifacial study. We started by giving an overview of our monofacial tandem solar cells that have an externally certified 25.2% power conversion efficiency. From there we moved on to bifacial tandems, where we reported the performances of perovskite tandems with 5 different bandgaps. Measured in monofacial mode, i.e. light shone only on the top, the solar cells with the higher bandgaps reported the highest efficiencies. More importantly, the highest J_{sc} was achieved in the condition of current matching at $1.68eV$. By then shining light also on the backside, we displayed the new set of data where we saw a different scenario. With increasing albedo on the rear of our solar cells, the bifacial tandems with lower bandgaps, $1.59 - 1.62eV$, reached the highest efficiencies around 28%. The explanation behind this increased power output can be found in the graph that plots current density to albedo. Here we saw that the more heavily mismatched tandems are the ones that gained the most from the extra photons that shined on the silicon, reaching J_{sc} over $21mA$. Whereas already current matched solar cells, gained less or nothing from collecting more radiation from the surroundings.

As an additional validation of our bifacial tandems, we provided outdoor data from different locations with different environments: Jeddah, Toronto, Karlsruhe. Demonstrating how bifacial tandems can outperform the monofacial counterparts in locations with sunny climates. We also studied the effect of different albedo on the bifacials, by recreating three diverse surroundings: concrete, artificial snow and synthetic grass. Surprisingly, we found out that concrete reflects the most light, thus resulting in a higher generated J_{sc} out of the three tested setups. However, in each condition, the bifacial tandem performed significantly better than the monofacial. The outdoor data validates even further our statement: perovskite/silicon bifacial tandem solar cells can indeed be more efficient than normal monofacial tandems.

4.1 Outlook

The enormous amount of effort that is being put in tandem solar cell research, finds its ultimate goal in future commercial applications. The recent evolution of solution processed highly efficient perovskite-based photovoltaic (PV) devices facilitates this end. Increasing the power conversion efficiency of solar panels not only generates more electricity but also contributes to the reduction of levelized cost of electricity (LCOE)⁴⁶. However, to breach the PV market, high efficiency is not enough. Long lasting stable devices are a requirement and much attention is now shifting towards that end, as reports show^{15,21,79}. It is in this scope that we decided to include outdoor field data of our bifacial tandems in this work.

A step further now makes us reflect upon the efficiency of our solar cells to a broader extent. And for this reason we include energy yield simulations to assess the performance of the bifacial tandems in realistic outdoor conditions (fig. 4.1). We chose two locations with very different climatic condition: Phoenix, Arizona, and Seattle, Washington. The annual EY was calculated for the same different perovskite bandgaps utilized in this work and compared for various albedo conditions. In the monofacial configuration, the highest EY is achieved with a perovskite bandgap of $1.68eV$ for both locations. Despite not being the optimal bandgap for monofacial tandem devices, which is between $1.70eV$ and $1.80eV$ ⁷⁰, this bandgap presents the best current matching throughout the whole year with the $1000nm$ thick perovskite layer and thus achieves the highest energy yield. The lowest performances in the monofacial configuration are achieved in the lowest bandgap ($1.59eV$) case, which suffers from high current mismatch losses, since the top cells harvests much more current than the bottom cell.

The scenario changes radically with a bifacial configuration. Even with a low reflective ground such as grey sandstone (average albedo equal to 9%), the optimum bandgap shifts to lower values: in Seattle it is $1.65eV$, while in Phoenix $1.62eV$. The lower optimum bandgap of the latter city, which presents a sunny desert climate, is attributed to the highest share of direct sunlight of the location, which then enhances the rear side irradiation due to albedo. Moving to higher reflective surroundings, the optimum bandgap shifts towards the lower value ($1.59eV$). EY improvements around 50% in Seattle and 60% in Phoenix with the respect to the

Si monofacial cell, are found with a bandgap of 1.59eV and the most reflective surface. Even if snow is not present in realistic situations, high reflection material can be used to enhance the albedo in locations with a high share of direct radiation, to fully exploit the potential of bifacial tandems with low perovskite bandgaps.

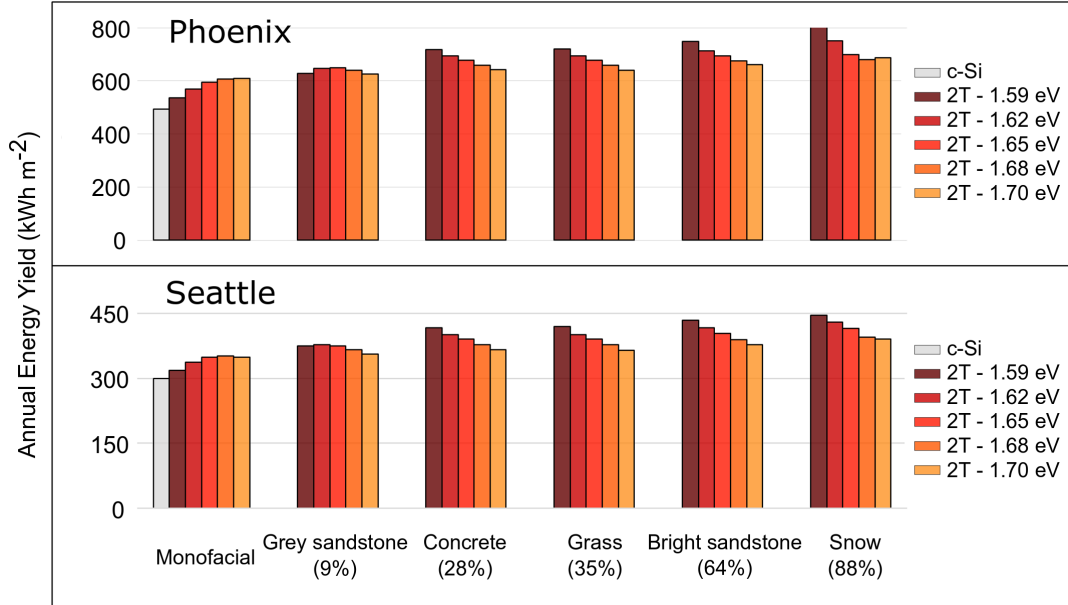


Figure 4.1: Annual energy yield simulations performed for two different locations with opposite climates. The graph shows a comparison between monofacial and bifacial tandems. In the first case the best bandgap is a wide one, in agreement with our predictions. In the second case, again in agreement with our predictions, the optimum bandgap moves towards lower bandgap values depending on the albedo intensity.

During the course of this thesis, we have striven to convincingly demonstrate a way to overcome the boundaries of the detailed balanced limit. Collecting extra photons, reflected or scattered from the surroundings, from the backside of solar cells, is a winning strategy and a promising route to push device efficiency even further, towards a renewable energy revolution.

References

- [1] Intergovernmental Panel of Climate Change. *Special Report: Global Warming of 1.5°C*. 2018.
- [2] Intergovernmental Panel of Climate Change. *Fifth Assessment Report*. 2014.
- [3] Global Market Outlook for Photovoltaics. 2019.
- [4] Solar Photovoltaic (PV) Market. *Update 2019 - Global Market Size, Market Share, Average Price, Regulations, and Key Country Analysis to 2030*. 2019.
- [5] Arno H. M. Smets et al. “Solar Energy: The Physics and Engineering of Photovoltaic Conversion, Technologies and Systems”. In: 2016.
- [6] P. Würfel and U. Würfel. *Physics of Solar Cells: From Basic Principles to Advanced Concepts*. Wiley, 2016. ISBN: 9783527413126.
- [7] “IEC 60904-3, Photovoltaic devices - Part 3: Measurement principles for terrestrial photovoltaic (PV) solar devices with reference spectral irradiance data”. In: 2008.
- [8] S.M. Sze. *SEMICONDUCTOR DEVICES: PHYSICS AND TECHNOLOGY, 2ND ED*. Wiley India Pvt. Limited, 2008. ISBN: 9788126516810.
- [9] William Shockley and Hans J. Queisser. “Detailed Balance Limit of Efficiency of p-n Junction Solar Cells”. In: *Journal of Applied Physics* 32.3 (1961), pp. 510–519. DOI: 10.1063/1.1736034.
- [10] Rappaport P. In: *RCA Rev.* 20 (1959), p. 373.
- [11] Wolf M. In: *Proc. I.R.E.* 48 (1960), p. 1246.
- [12] NREL. URL: http://www.nrel.gov/ncpc/images/efficiency_chart/jpg.

- [13] Uwe Rau, Ulrich W. Paetzold, and Thomas Kirchartz. “Thermodynamics of light management in photovoltaic devices”. In: *Phys. Rev. B* 90 (3 2014), p. 035211. DOI: 10.1103/PhysRevB.90.035211.
- [14] P. Baruch. “A two-level system as a model for a photovoltaic solar cell”. In: *Journal of Applied Physics* 57.4 (1985), pp. 1347–1355. DOI: 10.1063/1.334486.
- [15] Heping Shen et al. “Monolithic Perovskite/Si Tandem Solar Cells: Pathways to Over 30% Efficiency”. In: *Advanced Energy Materials* (), p. 1902840. DOI: 10.1002/aenm.201902840.
- [16] Robert T Ross and Arthur J Nozik. “Efficiency of hot-carrier solar energy converters”. In: *Journal of Applied Physics* 53.5 (1982), pp. 3813–3818.
- [17] Jianjun Tian and Guozhong Cao. “Semiconductor quantum dot-sensitized solar cells”. In: *Nano reviews* 4.1 (2013), p. 22578.
- [18] Akshay Rao and Richard H. Friend. “Harnessing singlet exciton fission to break the Shockley–Queisser limit”. In: *Nature Reviews Materials* 2.11 (2017), pp. 2058–8437. DOI: 10.1038/natrevmats.2017.63.
- [19] Katsuaki Tanabe. “A review of ultrahigh efficiency III-V semiconductor compound solar cells: multijunction tandem, lower dimensional, photonic up/down conversion and plasmonic nanometallic structures”. In: *Energies* 2.3 (2009), pp. 504–530.
- [20] Thomas G. Allen et al. “Passivating contacts for crystalline silicon solar cells”. In: *Nature Energy* 4.11 (2019), pp. 2058–7546. DOI: 10.1038/s41560-019-0463-6.
- [21] Ajay Kumar Jena, Ashish Kulkarni, and Tsutomu Miyasaka. “Halide perovskite photovoltaics: background, status, and future prospects”. In: *Chemical reviews* 119.5 (2019), pp. 3036–3103.
- [22] Anton R Chakhmouradian and Patrick M Woodward. *Celebrating 175 years of perovskite research: a tribute to Roger H. Mitchell*. 2014.
- [23] H. L. Wells. *Über die Cäsium- und Kalium-Bleihalogenide*. Jan. 1893. DOI: 10.1002/zaac.18930030124.

- [24] Dieter Weber. “CH₃NH₃PbX₃, ein Pb (II)-system mit kubischer perowskitstruktur/CH₃NH₃PbX₃, a Pb (II)-system with cubic perovskite structure”. In: *Zeitschrift für Naturforschung B* 33.12 (1978), pp. 1443–1445.
- [25] Dieter Weber. “CH₃NH₃SnBr_xI_{3-x} (x= 0-3), ein Sn (II)-System mit kubischer Perowskitstruktur/CH₃NH₃SnBr_xI_{3-x} (x= 0-3), a Sn (II)-system with cubic perovskite structure”. In: *Zeitschrift für Naturforschung B* 33.8 (1978), pp. 862–865.
- [26] CHR KN MØLLER. “A phase transition in caesium plumbochloride”. In: *Nature* 180.4593 (1957), pp. 981–982.
- [27] CHR KN MØLLER. “Crystal structure and photoconductivity of caesium plumbohalides”. In: *Nature* 182.4647 (1958), pp. 1436–1436.
- [28] Akihiro Kojima et al. “Organometal halide perovskites as visible-light sensitizers for photovoltaic cells”. In: *Journal of the American Chemical Society* 131.17 (2009), pp. 6050–6051.
- [29] Michael M Lee et al. “Efficient hybrid solar cells based on meso-superstructured organometal halide perovskites”. In: *Science* 338.6107 (2012), pp. 643–647.
- [30] James M Ball et al. “Low-temperature processed meso-superstructured to thin-film perovskite solar cells”. In: *Energy & Environmental Science* 6.6 (2013), pp. 1739–1743.
- [31] Mingzhen Liu, Michael B Johnston, and Henry J Snaith. “Efficient planar heterojunction perovskite solar cells by vapour deposition”. In: *Nature* 501.7467 (2013), pp. 395–398.
- [32] Jarvist M Frost et al. “Atomistic origins of high-performance in hybrid halide perovskite solar cells”. In: *Nano letters* 14.5 (2014), pp. 2584–2590.
- [33] Jun Hong Noh et al. “Chemical management for colorful, efficient, and stable inorganic–organic hybrid nanostructured solar cells”. In: *Nano letters* 13.4 (2013), pp. 1764–1769.
- [34] Giles E Eperon et al. “Formamidinium lead trihalide: a broadly tunable perovskite for efficient planar heterojunction solar cells”. In: *Energy & Environmental Science* 7.3 (2014), pp. 982–988.

- [35] Sneha A. Kulkarni et al. “Band-gap tuning of lead halide perovskites using a sequential deposition process”. In: *J. Mater. Chem. A* 2 (24 2014), pp. 9221–9225. DOI: 10.1039/C4TA00435C.
- [36] Kenjiro Miyano et al. “Lead halide perovskite photovoltaic as a model p–i–n diode”. In: *Accounts of chemical research* 49.2 (2016), pp. 303–310.
- [37] Takashi Kondo et al. “Resonant third-order optical nonlinearity in the layered perovskite-type material (C₆H₁₃NH₃)₂PbI₄”. In: *Solid state communications* 105.8 (1998), pp. 503–506.
- [38] Kenichiro Tanaka et al. “Comparative study on the excitons in lead-halide-based perovskite-type crystals CH₃NH₃PbBr₃ CH₃NH₃PbI₃”. In: *Solid state communications* 127.9-10 (2003), pp. 619–623.
- [39] Federico Brivio et al. “Relativistic quasiparticle self-consistent electronic structure of hybrid halide perovskite photovoltaic absorbers”. In: *Physical Review B* 89.15 (2014), p. 155204.
- [40] Martin A Green, Anita Ho-Baillie, and Henry J Snaith. “The emergence of perovskite solar cells”. In: *Nature photonics* 8.7 (2014), p. 506.
- [41] Stefaan De Wolf et al. “Organometallic halide perovskites: sharp optical absorption edge and its relation to photovoltaic performance”. In: *The journal of physical chemistry letters* 5.6 (2014), pp. 1035–1039.
- [42] Wan-Jian Yin, Tingting Shi, and Yanfa Yan. “Superior Photovoltaic Properties of Lead Halide Perovskites: Insights from First-Principles Theory”. In: *The Journal of Physical Chemistry C* 119.10 (2015), pp. 5253–5264. DOI: 10.1021/jp512077m.
- [43] Samuel D. Stranks et al. “Electron-Hole Diffusion Lengths Exceeding 1 Micrometer in an Organometal Trihalide Perovskite Absorber”. In: *Science* 342.6156 (2013), pp. 341–344. DOI: 10.1126/science.1243982.
- [44] Qingfeng Dong et al. “Electron-hole diffusion lengths \geq 175 μ m in solution-grown CH₃NH₃PbI₃ single crystals”. In: *Science* 347.6225 (2015), pp. 967–970. DOI: 10.1126/science.aaa5760.

- [45] Tsutomu Miyasaka. “Lead Halide Perovskites in Thin Film Photovoltaics: Background and Perspectives”. In: *Bulletin of the Chemical Society of Japan* 91.7 (2018), pp. 1058–1068. DOI: 10.1246/bcsj.20180071.
- [46] Bo Chen et al. “Progress in Tandem Solar Cells Based on Hybrid Organic–Inorganic Perovskites”. In: *Advanced Energy Materials* 7.14 (2017), p. 1602400. DOI: 10.1002/aenm.201602400.
- [47] Charles H Henry. “Limiting efficiencies of ideal single and multiple energy gap terrestrial solar cells”. In: *Journal of applied physics* 51.8 (1980), pp. 4494–4500.
- [48] The Duong et al. “Semitransparent perovskite solar cell with sputtered front and rear electrodes for a four-terminal tandem”. In: *IEEE Journal of Photovoltaics* 6.3 (2016), pp. 679–687.
- [49] Steve Albrecht et al. “Monolithic perovskite/silicon-heterojunction tandem solar cells processed at low temperature”. In: *Energy & Environmental Science* 9.1 (2016), pp. 81–88.
- [50] Yi Hou et al. “Efficient Charge Collection in Tandem Solar Cells based on Solution-Processed, Micrometer-Thick, Perovskite and Textured Crystalline Silicon”. In: *Science* (2020). DOI: 10.1126/science.aaz3691.
- [51] Philipp Löper et al. “Organic–inorganic halide perovskite/crystalline silicon four-terminal tandem solar cells”. In: *Physical Chemistry Chemical Physics* 17.3 (2015), pp. 1619–1629.
- [52] Steve Albrecht et al. “Towards optical optimization of planar monolithic perovskite/silicon-heterojunction tandem solar cells”. In: *Journal of Optics* 18.6 (2016), p. 064012.
- [53] Jérémie Werner, Bjoern Niesen, and Christophe Ballif. “Perovskite/Silicon Tandem Solar Cells: Marriage of Convenience or True Love Story? – An Overview”. In: *Advanced Materials Interfaces* 5.1 (2018), p. 1700731. DOI: 10.1002/admi.201700731.

- [54] Heping Shen et al. “Metal halide perovskite: a game-changer for photovoltaics and solar devices via a tandem design”. In: *Science and Technology of Advanced Materials* 19.1 (2018), pp. 53–75. DOI: 10.1080/14686996.2017.1422365.
- [55] S. P. Bremner, M. Y. Levy, and C. B. Honsberg. “Analysis of tandem solar cell efficiencies under AM1.5G spectrum using a rapid flux calculation method”. In: *Progress in Photovoltaics: Research and Applications* 16.3 (2008), pp. 225–233. DOI: 10.1002/pip.799.
- [56] Florent Sahli et al. “Fully textured monolithic perovskite/silicon tandem solar cells with 25.2% power conversion efficiency”. In: *Nature materials* 17.9 (2018), pp. 820–826.
- [57] EL Unger et al. “Roadmap and roadblocks for the band gap tunability of metal halide perovskites”. In: *Journal of Materials Chemistry A* 5.23 (2017), pp. 11401–11409.
- [58] Yang Zhou et al. “Benzylamine-treated wide-bandgap perovskite with high thermal-photostability and photovoltaic performance”. In: *Advanced Energy Materials* 7.22 (2017), p. 1701048.
- [59] Fengjiu Yang et al. “Planar Perovskite Solar Cells with High Efficiency and Fill Factor Obtained Using Two-Step Growth Process”. In: *ACS applied materials & interfaces* 11.17 (2019), pp. 15680–15687.
- [60] Jason J Yoo et al. “An interface stabilized perovskite solar cell with high stabilized efficiency and low voltage loss”. In: *Energy & Environmental Science* 12.7 (2019), pp. 2192–2199.
- [61] Eui Hyuk Jung et al. “Efficient, stable and scalable perovskite solar cells using poly (3-hexylthiophene)”. In: *Nature* 567.7749 (2019), pp. 511–515.
- [62] Zhaolai Chen et al. “Single-crystal MAPbI₃ perovskite solar cells exceeding 21% power conversion efficiency”. In: *ACS Energy Letters* 4.6 (2019), pp. 1258–1259.
- [63] Yuze Lin et al. “Matching Charge Extraction Contact for Wide-Bandgap Perovskite Solar Cells”. In: *Advanced materials* 29.26 (2017), p. 1700607.

- [64] G Sala et al. “Albedo collecting photovoltaic bifacial panels”. In: *pvse* (1984), pp. 565–569.
- [65] Reza Asadpour et al. “Bifacial Si heterojunction-perovskite organic-inorganic tandem to produce highly efficient ($\eta T^* \approx 33\%$) solar cell”. In: *Applied Physics Letters* 106.24 (2015), p. 243902. DOI: 10.1063/1.4922375.
- [66] Andreas Hübner, Armin G. Aberle, and Rudolf Hezel. “Novel cost-effective bifacial silicon solar cells with 19.4% front and 18.1% rear efficiency”. In: *Applied Physics Letters* 70.8 (1997), pp. 1008–1010. DOI: 10.1063/1.118466.
- [67] Fan Fu et al. “Low-temperature-processed efficient semi-transparent planar perovskite solar cells for bifacial and tandem applications”. In: *Nature communications* 6.1 (2015), pp. 1–9.
- [68] Yaoming Xiao et al. “Efficient bifacial perovskite solar cell based on a highly transparent poly (3, 4-ethylenedioxythiophene) as the p-type hole-transporting material”. In: *Journal of Power Sources* 306 (2016), pp. 171–177.
- [69] M. Ryyan Khan and Muhammad A. Alam. “Thermodynamic limit of bifacial double-junction tandem solar cells”. In: *Applied Physics Letters* 107.22 (2015), p. 223502. DOI: 10.1063/1.4936341.
- [70] Jonathan Lehr et al. “Energy yield of bifacial textured perovskite/silicon tandem photovoltaic modules”. In: *Solar Energy Materials and Solar Cells* 208 (2020), p. 110367.
- [71] F. Isikgor et al. “manuscript in preparation”. In: ().
- [72] Michael C. Brennan et al. “Light-Induced Anion Phase Segregation in Mixed Halide Perovskites”. In: *ACS Energy Letters* 3.1 (2018), pp. 204–213. DOI: 10.1021/acseenergylett.7b01151.
- [73] Dane W DeQuilettes et al. “Photo-induced halide redistribution in organic–inorganic perovskite films”. In: *Nature communications* 7.1 (2016), pp. 1–9.
- [74] Yanqi Luo et al. “Direct observation of halide migration and its effect on the photoluminescence of methylammonium lead bromide perovskite single crystals”. In: *Advanced Materials* 29.43 (2017), p. 1703451.

- [75] Konrad Domanski et al. “Migration of cations induces reversible performance losses over day/night cycling in perovskite solar cells”. In: *Energy Environ. Sci.* 10 (2 2017), pp. 604–613. DOI: 10.1039/C6EE03352K.
- [76] Wanyi Nie et al. “Light-activated photocurrent degradation and self-healing in perovskite solar cells”. In: *Nature communications* 7.1 (2016), pp. 1–9.
- [77] Konrad Domanski et al. “Systematic investigation of the impact of operation conditions on the degradation behaviour of perovskite solar cells”. In: *Nature Energy* 3.1 (2018), pp. 61–67.
- [78] Michael Saliba et al. “Measuring aging stability of perovskite solar cells”. In: *Joule* 2.6 (2018), pp. 1019–1024.
- [79] Nam-Gyu Park et al. “Towards stable and commercially available perovskite solar cells”. In: *Nature Energy* 1.11 (2016), pp. 1–8.